LBNL-40405
UC-404

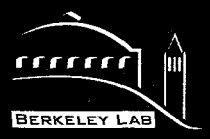

ERNEST ORLANDO LAWRENCE
BERKELEY NATIONAL LABORATORY

Cold SQUIDs and Hot Samples

Thomas S.-C. Lee

Materials Sciences Division

May 1997

Ph.D. Thesis

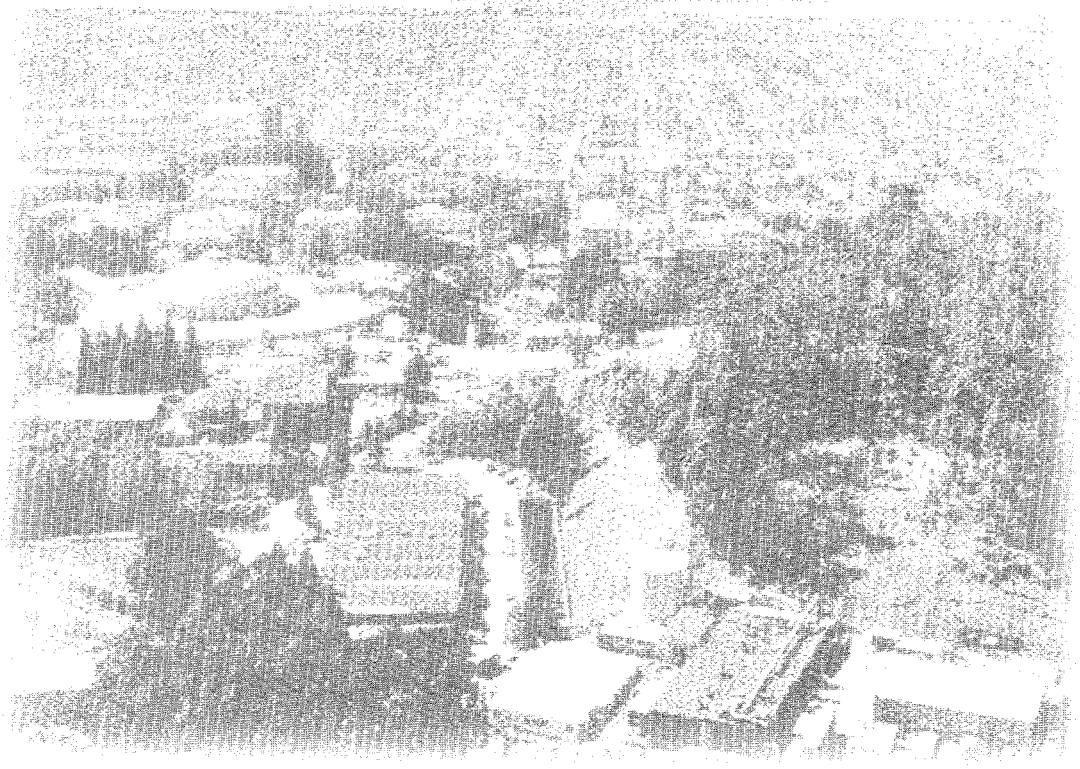

LBNL-40405

Cold SQUIDs and Hot Samples

by

Thomas Shih-Chun Lee
(Ph.D. Thesis)

Department of Physics, University of California
and
Materials Sciences Division
Lawrenece Berkeley National Laboratory
University of California
Berkeley, CA 94720

May 1997

This work was supported by the Office of Basic Energy Sciences, Materials Sciences Division of the U.S. Department of Energy under contract number DE-AC03-76SF00098.

Cold SQUIDs and Hot Samples

by

Thomas Shih-Chun Lee

B.A. (Stanford University) 1991
M.A. (University of California at Berkeley) 1993

A dissertation submitted in partial satisfaction of the
requirements for the degree of
Doctor of Philosophy

in

Physics

in the

GRADUATE DIVISION
of the
UNIVERSITY of CALIFORNIA at BERKELEY

Committee in charge:

Professor John Clarke, Chair
Professor Daniel Rokhsar
Professor Peter Schultz

Spring 1997

Cold SQUIDs and Hot Samples

by

Thomas Shih-Chun Lee

Abstract

Cold SQUIDs and Hot Samples

by

Thomas Shih-Chun Lee

Doctor of Philosophy in Physics

University of California at Berkeley

Professor John Clarke, Chair

Low transition temperature (low-T_c) and high-T_c Superconducting QUantum Interference Devices (SQUIDs) have been used to perform high-resolution magnetic measurements on samples whose temperatures are much higher than the operating temperatures of the devices. Part I of this work focuses on measurements of the rigidity of flux vortices in high-T_c superconductors using two low-T_c SQUIDs, one on either side of a thermally-insulated sample. The correlation between the signals of the SQUIDs is a direct measure of the extent of correlation between the movements of opposite ends of vortices. These measurements were conducted under the previously-unexplored experimental conditions of nominally-zero applied magnetic field, such that vortex-vortex interactions were unimportant, and with zero external current. At specific temperatures, we observed highly-correlated noise sources, suggesting that the vortices moved as rigid rods. At other temperatures, the noise was mostly uncorrelated, suggesting that the relevant vortices were pinned at more than one point along their length.

Part II describes the design, construction, performance, and applications of a scanning high-T_c SQUID microscope optimized for imaging room-temperature objects with very high spatial resolution and magnetic source sensitivity. We achieved a spatial resolution of 15 μm, which is at least 60 times better than that of low-T_c SQUID microscopes (for room-temperature samples) to date. As an example of a biological application of our microscope, we measured the magnetic flux noise generated by magnetotactic bacteria, which possess intrinsic magnetic dipole moments. When the bacteria are swimming, we observe characteristic peaks in the flux spectral density, which result from precessional movements

of the bodies of the bacteria due to their rotating flagella. When the bacteria are non-motile or dead, the flux spectral density is consistent with that produced by Brownian rotation. Because of the high sensitivity of the microscope, we are also able to resolve the dipole moment of a single, swimming bacterium. Finally, an experiment is proposed to track magnetotactic bacteria as they migrate through an opaque, porous matrix, which is a situation of relevance to bioremediation applications.

Professor John Clarke
Dissertation Committee Chair

Contents

Acknowledgments

I would like to give deep thanks to my advisor, Professor John Clarke, for his support and encouragement of my work over these past five-and-a-half years. I also gratefully acknowledge the National Science Foundation, the Department of Education, and the Department of Energy for providing me with financial support.

The people I have worked with and befriended during graduate school are what have made the experience worthwhile. Gene Dantsker, in addition to fabricating excellent high-T_c SQUIDs for the SQUID microscope, made working in the second basement of Birge Hall most enjoyable with his good humor and late-night comradery. Yann Chemla, Mike Adamkiewicz, and Wanda Rivera conquered the daunting task of growing magnetotactic bacteria. Yann also spent many hours helping me maintain and run the SQUID microscope, as well as collaborating with me on theoretical calculations of flux noise generated by magnetotactic bacteria. Professor Bob Buchanan provided us with indispensible facilities and good advice for growing bacteria. Professor Dennis Bazylinski kindly supplied us with initial bacteria cultures and with recipes for growing them. I am greatly indebted to the student members and staff of the Berkeley Microfabrication Lab who helped me learn the fine-art of microfabrication. In particular, I would like to thank Keith Schwab and Amy Wang for helping me fabricate silicon nitride windows, and Dave Hebert and Xiao-Fan Meng for invaluable assistance with low-T_c SQUID fabrication. I would also like to acknowledge the excellent work and advice provided to me by the Physics Department Machine Shop in the design and construction of the SQUID microscope.

Professor David Drubin provided me with the opportunity to work in his biology lab for a semester, giving me valuable research experience not normally available to physicists. I would like to thank everybody in his lab for patiently answering all of my many questions and for making me feel like a part of the group. In addition, Professor Dan Rokhsar was a great source of encouragement and knowledge for me as I was becoming acquainted with modern biology.

Lise Sagdahl not only worked very diligently with me on the vortex-correlation experiments, but also helped ease my transition into graduate research while I was a first-year graduate student. Nancy Missert initiated the vortex-correlation experiments, and I would like to thank her for her valuable advice and for her patience in transferring her knowledge to me. Professor Fred Wellstood provided timely advice on junction-oxidation procedures

for low-T_c SQUID fabrication. Professor John Clem performed crucial calculations of the magnetic fields and interaction energies of pancake vortices. I would also like to thank our collaborators who provided us with samples for the vortex-correlation experiments: Kookrin Char, Jim Eckstein, Dave Fork, Lou Lombardo, Aharon Kapitulnik, Lynn Schneemeyer, J. Waszczak, and Bruce van Dover.

Working in the Clarke Group has been a great experience for me mostly because of the intelligence, honesty, and generosity of my fellow group members. I want to take this opportunity to thank each of them for making graduate school both stimulating and fun.

Finally, I would like to thank my mother and father for their many sacrifices, endless support, and unconditional love which have made all of this possible. I thank Melini for her limitless love, understanding, and encouragement.

Chapter 1

Introduction

Superconducting QUantum Interference Devices (SQUIDs) are the most sensitive detectors of magnetic flux. However, one of the primary requirements of SQUIDs is the need to maintain them at cryogenic temperatures. For a sample whose temperature is much greater than the SQUID operating temperature, this implies that the SQUID must be thermally-isolated from the sample. However, at the same time, the SQUID-sample distance must often be made as small as possible, in order to increase the amount of magnetic flux coupled into the SQUID.

In the two parts of this thesis, I describe two intimately-related approaches to this problem in connection with two different projects. In Part I, I explain how two low transition temperature (low-T_c) SQUIDs can be placed within 100-200 μm of both sides of a high-T_c superconducting sample in a liquid-helium-cooled vacuum can. The sample temperature can be varied up to about 120 K while maintaining the SQUIDs below 7 K. This technique is the two-SQUID extension of the idea implemented by Mark Ferrari and others in single-SQUID measurements of high-T_c films and crystals in our group [3]. The aim of the project described in Part I is to explore the intrinsic flexibility of flux vortices in high-T_c superconductors.

In Part II, I describe a "SQUID microscope"in which a high-T_c SQUID can be positioned within 15 μm of a room-temperature sample maintained at atmospheric pressure. The sample can be scanned over the SQUID, thereby producing a two-dimensional magnetic field map. Our experiences with the experimental apparatus described in Part I led us to contemplate how well a high-T_c SQUID could be thermally-isolated from a room-temperature sample, while maintaining a small SQUID-sample separation. We realized that,

with proper design, there was no *fundamental* limitation to how small the separation could be made. I discuss the design, construction and performance of the SQUID microscope in Part II. I also describe magnetic measurements of live magnetotactic bacteria.

Part I

Correlation of Vortex Motion in High-Tc Superconductors

Chapter 2

Superconductivity and Vortices

2.1 Type I and Type II Superconductivity

Superconductivity is a phase whose electrical and magnetic properties differ drastically from those of normal metals. Below a transition temperature, T_c, electrons experience an attractive interaction with respect to each other, causing them to condense into Cooper pairs. The quantum-mechanical wave functions of the Cooper pairs lock together to produce a macroscopic wave function or "order parameter," $\psi(\overline{\mathbf{r}})$, representing quantum coherence over macroscopic length scales. Some of the well-known manifestations of superconductivity are dissipation-less DC current flow and the Meissner effect, in which magnetic flux is largely excluded from the interior of a superconductor by the spontaneous generation of a surface current [2].

The magnetic behavior of superconductors strongly depends on the relative sizes of two temperature-dependent length-scales of the superconducting phase: the Ginzburg-Landau coherence length, $\xi(T)$, and the magnetic penetration depth, $\lambda(T)$. $\xi(T)$ can be thought of as the minimum distance over which $\psi(\overline{\mathbf{r}})$ can exhibit large changes in amplitude. In the ideal case when the superconductor is free of defects and impurities, $\xi(T)$ is approximately equal to the size of a Cooper pair in the system. $\lambda(T)$ is the distance over which magnetic flux is allowed to penetrate the body of a superconductor in the Meissner state. The ratio between these two lengths is defined as the Ginzburg-Landau parameter $\kappa(T) = \lambda(T)/\xi(T)$.

The Ginzburg-Landau (GL) theory divides superconductors into two classes: type I and type II. Type I materials have $\kappa(T) < 1/\sqrt{2}$, whereas type II materials satisfy $\kappa(T) >$

$1/\sqrt{2}$. The fundamental difference between these is the sign of the surface energy associated with a boundary between superconducting and non-superconducting ("normal") regions. In a type I superconductor, the surface energy is positive, which inhibits the formation of superconducting-normal interfaces in the material. On the other hand, the surface energy is negative in type II superconductors. This implies that, under certain conditions, it becomes energetically-favorable for normal regions to spontaneously form within the superconductor, as this increases the interfacial area separating superconducting and normal regions.

From thermodynamic arguments, one can show that there exist two critical magnetic fields, $H_{c1}(T)$ and $H_{c2}(T)$, which determine when normal and superconducting phases coexist in what is known as the *mixed state*. The region in the H-T phase diagram occupied by the mixed state is shown in Figure 2.1. For a given T, the Meissner state, corresponding to complete exclusion of magnetic flux from the bulk of the material, exists below $H_{c1}(T)$. The mixed state occurs between $H_{c1}(T)$ and $H_{c2}(T)$, and the normal state exists above $H_{c2}(T)$.

2.2 Magnetic Flux Vortices

2.2.1 Vortex Structure

In the mixed state of type II superconductors, the characteristic way in which a normal region exists is within a magnetic flux vortex (Figure 2.2(a)) [2]. The normal core, in which $|\psi(\overline{\mathbf{r}})|$ is suppressed, extends to a radius approximately equal to $\xi(T)$ (Figure 2.2(b)). $|\psi(\overline{\mathbf{r}})|^2$ is proportional to the local density of Cooper pairs and is zero at the vortex center. The core is surrounded by a circulating current which exhibits a maximum at a distance on the order of $\lambda(T)$ from the center. The current generates exactly one flux quantum ($\Phi_o = 2.07 \times 10^{-15}\ \mathrm{T\,m^2}$) of magnetic flux, mostly confined to a region whose radius is comparable to $\lambda(T)$. The fundamental unit of flux, Φ_o, arises from the requirement of flux quantization imposed by the macroscopic quantum coherence in the system. In a sample of finite thickness, a straight-line vortex penetrates the entire thickness and terminates at the surfaces, where magnetic flux either escapes or enters, as shown in the right-hand schematic of Figure 2.2(a).

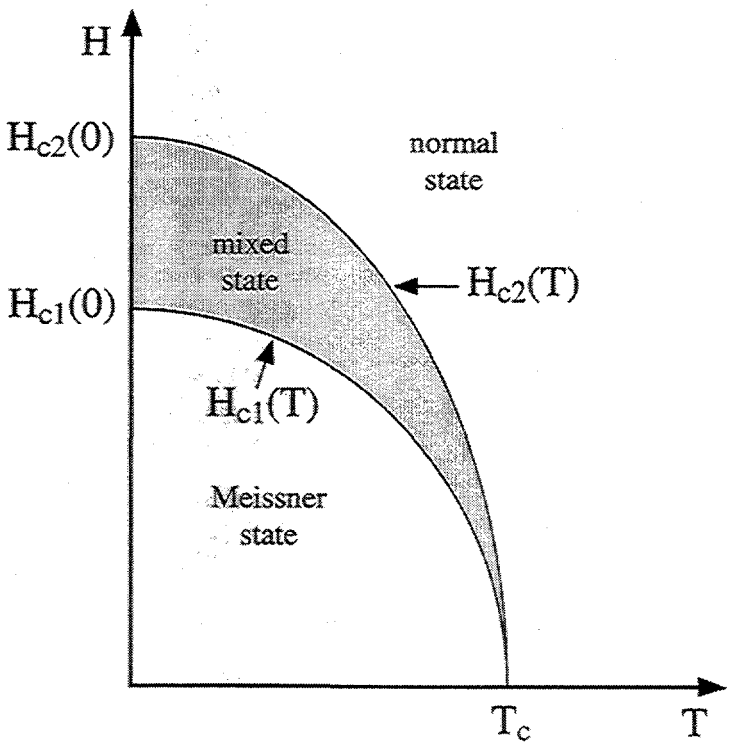

Figure 2.1: H-T phase diagram for a type II superconductor. $H_{c1}(T)$ and $H_{c2}(T)$ are temperature-dependent critical magnetic fields. T_c is the superconducting transition temperature.

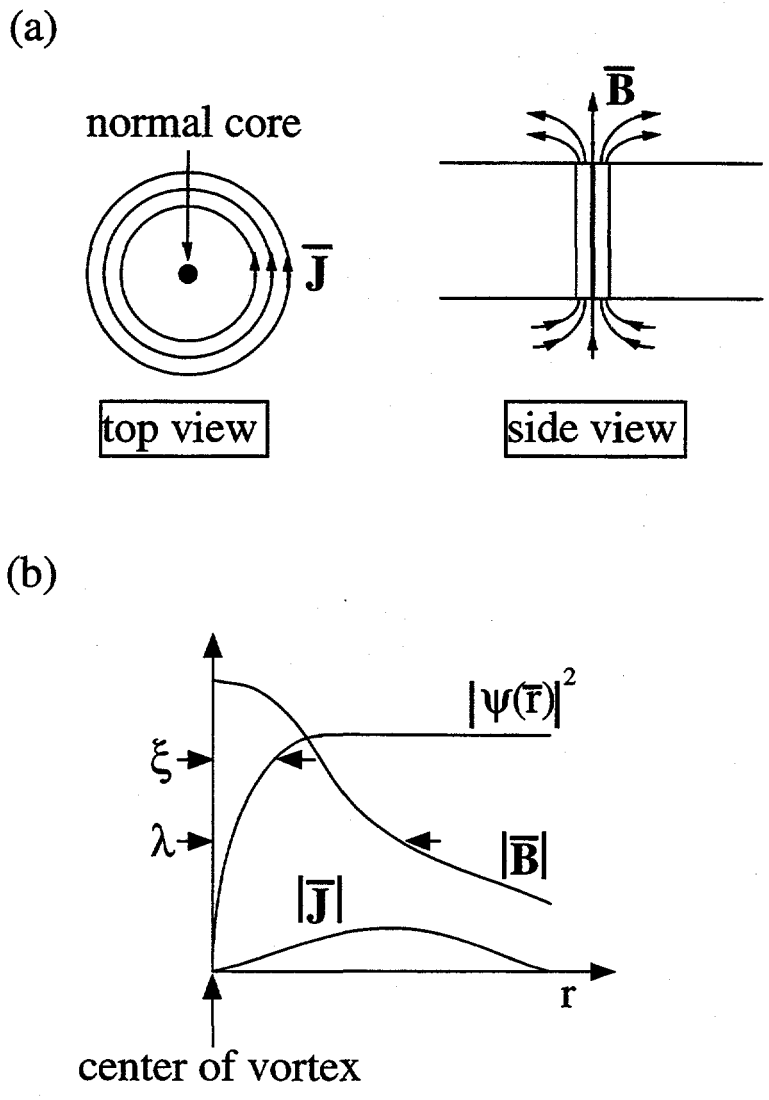

Figure 2.2: Magnetic flux vortex. (a) Schematic of a vortex. $\overline{\mathbf{J}}$ is the current density, and $\overline{\mathbf{B}}$ is the magnetic field. (b) Radial dependence of $|\psi(\overline{\mathbf{r}})|^2$, the magnetic field, and the current density.

2.2.2 Vortex Motion and the Role of Pinning

In an ideal superconductor free of defects, the translational motion of a vortex is similar to that of an object in a viscous fluid [2]. The viscous force per unit length is given by $\overline{\mathbf{f}}_v = -\eta\overline{\mathbf{v}}$, where η is an effective viscosity coefficient, and $\overline{\mathbf{v}}$ is the vortex velocity. Vortex motion can be induced by the application of an external current through the material, as shown in Figure 2.3. The Lorentz force per unit length exerted on a vortex is given by $\overline{\mathbf{f}}_{lorentz} = \Phi_o\overline{\mathbf{J}} \times \hat{\mathbf{z}}$, where $\overline{\mathbf{J}}$ is the current density and $\hat{\mathbf{z}}$ is the unit vector pointing along the axis of the vortex. Hence, the vortices move perpendicular to the current. In equilibrium, the Lorentz force exactly balances the viscous force such that the vortex moves at a constant velocity. The viscous drag dissipates energy into the surrounding material. In addition, the vortex motion perpendicular to the current induces a finite voltage drop along the current, according to Faraday's law: $V = -d\Phi/dt$.

Defects and impurities exist in real materials. Grain boundaries, impurity atoms, and lattice defects represent locations where the superconducting phase is locally suppressed. Experimentally, it is well-known that flux vortices may become pinned by these types of imperfections. When an external current is run through the superconductor, the pinning may be so strong that vortices remain pinned, and no energy is dissipated. For example, vortex pinning allows high-field superconducting magnets to operate in the mixed state without dissipation.

Each pinning site has a potential energy associated with it. Figure 2.4 shows a typical pinning potential $U(R)$, where R is the lateral displacement of a vortex from the center of the pinning potential. The width of the pinning site is typically on the order of $\xi(T)$. There are two primary mechanisms by which a vortex can escape a pinning site. First, a vortex can be pushed out by the Lorentz force due to a current. The current effectively lowers the potential barrier of the pinning potential so that a vortex more readily escapes. In type II superconducting wire, the maximum transport current ("critical current") is reached when the Lorentz force begins to overcome the pinning. Currents larger than the critical current depin vortices in large numbers, thereby causing heat dissipation in the wire.

The second mechanism of vortex depinning is thermal activation [3]. The characteristic time between depinning events is $\tau_{escape} = \tau_o exp[U(T)/k_BT]$, where τ_o is an attempt or vibration time, $U(T)$ is the pinning energy or well depth, and k_B is Boltzmann's constant. In fact, Lorentz forces enhance thermal activation because they effectively lower $U(T)$. As

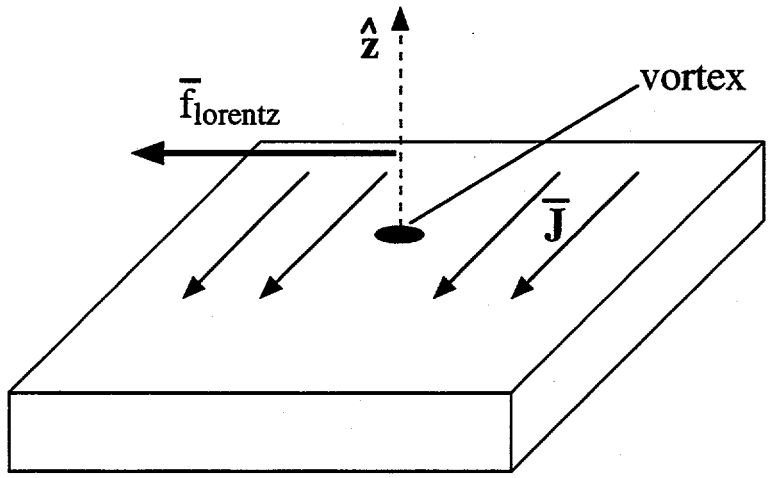

Figure 2.3: Schematic of Lorentz force exerted on a vortex by an electrical current.

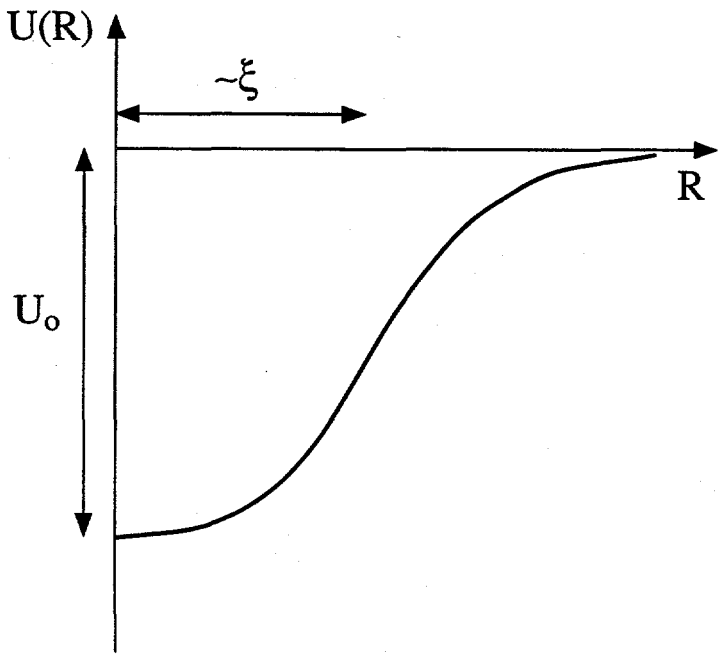

Figure 2.4: Typical vortex pinning potential.

we shall see later in Part I, the thermally-activated hopping of vortices among pinning sites is the primary mode of vortex motion measured in our experiments.

2.3 High-Tc Superconductors

Up until 1986, the highest T_c of all superconductors was that of Nb_3Ge ($T_c = 23$ K)[4]. All practical applications of superconductors, such as high-field magnets, required the use of liquid helium (T = 4.2 K) as a cryogen. But in 1986, high-Tc superconductors (HTSC) were discovered. This event sparked an enormous world-wide research effort into the physical and materials properties of these compounds. The high transition temperatures of materials such as $YBa_2Cu_30_{7-x}$ (YBCO) and $Bi_2Sr_2CaCu_2O_{8+y}$ (BSCCO) were found to exceed the boiling point of liquid nitrogen (77 K). The prospect of being able to use inexpensive liquid nitrogen rather than liquid helium as the cryogen inspired numerous groups to explore potential applications of HTSC. Some of the most widely publicized applications involved high-current applications, such as levitating trains and lossless power transmisssion.

However, much of the initial excitement surrounding these types of applications were soon dampened by the discovery that the critical currents of HTSC were particularly low. The problem was exacerbated when the materials were exposed to high magnetic fields, comparable to those encountered in real applications. Since high-T_c materials are type II, magnetic fields exceeding H_{c1} generate large numbers of flux vortices, which become pinned at defects in the material. Two factors conspire to depress the critical current. First, typical pinning energies are often too low to prevent vortex depinning at current densities of interest. Second, flux vortices were found to have low rigidity in HTSC, allowing them to bend and exhibit local fluctuations in lateral position at points along their lengths. This property makes vortices in HTSC particularly difficult to immobilize with pinning sites, since one must pin a vortex at multiple sites along its length in order to sufficiently suppress its motion.

Chapter 3

Vortices in High-Tc Superconductors

3.1 Influence of Anisotropy: Pancake-Stack Model

As mentioned in the previous chapter, the intrinsic rigidity of a flux vortex greatly determines how effectively it can be immobilized by a pinning site. A flux vortex in isotropic, conventional low-T_c superconductors typically behaves as a continuous, highly-rigid rod. Hence, it can usually be effectively pinned by a single, point-like pinning site. In contrast, the internal structure of flux vortices in HTSC is strongly influenced by the anisotropy of these layered materials. Figure 3.1 shows the unit cell crystal structure of YBCO. The anisotropy of the material is manifested by the fact that the zero-temperature GL coherence length, $\xi(0)$, is greater in the a-b plane than along the c-axis. This arises from the fact that the superconducting properties mainly result from the copper-oxygen (CuO_2) bilayers (one of which is indicated in Figure 3.1), lying parallel to the a and b axes. The zero-temperature anisotropy parameter is defined as $\gamma_{anis}(0) = \xi_{ab}(0)/\xi_c(0) = \lambda_c(0)/\lambda_{ab}(0)$, where $\xi_{ab}(0)$ and $\xi_c(0)$ are the in-plane and out-of-plane zero-temperature GL coherence lengths, respectively. The magnetic penetration depths are also anisotropic. For magnetic fields along the c-axis, the relevant zero-temperature penetration depth is $\lambda_{ab}(0)$, whereas $\lambda_c(0)$ applies to fields parallel to the a-b plane. Table 3.1 lists these parameters for YBCO and BSCCO (I will define the Josephson penetration depth, $\lambda_J(0)$, later). The large spread in some of the parameters for BSCCO is due to experimental uncertainty in the value of

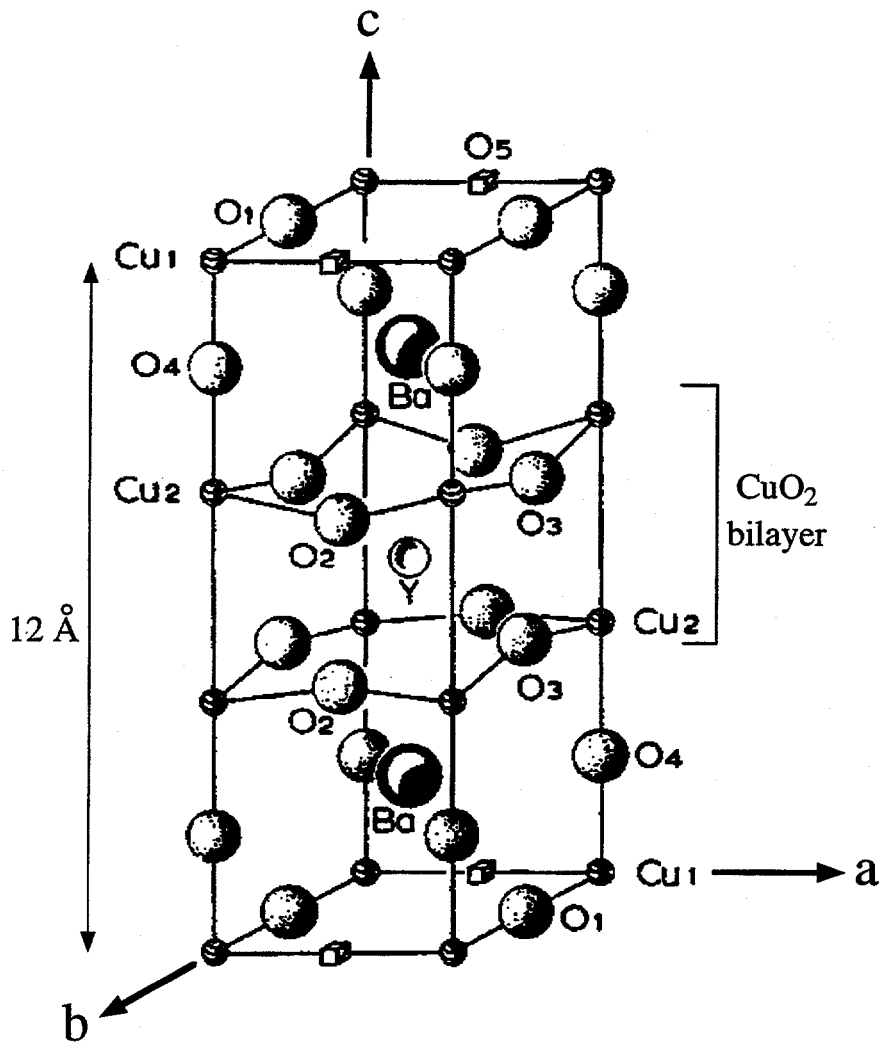

Figure 3.1: Unit-cell crystal structure of YBCO.

Material	$\xi_{ab}(0)$ (Å)	$\xi_c(0)$ (Å)	$\gamma_{anis}(0)$	$\lambda_J(0)$ (Å)	$\lambda_{ab}(0)$ (μm)	$\lambda_c(0)$ (μm)	s_c (Å)
YBCO	$12-16$	$1.5-3$	≈ 5	≈ 60	0.14	≈ 0.7	12
BSCCO	≈ 27	$0.03-0.5$	$55-900$	$800-14000$	0.20	$11-180$	15

Table 3.1: The zero-temperature GL coherence lengths [$\xi_{ab}(0)$ and $\xi_c(0)$], Josephson penetration depths [$\lambda_J(0)$], and magnetic penetration depths [$\lambda_{ab}(0)$ and $\lambda_c(0)$] for YBCO and BSCCO. The spacing between successive CuO_2 bilayers is s_c. The zero-temperature anisotropy parameter is $\gamma_{anis}(0) = \xi_{ab}(0)/\xi_c(0) = \lambda_c(0)/\lambda_{ab}(0)$.

$\xi_c(0)$. Nevertheless, it is certainly true that BSCCO is significantly more anisotropic than YBCO. For both materials, $\xi_c(0)$ is less than the vertical spacing between the centers of adjacent CuO_2 bilayers. Hence, these superconductors are best described as being composed of individual two-dimensional superconducting planes coupled along the c-direction, where each superconducting plane corresponds to a CuO_2 bilayer. This is very different from typical low-T_c materials such as niobium which are well-described by isotropic, continuum models.

Given the anistropic and layered nature of HTSC, a flux vortex along the c-axis may be considered as a stack of two-dimensional pancake vortices, each of which is confined to a CuO_2 bilayer (Figure 3.2) [5, 6, 7, 8]. This implies that vortices in the HTSC may be significantly less rigid than their low-T_c counterparts. The coupling between each pair of pancake vortices in the HTSC is determined by magnetic and Josephson coupling [5, 6, 7, 8, 9, 10, 11].

Magnetic coupling arises from the fact that pancakes situated in neighboring planes attract each other in the lateral direction. Figure 3.3 shows a qualitative physical explanation for this coupling force. The magnetic field produced by the lower pancake induces a screening current in the plane of the other pancake, due to the Meissner effect. The Lorentz force generated by this screening current causes the upper pancake to move laterally towards the lower pancake until the pancakes are aligned vertically.

Josephson coupling derives from the fact that the phases of the superconducting order parameters in neighboring CuO_2 bilayers are coupled in a manner that favors uniform phases along the c-axis, as described by the Josephson equations. The Josephson coupling energy between pancake vortices in adjacent planes is minimized when they are aligned vertically. A simple way to understand this is shown in Figure 3.4. Gauge invariance demands that the phase of the order parameter continuously change from 0 to 2π over one circular path around each pancake vortex, as shown in the figure. The potential energy associated with laterally separating the two pancakes is proportional to $\int dxdy[1-cos(\phi(x,y))]$, where $\phi(x,y)$ is the interplanar difference in the phases of the order parameters at position (x,y). The minimum potential energy occurs when $\phi(x,y)=0$ at all (x,y). It is clear from Figure 3.4 that this relation can be satisfied only if the pancake vortices are vertically aligned with each other. Otherwise, there will be non-zero phase differences between the two planes at various (x,y), thereby raising the potential energy. Hence, there is a lateral force due to Josephson coupling which tends to pull the pancakes into vertical alignment.

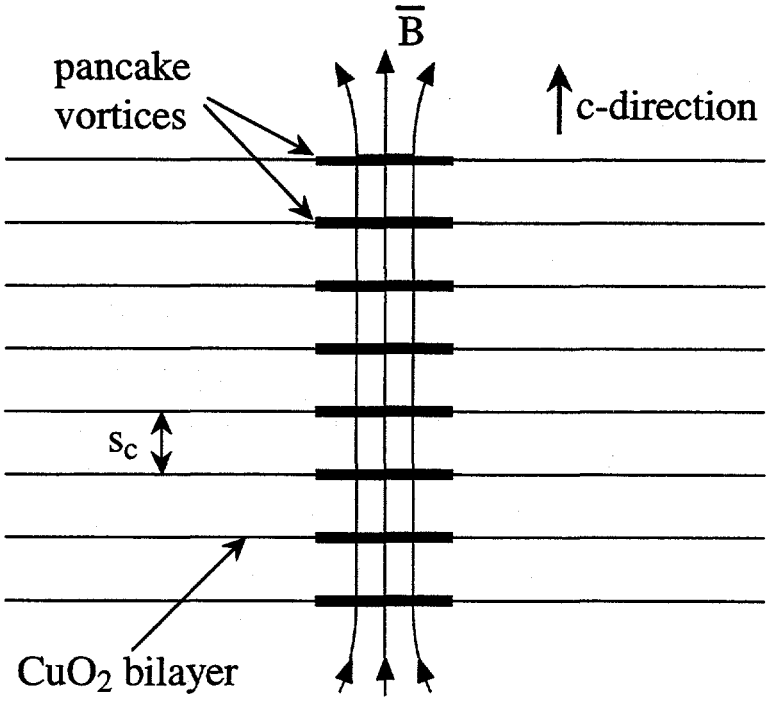

Figure 3.2: Schematic of a vortex modeled as a stack of pancake vortices.

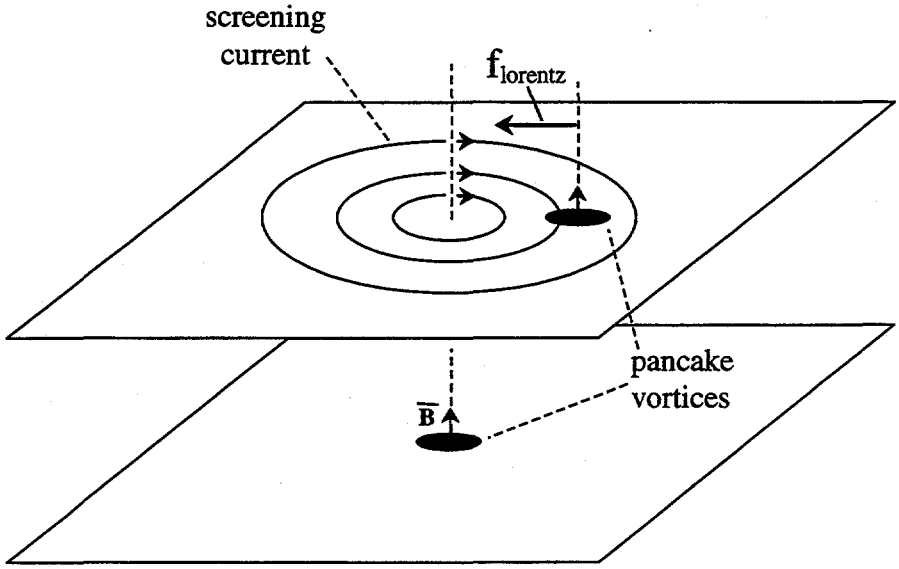

Figure 3.3: Physical explanation for the magnetic coupling force between pancake vortices.

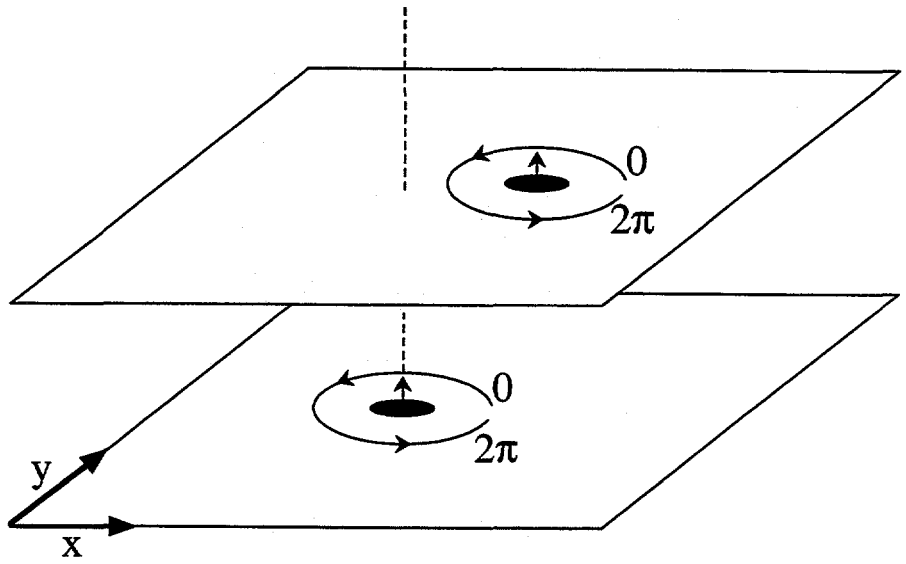

Figure 3.4: Physical explanation of Josephson coupling between pancake vortices. The phase θ of the order parameter varies from 0 to 2π around each pancake. The Josephson potential energy is minimized when the pancakes are vertically aligned.

3.2 Numerical Estimates of Coupling Strengths

It is possible to estimate the magnitudes of the potential energies of interaction due to magnetic and Josephson coupling between vortex pancakes. Let us consider an isolated vortex-pancake stack, representing a single flux vortex, with a single pancake displaced laterally by a distance r (Figure 3.5). I define $U_m(r)$ and $U_J(r)$ as the magnetic and Josephson potential energies, respectively. The sum $U_T(r) = U_m(r) + U_J(r)$ is equal to the amount of work that must be done in order to laterally displace the pancake from the rest of the pancake stack. $U_m(r)$ and $U_J(r)$ are equal to zero at $r = 0$. John Clem has performed order-of-magnitude estimates[1] of $U_m(r)$ and $U_J(r)$ (in cgs units):

$$U_m(r) \approx \frac{\Phi_o^2 s_c}{8\pi^2 \lambda_{ab}^2(0)} \left(\frac{r}{\lambda_{ab}(0)}\right)^2, \qquad r \ll \lambda_{ab}(0) \tag{3.1}$$

$$\approx \frac{\Phi_o^2 s_c}{8\pi^2 \lambda_{ab}^2(0)} \left(1 + ln\left(\frac{r}{2\lambda_{ab}(0)}\right)\right), \qquad r \gg \lambda_{ab}(0) \tag{3.2}$$

$$U_J(r) \approx \frac{\Phi_o^2 s_c}{8\pi^2 \lambda_{ab}^2(0)} \left(\frac{r}{\lambda_J(0)}\right)^2, \qquad r \ll \lambda_J(0) \tag{3.3}$$

$$\approx \frac{\Phi_o^2}{16\pi^2 \lambda_{ab}(0) \lambda_c(0)} r, \qquad r \gg \lambda_J(0) \tag{3.4}$$

where $\lambda_J(0) = \gamma_{anis}(0) s_c$ is the zero-temperature Josephson penetration depth. For intermediate values of r, we can interpolate these estimates to generate plots of $U_m(r)$ and $U_J(r)$ for YBCO and BSCCO at all r, as shown in Figure 3.6. The solid lines are calculated with the parameters listed in Table 3.1. For YBCO, I chose $\xi_{ab}(0) = 15$ Å and $\xi_c(0) = 3$ Å. For BSCCO, I used the parameters corresponding to $\gamma_{anis}(0) \approx 55$: $\xi_c(0) = 0.5$ Å, $\lambda_J(0) = 800$ Å, and $\lambda_c(0) = 11$ μm. At all values of r, the value of $U_T(r)$ for YBCO is at least 20 times greater than that for BSCCO. This reflects the fact that $\gamma_{anis}(0)$ is much greater for BSCCO than for YBCO. More detailed calculations of magnetic and Josephson coupling can be found elsewhere [5, 12].

3.3 Vortex-Shearing Experiments

The net interlayer coupling between pancakes has been investigated in the HTSC by experiments in the mixed state [13, 14, 15] in which a magnetic field ($\approx$1 T) was applied

[1] Private communication.

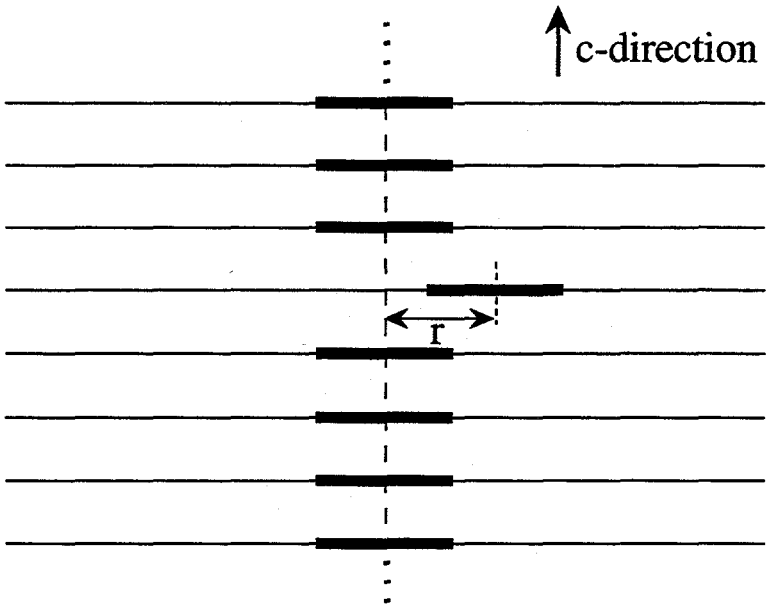

Figure 3.5: A stack of vortex pancakes with a single pancake laterally displaced from the central axis.

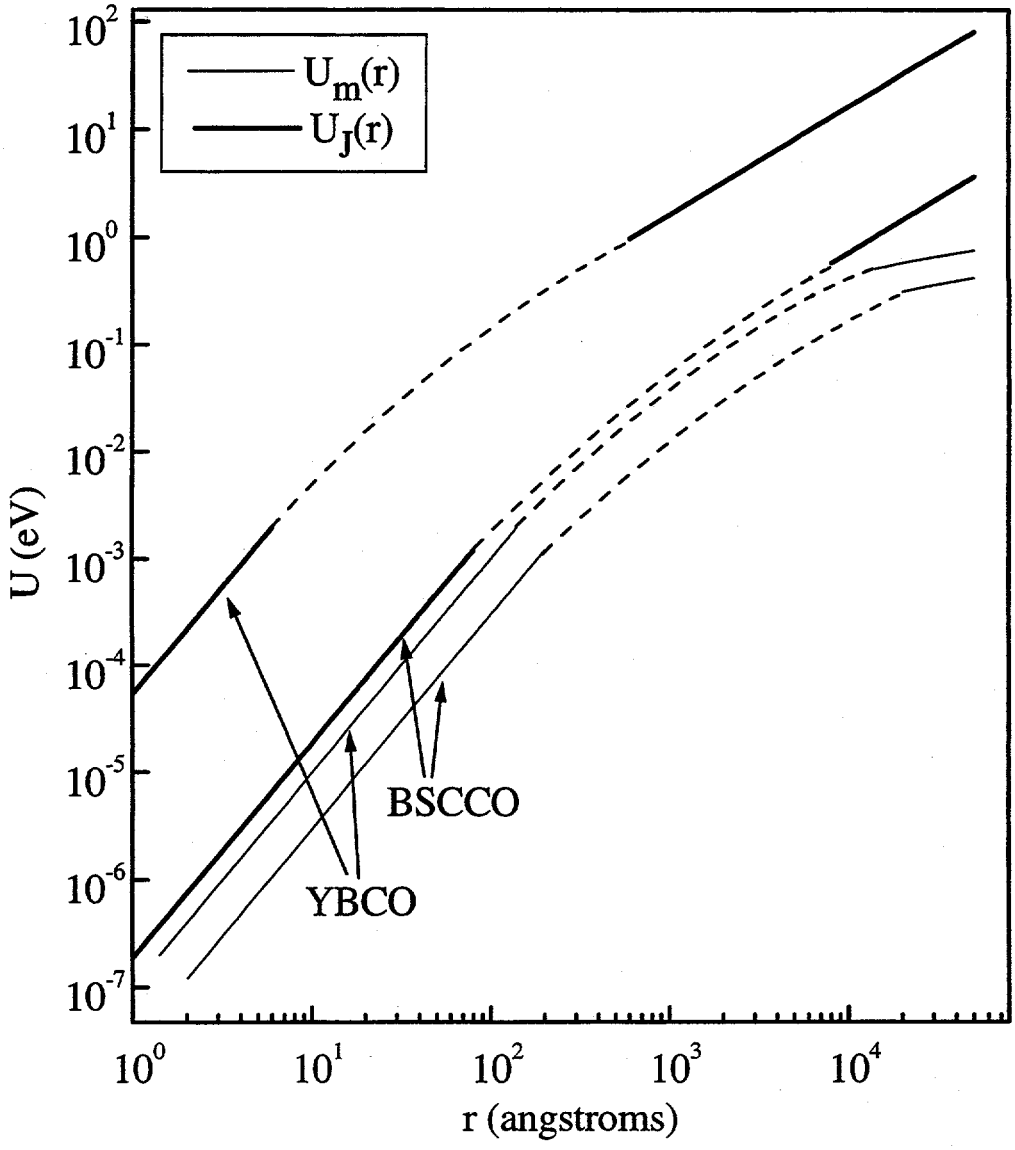

Figure 3.6: Estimated magnetic and Josephson potential energies for a laterally displaced pancake. Dashed lines indicate interpolations between high-r and low-r limits.

along the c-axis of a crystal and a current injected along one surface in the ab-direction (Figure 3.7(a)). The voltage drop due to vortex motion is measured at the top and bottom surfaces. Note that the current density is higher near the top surface with the current contacts than near the bottom surface, due to the manner in which the current distributes itself. Hence, the Lorentz force exerted on a vortex by the current is greater near the top surface than the bottom surface. In the case of BSCCO [13, 14], it was found that the voltage drop across the top surface greatly exceeded that across the bottom surface, implying that the pancake vortices near the top surface moved faster than those near the bottom surface (Figure 3.7(b)). Thus, vortices in BSCCO were sheared by the nonuniform current. In contrast, the voltages on the two sides of a YBCO crystal [15] were identical below a characteristic temperature, implying that the vortices moved as rigid rods. These findings are consistent with the numerical estimates in Section 3.2 which predict that the total coupling energy between pancakes in YBCO is at least 20 times greater than that in BSCCO.

These experiments were performed under two key experimental conditions. First, the areal density of vortices (proportional to the applied magnetic field) was sufficiently high to make vortex-vortex interactions important. This occurs when the average vortex-vortex spacing (d_{vv}) is comparable to or less than λ_{ab}. For BSCCO exposed to a field of 1 T along the c-axis, we have $d_{vv} \approx 0.045\,\mu\text{m} < 0.20\,\mu\text{m} = \lambda_{\text{ab}}$. Second, the applied current density was high enough to shear the vortices (in the case of BSCCO) and to overcome vortex pinning, corresponding to the limit of high Lorentz force.

3.4 Our Focus: Low-Field, Force-Free Limit

In contrast to the vortex-shearing experiments, our measurements focus on the opposite limits of nominally zero applied magnetic field ($< 10^{-7}$ T) and zero driving current. These experimental conditions allow us to investigate the dynamics of isolated vortices moving only under thermal activation and without the shearing forces exerted by a driving current. Hence, we observe vortex motion in a non-invasive fashion, allowing the pancake stack to be perturbed only by thermal fluctuations and the presence of pinning sites.

Although the residual dc magnetic field is much less than $H_{c1}(T)$ (except near T_c where H_{c1} goes to zero), vortices are generated in the film by the production of vortex-antivortex pairs as the sample is cooled through T_c. These vortices become pinned by

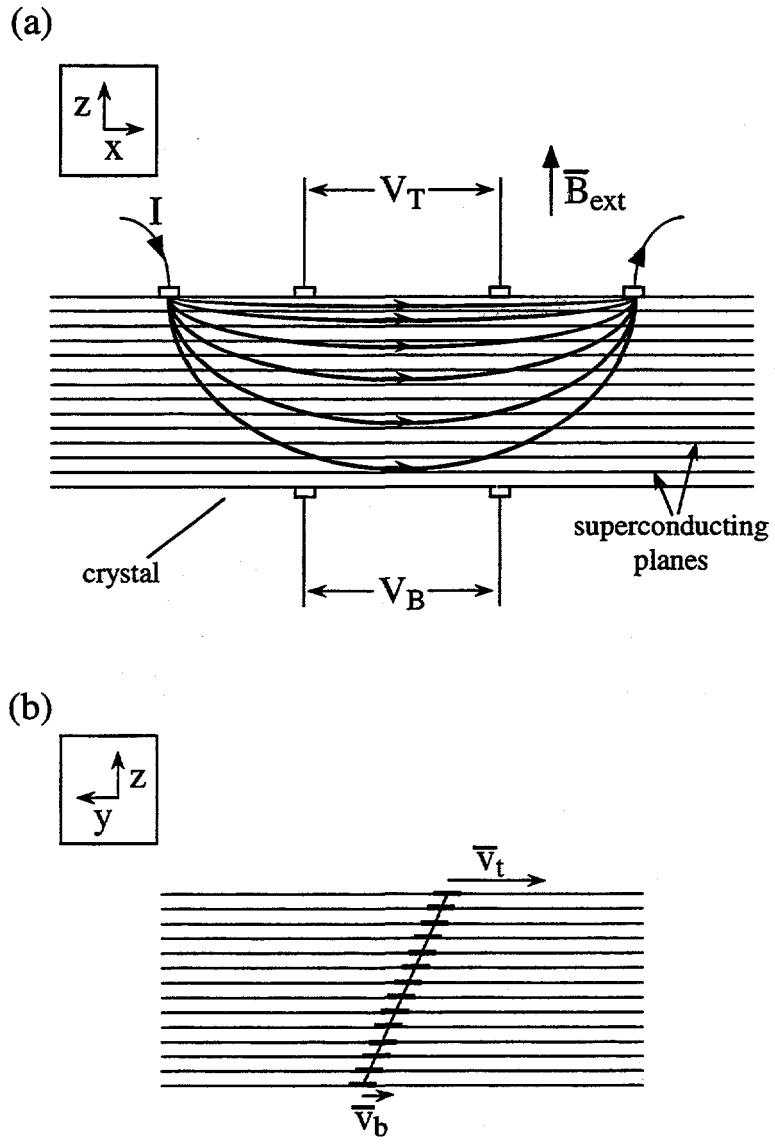

Figure 3.7: (a) Schematic of vortex-shearing experiment. I is the injected current, and V_T and V_B are the voltages measured across the top and bottom surfaces, respectively. Note that the current density is higher near the top surface. $\overline{B}_{ext}$ is the external magnetic field applied along the c-axis of the crystal. (b) View of a vortex along the direction of the current (x-direction). $\overline{v}_t$ and $\overline{v}_b$ are the velocities of pancakes near the top and bottom surfaces, respectively. The fact that $v_t \gg v_b$ causes vortex shearing. (Figures not drawn to scale.)

defects in the film and hop among different pinning sites by thermal activation.

There are several reasons why one may be interested in vortex dynamics under these experimental conditions. First, some significant applications of HTSC, such as Superconducting Quantum Interference Devices (SQUIDs), are carried out under these types of conditions. Since vortex motion often causes noise or other undesirable effects in such applications, it is important to understand the nature of vortices and vortex dynamics in these situations. Second, from the perspective of basic science, one would like to know how vortices behave in the limit of small lateral displacements, such as those caused by thermal activation. This corresponds to the situation of small r in Figure 3.6. Third, it is important to explore the properties of isolated vortices without the perturbing influences of vortex-vortex interactions. This potentially gives clearer insight into the fundamental forces governing the internal structure of vortices.

In order to sense the tiny flux changes produced by small vortex-displacements, we employ ultrasensitive dc SQUIDs in our measurements. We use two SQUIDs, one above and one below a film or crystal of YBCO or BSCCO, to measure the temporal correlation of the magnetic flux noise generated at the two surfaces by the motion of vortex pancakes. From the degree of correlation we infer the extent to which the motion of the pancakes on the opposite ends of a vortex are coherent, thereby providing a measure of the apparent rigidity of the entire pancake stack comprising the vortex.

Chapter 4

Experimental Apparatus

4.1 Basic Idea

The primary goal of the experimental apparatus is to bring two low-T_c SQUIDs as close as possible to both sides of a high-T_c sample, whose temperature we want to vary to values above its T_c. Hence, the sample must be properly thermally-isolated from the SQUIDs so that the devices are maintained in their operating temperature range. The general idea is illustrated in Figure 4.1. The flux emanating from both ends of a given vortex are coupled into the SQUIDs, and the correlation between the two SQUID signals is measured.

4.2 Operating Principle of the SQUID

The basic schematic of a dc SQUID [16] is shown in Figure 4.2(a). The dc SQUID consists of a superconducting loop with two Josephson junctions. The junctions represent points where the superconductivity is suppressed. The superconducting order parameters on both sides of the junctions are coupled according to the Josephson equations. A consequence of this is that a SQUID produces the current-voltage (I-V) characteristic shown in Figure 4.2(b). Below a critical current, I_c, there is no voltage developed across the device. Above I_c, the SQUID switches into the voltage state and approaches a straight-line, ohmic characteristic at very high currents. When magnetic flux is applied through the loop, the I-V curve shifts as indicated for $\Phi = (n + 1/2)\Phi_o$, where n is an integer. When $\Phi = n\Phi_o$, the curve returns to its zero-flux form, and subsequent increases in flux repeat the cycle.

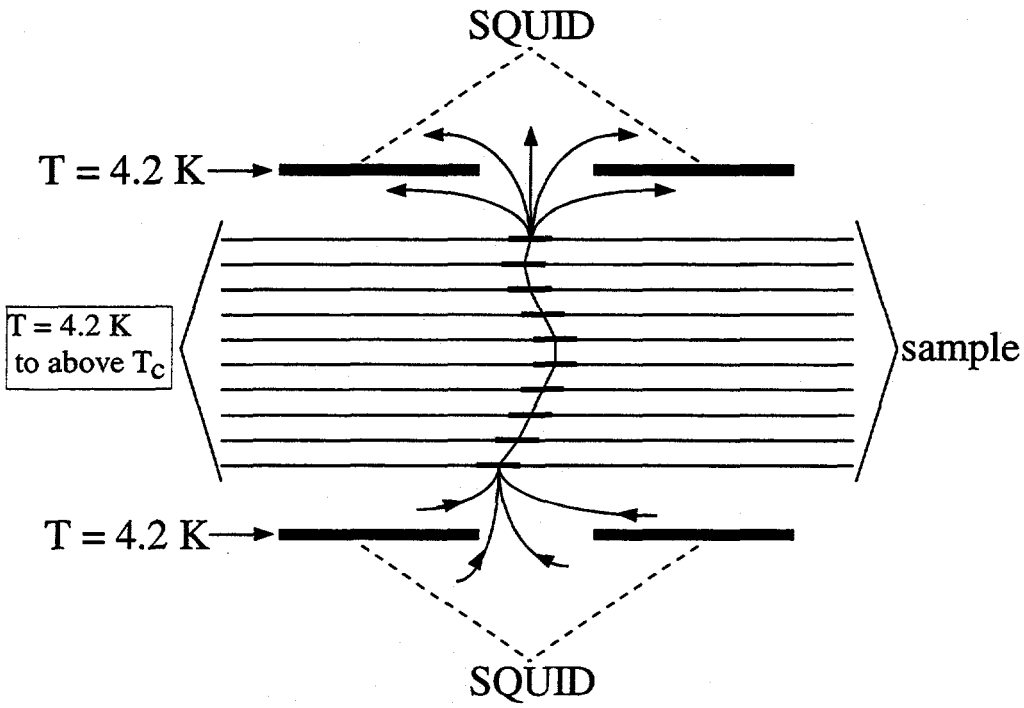

Figure 4.1: Concept of the double-SQUID measurement. The arrows indicate field lines leading to and from a vortex in a high-T_c sample. Not drawn to scale.

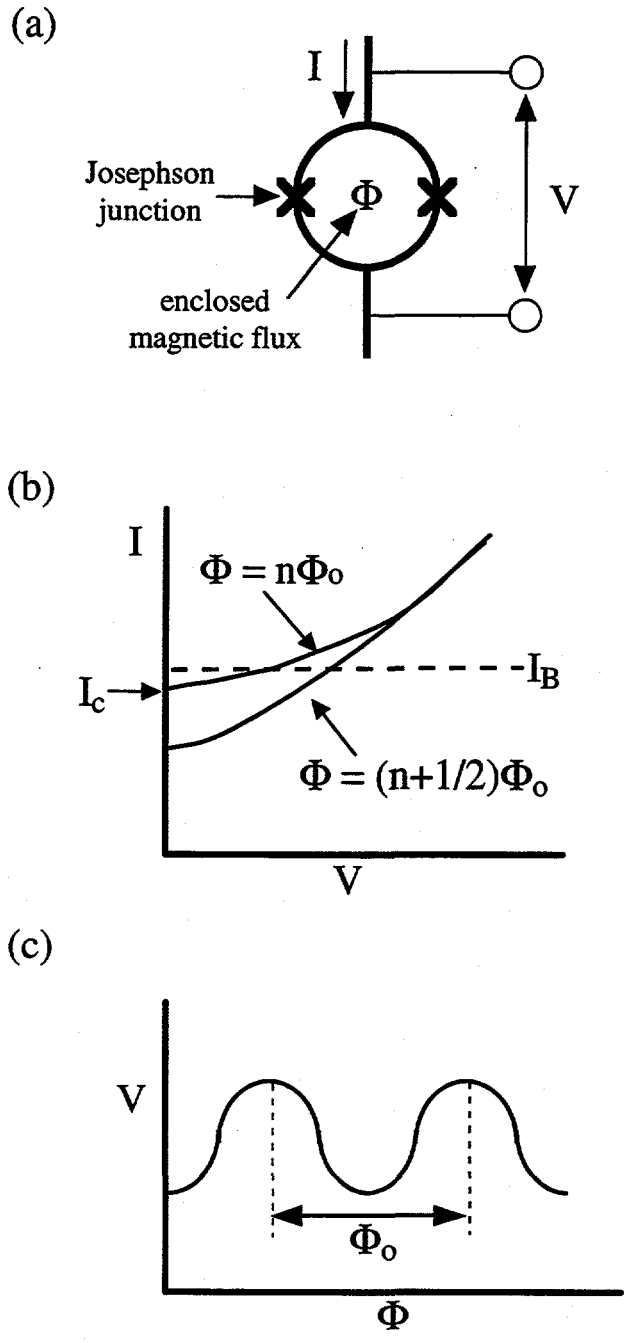

Figure 4.2: (a) Schematic of a dc SQUID. (b) Current-voltage characteristic. (c) Voltage-versus-flux curve.

Hence, if one fixes the current at the value I_B, indicated by the dotted line, then the voltage oscillates as a function of magnetic flux with period Φ_o, as shown in Figure 4.2(c). With appropriate SQUID control electronics, one can linearize the SQUID signal to achieve extremely high flux sensitivities on the order of a few $\mu\Phi_o/\sqrt{\text{Hz}}$.

4.3 Design and Fabrication of Low-Tc SQUIDs

The layout of our thin-film, low-T_c SQUIDs is shown in Figure 4.3. The niobium washer has outer dimensions 900 μm x 900 μm and hole dimensions 180 μm x 180 μm. The junctions are composed of Nb-NbO_x-PbIn sandwiches, each with an area of 2 μm x 2 μm. The dotted rectangle in the figure corresponds to an additional layer of superconducting PbIn which is separated from the washer by an insulating layer. This PbIn patch serves to shield the washer slit from external flux. This effectively transforms the SQUID pick-up area into the shape of a continuous square washer, which insures that the two SQUIDs in the measurement set-up can be adequately aligned with each other, as discussed in Section 4.4. A field modulation coil used by the SQUID control electronics (Section 4.5) is also patterned around each SQUID. The devices are fabricated on transparent sapphire substrates, which allow us to optically align two SQUIDs in the measurement cell by looking through the backside of one of the SQUID substrates. The SQUIDs operate at temperatures below 7 K.

The fabrication process for these SQUIDs basically follows that developed by others in our group for 2-inch-diameter silicon and sapphire substrates [17]. However, one major difference is that I fabricated the devices on 4-inch wafers. I switched to the 4-inch process because the photolithography equipment used for it provided cleaner definition of the junction areas, resulting in a much higher yield of working SQUIDs.

4.4 Measurement Cell

Figure 4.4 shows the essential components of the measurement cell, which is contained in a vacuum can that is immersed in liquid helium (T = 4.2 K). The vacuum, of course, is necessary to provide thermal isolation between the sample and the rest of the cell. In order to insure good flux coupling between the sample and each SQUID, it is crucial that the SQUID-sample distance be kept as small as possible. We managed to mount two SQUIDs (whose substrates are indicated by a in the figure) to within 100-200 μm of the

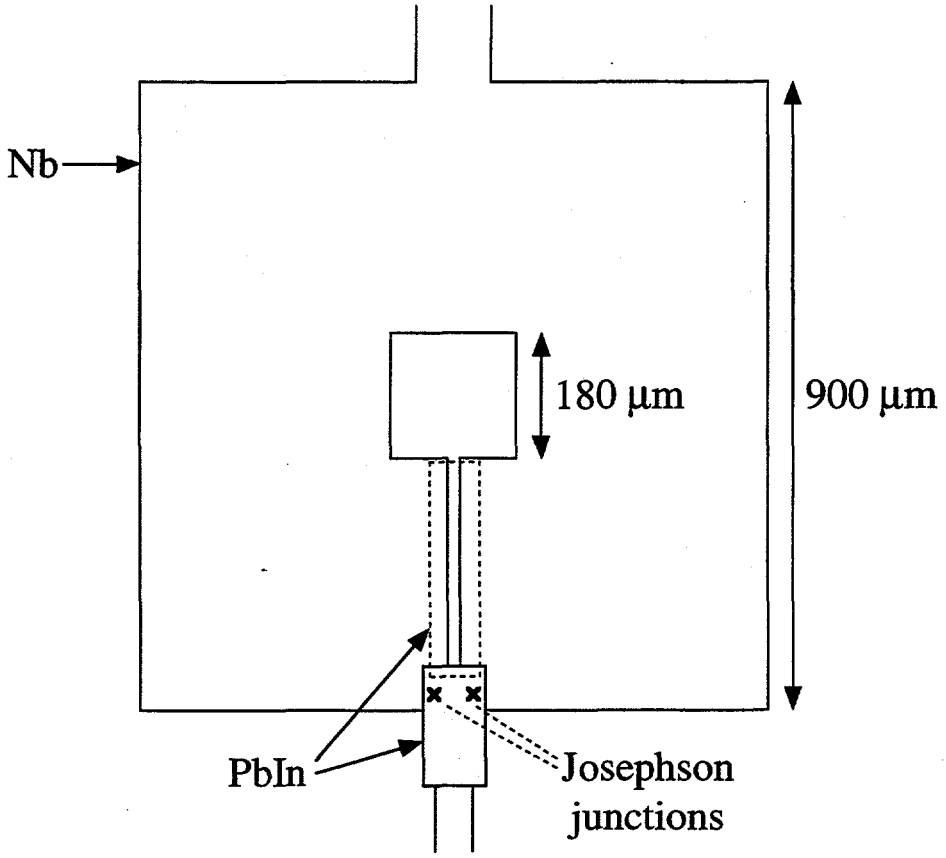

Figure 4.3: Layout of Nb-PbIn SQUID. The dotted rectangle represents an additional layer of PbIn, insulated from the Nb washer, which shields the slit from external flux.

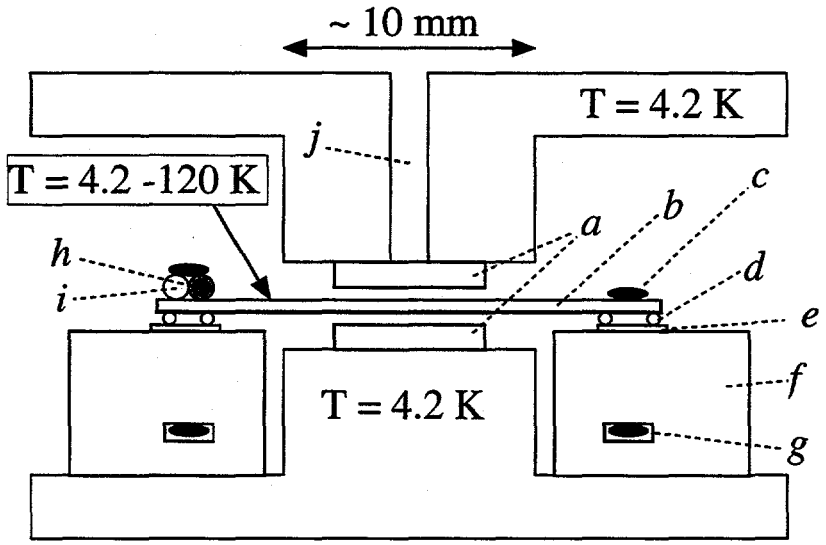

Figure 4.4: Cross-sectional view of the measurement cell. *a* SQUID substrates, *b* sample substrate, *c* dental floss, *d* nylon fiber, *e* alumina plate, *f* plastic stage, *g* hole in stage for dental floss, *h* platinum thermometer, *i* metal-film resistive heater, and *j* viewing hole for aligning the SQUIDs with respect to each other. Although the diagram is not drawn exactly to scale, the 10 mm scale bar gives approximate dimensions.

two opposing sides of the sample, which resides on either the upper or lower side of the sample substrate *b*. This was made possible by using sample substrates having thicknesses of less than 150 μm (see Section 4.6 for more details).

The two SQUIDs are rotated 180° with respect to each other in the horizontal plane so that the electrical contacts on one SQUID substrate do not touch those of the other. Since the SQUID pick-up areas are approximately two-fold symmetric, due to the PbIn patches covering the washer slits (see Section 4.3), the pick-up areas can still exactly mirror each other, despite the relative 180° in-plane rotation. As can be seen from Figure 4.1 on page 26, the validity of the correlation measurement relies on the fact that the two SQUID washers overlie and mirror each other, so that they measure the same region of the sample. We laterally aligned the SQUIDs with respect to each other by looking through the hole *j* under a microscope and in the absence of a sample. Since the SQUID substrates are attached to their respective mounts with GE varnish, which requires more than 12 hours to harden, we were able to nudge the substrates into alignment. Typically, we could align the SQUIDs to within ± 25 μm of each other along each lateral direction. We consider the effects on the measurement of this residual misalignment in Section 5.2.3.

The sample sits on top of thin nylon fibers *d* placed under each end. These fibers support the sample with only a very small total contact area, thereby reducing the net heat leak from the sample. The fibers rest on thin alumina plates *e* glued to the top of a plastic stage *f* which has a low thermal conductivity. Dental floss *c* is wrapped over each end of the sample and threaded through holes *g* in the stage in order to tie down the sample. This entire arrangement thermally-isolates the sample from the SQUIDs and the rest of the cell. The sample temperature is controlled and monitored by means of a metal-film resistive heater *i* and a platinum thermometer *h*. This assembly has allowed us to achieve very high temperature differences, on the order of 120 K, between the sample and the SQUIDs, while keeping the SQUIDs operational and the SQUID-sample distances less than 150 μm. Hence, we were able to perform measurements with the temperature of the sample raised well-above T_c.

In order to shield against external ac magnetic fields, a superconducting niobium sheath lines the inner surface of the vacuum can. The dc field of the earth is attenuated to less than 10^{-7} T by three cylindrical mu-metal shields surrounding the vacuum can. The entire dewar is placed inside a copper-mesh shielded room to attenuate radio-frequency noise.

4.5 SQUID Operation

A schematic of the SQUID control electronics is shown in Figure 4.5(a). A separate set of electronics is used for each SQUID with the exception of the oscillator (frequency $f_m = 500$ kHz), which is shared. The bias current, I_B, through the SQUID is chosen to maximize the amplitude of the voltage-versus-flux characteristic (the "V-Φ") of the SQUID. Figure 4.5(b) shows the operating principle of the electronics. Say that the total flux, Φ, through the SQUID is equal to $n\Phi_o$, where n is an integer, so that Φ is at a minimum in the V-Φ, as shown in the figure (the following explanation also holds for $\Phi = (n + 1/2)\Phi_o$, corresponding to a maximum of the V-Φ characteristic). Now impose an ac modulation flux, $\Phi_m(t)$, with a peak-to-peak amplitude of $\Phi_o/2$ at a frequency of f_m. This gives the time-varying SQUID voltage, $V(t)$, shown at the lower left of the figure. The important aspect of this response is it has no Fourier component at the modulation frequency f_m. Only even harmonics ($2f_m$, $4f_m$, etc) are represented. In Figure 4.5(a), the output of the mixer, V_{mixer}, is proportional to the in-phase f_m-fourier-component of the SQUID voltage. Hence, V_{mixer} is equal to zero when $\Phi = n\Phi_o + \Phi_m(t)$. However, say that the sample generates a flux fluctuation, Φ_{ext}, whose timescale is long compared to $1/f_m$ (a "quasistatic" fluctuation). This shifts the average flux away from the minimum in the V-Φ, as indicated in the figure, resulting in a different $V(t)$ which now has a non-zero fourier component at f_m, so that V_{mixer} is also non-zero.

We run the electronics in two modes, depending upon the desired measurement. The first mode is known as flux-locked-loop operation or "feedback mode". In this mode, the feedback switch [Figure 4.5(a)] is closed, so that V_{mixer}, after being integrated (or, equivalently, low-pass-filtered), is converted into a feedback current which is fed to the modulation coil. This causes the average flux to return to the minimum in the V-Φ, where the f_m-component is again zero, so that the quasistatic flux through the SQUID is "locked" at $n\Phi_o$ [or $(n+1/2)\Phi_o$]. The feedback current, which is proportional to Φ_{ext}, is converted to a voltage, V_{FB}, by a resistor and a buffer, as shown in Figure 4.5(a). Thus, V_{FB} is directly proportional to the flux generated by the sample.

The second mode of operation is called "open-loop mode", in which the feedback switch is open. The dc flux adjustment [Figure 4.5(a)] is manually set so that the average flux through the SQUID is as close as possible to an extremum of the V-Φ curve. This can be done only when the flux generated by the sample does not exhibit large changes (of order

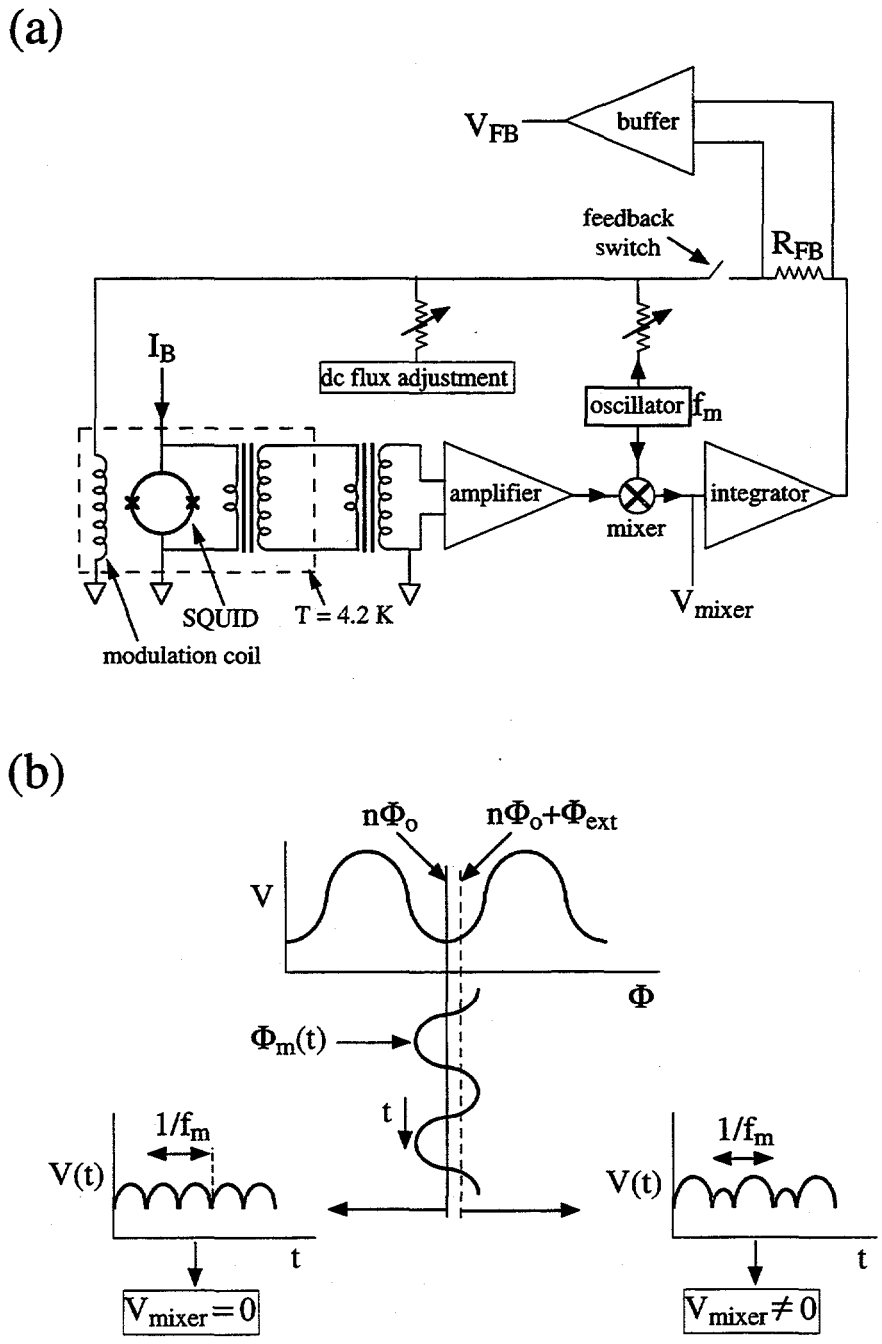

Figure 4.5: (a) Schematic of SQUID control electronics. (b) Principle of operation.

$\Phi_0/4$) over the duration of the measurement (this is usually the case, except near T_c where the sample flux fluctuations are particularly high). Since the feedback switch is open, no feedback flux is fed to the SQUID. We simply measure V_{mixer} to gauge the flux changes produced by the sample.

A main requirement for our experiment is that the SQUIDs operate independently. In other words, since the goal is to measure correlations in flux motion between both sides of the sample, the SQUIDs themselves must be uncorrelated with each other. Although feedback mode provides high linearity and good amplitude accuracy, two SQUIDs simultaneously operating with feedback can become coupled to each other. This occurs when the feedback current fed to the modulation coil of one SQUID (call it A) couples a significant amount of flux into the other SQUID (B). In this way, SQUID B senses a flux which is proportional to the flux originally sensed by SQUID A, thereby coupling the SQUIDs together. In our set-up, this coupling effect is significant when the magnetic shielding provided by the Meissner effect of the superconducting sample insufficiently screens the fields generated by the modulation coils. This happens when the temperature of the sample is above or near T_c, or when the sample area is comparable to or smaller than the SQUID area. In order to prevent cross-coupling, we use open-loop mode when operating both SQUIDs simultaneously under these circumstances. Since feedback is inactivated in open-loop mode, the SQUIDs are completely uncoupled.

The drawback of open-loop mode is that the output voltage, V_{mixer}, is strictly *nonlinear* in Φ_{ext}. The transfer coefficient, $dV_{mixer}/d\Phi_{ext}$, varies with the amount by which Φ_{ext} displaces the quasistatic flux from the nearest extremum in the V-Φ curve [Figure 4.5(b)]. Nevertheless, for sufficiently small variations in Φ_{ext}, V_{mixer} responds linearly to a very good approximation. As a check of this, I acquired data with each SQUID *separately* in feedback mode following each run in open-loop mode in which the fluctuations in the sample flux were particularly large. I then checked that the frequency dependence of the spectral density (proportional to the squared-magnitude of the fourier transform; precisely defined in Section 5.1.1) measured by each SQUID was the same in feedback mode as it was in open-loop mode. Any significant nonlinearities in the open-loop output voltage would manifest themselves as large distortions of the spectral density, due to mixing between different frequency components. For all the open-loop measurements presented here, no such nonlinear effects were apparent.

Another reason for supplementing the open-loop measurements with single-SQUID

feedback measurements is to measure the magnitude of the signal in absolute flux units. Due to the nonlinearity of the response in open-loop mode, it is very difficult to get an accurate measure of $dV_{mixer}/d\Phi_{ext}$, particularly when the fluctuations in flux from the sample are large. In contrast, the feedback-mode transfer coefficient, $dV_{FB}/d\Phi_{ext}$, is easily measured (see Section 5.1.4).

We performed the flux correlation measurements in an experimental bandwidth of 0.6 Hz to 2.5 kHz. The noise of each measurement channel was dominated by either the white noise of the preamplifiers in the SQUID electronics or by the intrinsic white noise of the SQUIDs themselves. This typically gave a noise floor of 10^{-10} to 10^{-9} Φ_o^2/Hz when operating in feedback mode.

4.6 Samples

We measured c-axis oriented BSCCO and YBCO samples, with parameters specified in Table 4.1. BSCCO (1) [18] and YBCO (1) [19] are thin films grown on $SrTiO_3$ and $SrTiO_3$-buffered-sapphire substrates, respectively. BSCCO (2) and (3) [20] and YBCO (2) and (3) [21] are single crystals. The crystal YBCO (3) had been irradiated with 1 GeV Au ions at a dose of 4.8×10^8 ions/mm^2 to introduce columnar defects along the c-axis [22]. For each sample, we obtained a measure of the diamagnetic shielding $S(T)$ ($0 \leq S \leq 1$) by determining the magnetic field required to induce one flux quantum in the SQUID; as the shielding decreases with increasing temperature, the required field is reduced (the precise definition of $S(T)$ will be given in Section 5.1.4). In Table 4.1, T_o is the temperature at which $S(T)$ vanishes. The T_c of the sample is roughly equal to T_o (we distinguish between these two since many authors refer to T_c as the transition temperature extracted from resistance-versus-temperature measurements).

The substrates of BSCCO (1) and YBCO (2) were polished down to their final thicknesses after deposition of the films. This was carried out in the following way. First, the film was protected by spinning on a thin layer of photoresist. Then, the substrate was mounted, film-side down, onto a polishing block with low-melting-temperature ($\approx$ 120 K) wax. Using fine diamond or alumina grit, ranging in size from 0.1 to 25 μm, the substrate was polished down to a thickness of less than 150 μm. Finally, the wax was dissolved by immersing the polishing block in a room-temperature acetone bath. This substrate-thinning procedure did not seem to harm the films, as the measured values for T_o were the same

before and after polishing.

The BSCCO and YBCO crystals were typically about 1-2 mm on a side, large enough to completely cover the areas of the SQUID washers. The crystals were mounted on commercially-available silicon substrates (Virginia Semiconductor, Inc.), each having a thickness of 75 μm. A very thin layer of silicone vacuum grease was used to attach each crystal to its substrate.

Sample	Type	Thickness(μm)	T_o(K)
BSCCO (1)	film	0.075	76
BSCCO (2)	crystal	4	88
BSCCO (3)	crystal	29	81
YBCO (1)	film	0.20	88
YBCO (2)	crystal	30	90
YBCO (3)	crystal	30	90

Table 4.1: Parameters of samples. T_o is the temperature at which the diamagnetic shielding vanishes. YBCO (3) has columnar defects.

Chapter 5

Results and Conclusions

5.1 Measurement Quantities

5.1.1 Definition of Flux Spectral Density

The output of the SQUID electronics, after multiplication by the appropriate voltage-to-flux transfer coefficient, yields the time-varying flux generated by the sample, $\Phi(t)$ (equal to Φ_{ext} in the preceding chapter; I drop the subscript for notational simplicity). By analyzing this signal with a spectrum analyzer, we obtain the spectral density of $\Phi(t)$, defined as:

$$S_\Phi(f) = \int_{-\infty}^{\infty} < \Phi(0)\Phi(t) > e^{-i2\pi ft} dt, \tag{5.1}$$

where f is the frequency, and $< \Phi(0)\Phi(t) >$ is the ensemble-averaged correlation function. $S_\Phi(f)$ is real-valued and is proportional to the square of the magnitude of the fourier transform. The flux spectral densities associated with SQUIDs A and B are $S_\Phi^A(f)$ and $S_\Phi^B(f)$, respectively.

5.1.2 Definition of Coherence Function

We analyze the correlations between the SQUID signals by obtaining the *coherence*:

$$\gamma^2(f) = \frac{|S_\Phi^{AB}(f)|^2}{S_\Phi^A(f) S_\Phi^B(f)}, \tag{5.2}$$

where $S_\Phi^{AB}(f)$ is the cross-spectral density defined by:

$$S_\Phi(f) = \int_{-\infty}^{\infty} < \Phi^A(0)\Phi^B(t) > e^{-i2\pi ft} dt. \tag{5.3}$$

The coherence $\gamma^2(f)$ varies from zero (no correlation) to unity (complete correlation). Our dual-channel spectrum analyzer (HP 3582A) calculates $\gamma^2(f)$ from the two SQUID outputs, $\Phi^A(t)$ and $\Phi^B(t)$.

5.1.3 Definition of the Relative Phase

Another useful function computed by our spectrum analyzer is the average relative phase difference, $\theta(f)$, between channels A and B at a given frequency. When $\gamma^2(f) = 0$, then the value of $\theta(f)$ randomly varies between 0 and 2π. When $\gamma^2(f) = 1$, then $\theta(f)$ settles at a single value; for example, $\theta(f) = 0$ indicates complete correlation between the signals, whereas $\theta(f) = \pi$ indicates complete *anti*-correlation.

5.1.4 Diamagnetic Shielding

In order to gauge the relative strength of the diamagnetic (Meissner) screening of the sample, we define a temperature-dependent diamagnetic shielding that varies between 0 and 1:

$$S(T) \equiv \frac{I_{\Phi_0}(T) - I_{\Phi_0}(T \gg T_c)}{I_{\Phi_0}(T \ll T_c) - I_{\Phi_0}(T \gg T_c)}, \tag{5.4}$$

where $I_{\Phi_0}(T)$ is the modulation-coil current necessary to couple one flux quantum into the SQUID at a given sample temperature T. Here, the coupling of interest is that between a coil and SQUID fabricated on the *same* substrate. When $T \ll T_c$, the sample exerts the maximum amount of diamagnetic shielding between the coil and the SQUID, so that $I_{\Phi_0}(T \ll T_c) = I_{\Phi_0}(max)$. Conversely, when $T \gg T_c$, the diamagnetic shielding is zero, so that $I_{\Phi_0}(T \gg T_c) = I_{\Phi_0}(min)$. Since we have two SQUIDs, there are two values for $S(T)$ at each temperature, which typically agree within experimental error. However, one SQUID is usually placed somewhat closer to the sample than the other, so that it has a larger value of the difference $I_{\Phi_0}(T \ll T_c) - I_{\Phi_0}(T \gg T_c)$. This means that $S(T)$ is measured more precisely with this SQUID than with the other. Hence, in the rest of Part I, the values quoted for $S(T)$ are those for the SQUID which is closer to the sample. As mentioned in Section 4.6, we define T_o as the temperature at which $S(T)$ vanishes. The T_c of the sample is very close to T_o, but we make the distinction in order to prevent confusion with values of T_c extracted from resistance-versus-temperature curves.

Incidentally, the measurement of $I_{\Phi_0}(T)$ necessary for deducing $S(T)$ also yields

the flux-to-voltage transfer coefficient for feedback-mode operation of each SQUID:

$$dV_{FB}/d\Phi_{ext} = I_{\Phi_0}(T)R_{FB}g \text{ (units of V}/\Phi_o), \tag{5.5}$$

where $I_{\Phi_0}(T)$ is in units of A/Φ_o, R_{FB} is the resistance of the feedback resistor (see Figure 4.5(a) on page 33) in units of ohms, and g is the gain (always unity in our measurements) of the buffer monitoring the voltage across the feedback resistor.

5.2 Results

When the sample is cooled in a low applied magnetic field ($< 10^{-7}$ T), vortex-antivortex pairs are generated at the superconducting transition; as the sample is cooled further, most of these vortices annihilate, but some are pinned and may hop among pinning sites under thermal activation. As discussed in Section 2.2.2, the characteristic time interval for this process is $\tau = \tau_o exp[U(T)/k_BT]$, where τ_o is an attempt frequency and $U(T)$ is the temperature-dependent pinning energy. This motion generates magnetic flux noise that is detected by the SQUIDs. We emphasize that each cooling process generates a different vortex configuration and thus possibly a different behavior at a given temperature. In general, we observe two distinct types of behavior [3]. The first consists of random telegraph signals (RTSs), in which the flux jumps randomly between two distinct values. The second is $1/f$ noise, where the spectral density scales as $1/f^\alpha$ with α close to unity, which is produced by an incoherent superposition of RTSs. At each temperature, RTSs produced by vortices with pinning energies within about k_BT of a characteristic energy $\tilde{U}_o(\omega, T) = k_BT\, ln(1/\omega\tau_o)$ contribute predominantly to the spectral density of the flux noise at frequency ω. Assuming $\tau_o = 10^{-10}$ sec, we find $\tilde{U}_o = 21k_BT$ for $\omega/2\pi = 1$ Hz. Thus, as the temperature is changed, different pinning sites with appropriate pinning energies are brought into the observable frequency range.

5.2.1 Random Telegraph Signals

Figure 5.1 shows the time traces of two RTSs, in two different crystals, each measured simultaneously by the two SQUIDs. Also shown are the corresponding and average relative phases of each set of time traces[1]. In Figure 5.1(a) [YBCO (2)], the two time traces

[1]The frequency range has been cut off above 12 Hz. At higher frequencies, the white noise of the SQUID becomes significant, reducing the observed coherence.

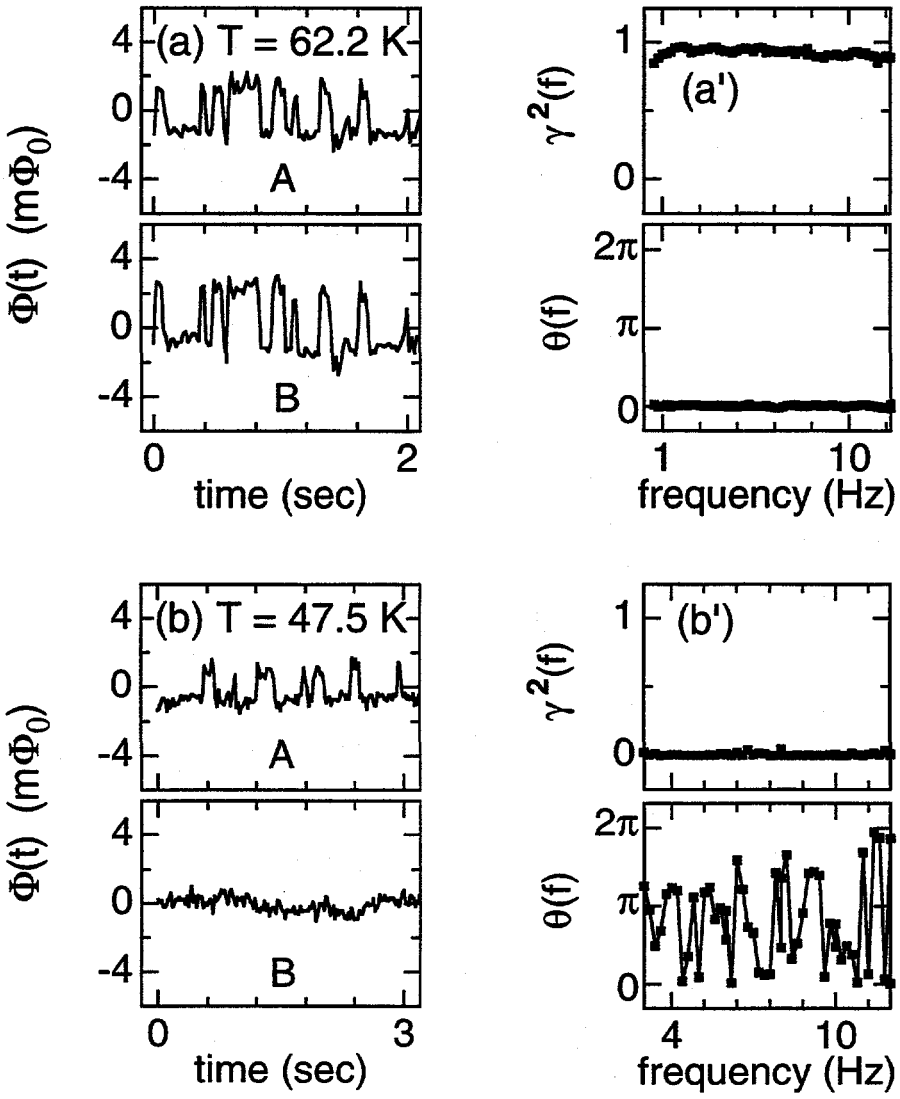

Figure 5.1: Random telegraph signals detected by SQUIDs A and B for (a) YBCO(2) and (b) BSCCO(2); the corresponding coherences $\gamma^2(f)$ and relative phases $\theta(f)$ are shown in (a′) and (b′), respectively.

show considerable correlation; this observation is confirmed in (a'), where $\gamma^2(f)$ is essentially unity and $\theta(f)$ is zero. We interpret this result as the hopping of a single vortex as a rigid rod between two pinning sites separated by at least 1.3 μm [3]. We have observed comparable correlated RTSs in all of the BSCCO and YBCO crystals, and conclude that the rigidity of the vortices in both materials is high at least for timescales greater than 0.01 sec. In all the crystals over certain temperature ranges we also observe RTSs on one side with no corresponding RTSs on the other, so that $\gamma^2(f)$ is zero and $\theta(f)$ is randomly distributed; an example is shown in Figure 5.1(b). This process is consistent with a vortex line that is strongly pinned near one end while the other end hops between two pinning sites.

For a given RTS, the hopping rate varies rapidly with temperature, so that it is observable only over a restricted temperature range. Thus, one typically observes a number of different RTSs over the temperature range of the experiment. For the 24 RTSs in the BSCCO and YBCO crystals we have studied, there were 11 correlated and 13 uncorrelated processes, indicating that both types occurred with approximately equal probability.

5.2.2 1/f noise

We turn now to a discussion of $1/f$ noise, which we observed in all samples at temperatures below the transition over the frequency range 0.6 Hz to 2.5 kHz, except over the narrow temperature ranges in which RTSs occurred. Figure 5.2 shows a representative example, for YBCO(2) at 89.7 K with $S = 0.9$. The spectra measured by the two SQUIDs have slopes very close to -1 over the frequency range shown, 1 - 100 Hz, and $\gamma^2(f)$ is nearly white, with an average value $< \gamma^2 > = 0.35$.

We next briefly discuss the results from the thin films. Clem [23] has shown that when $\lambda_{ab}(T)$ exceeds the sample thickness, the motion of a pancake vortex at one surface will produce a nearly equal flux in both SQUIDs, giving a high degree of coherence. In Figure 5.3(a) we plot $< \gamma^2 >$ versus temperature for films YBCO(1) and BSCCO(2) both with thicknesses less than or comparable to $\lambda_{ab}(T)$ (λ_{ab}(YBCO) $\approx$ 1400 Å and λ_{ab}(BSCCO) $\approx$ 2000 Å for the temperatures shown); in both cases $S \geq 0.9$. The average $< \gamma^2 >$ is taken over the frequency range where $\gamma^2(f)$ is frequency-independent[2]. The values of $< \gamma^2 >$ are essentially unity, with no temperature variation. This result is consistent with Clem's

[2]Any frequency dependence of $\gamma^2(f)$ is usually caused by uncorrelated SQUID noise that becomes significant at frequencies where the sample noise is low

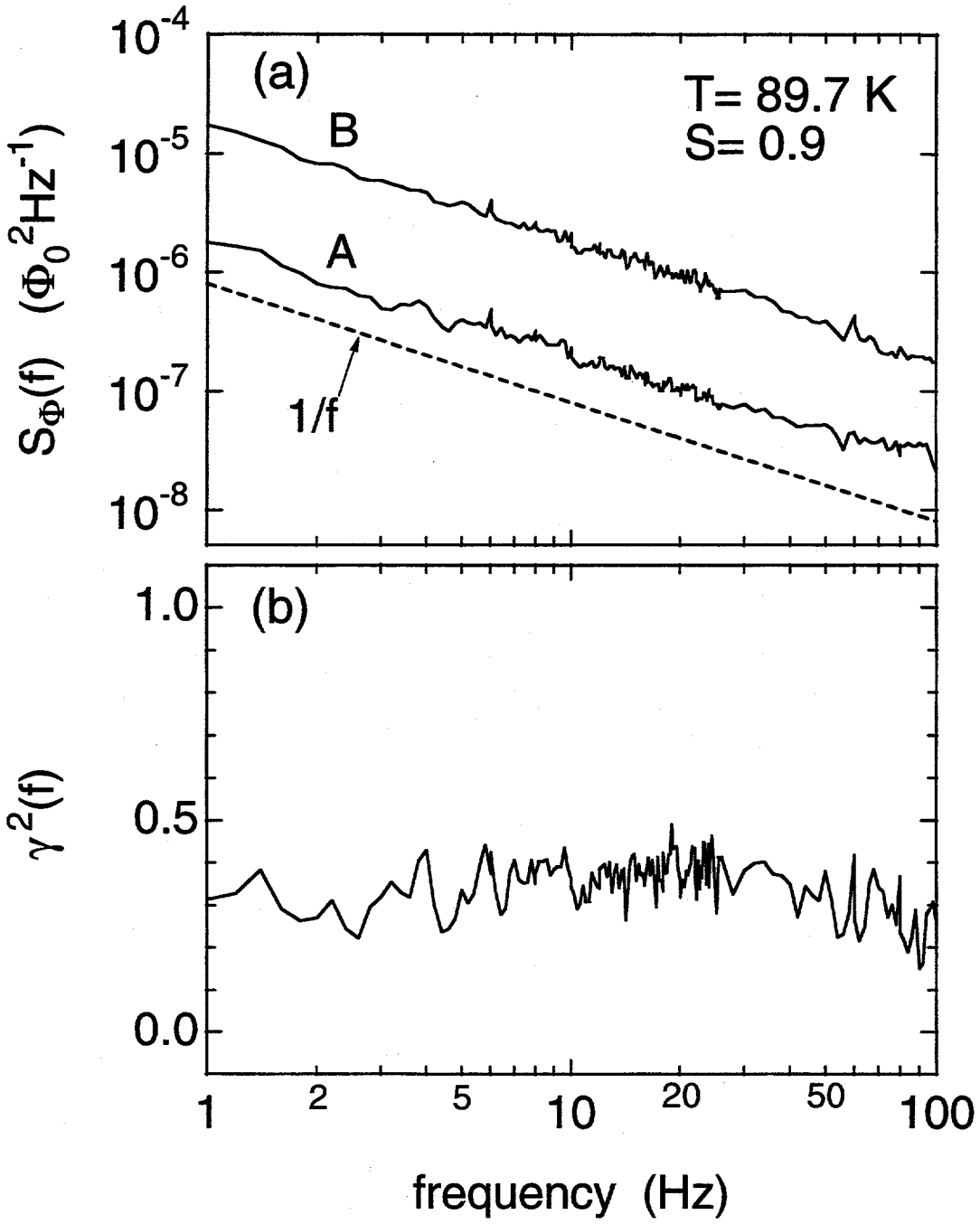

Figure 5.2: (a) Spectral density of $1/f$ noise in YBCO(2) at 89.7K, with $S(T) = 0.9$, measured by SQUIDs A and B; (b) $\gamma^2(f)$ for the two spectra in (a).

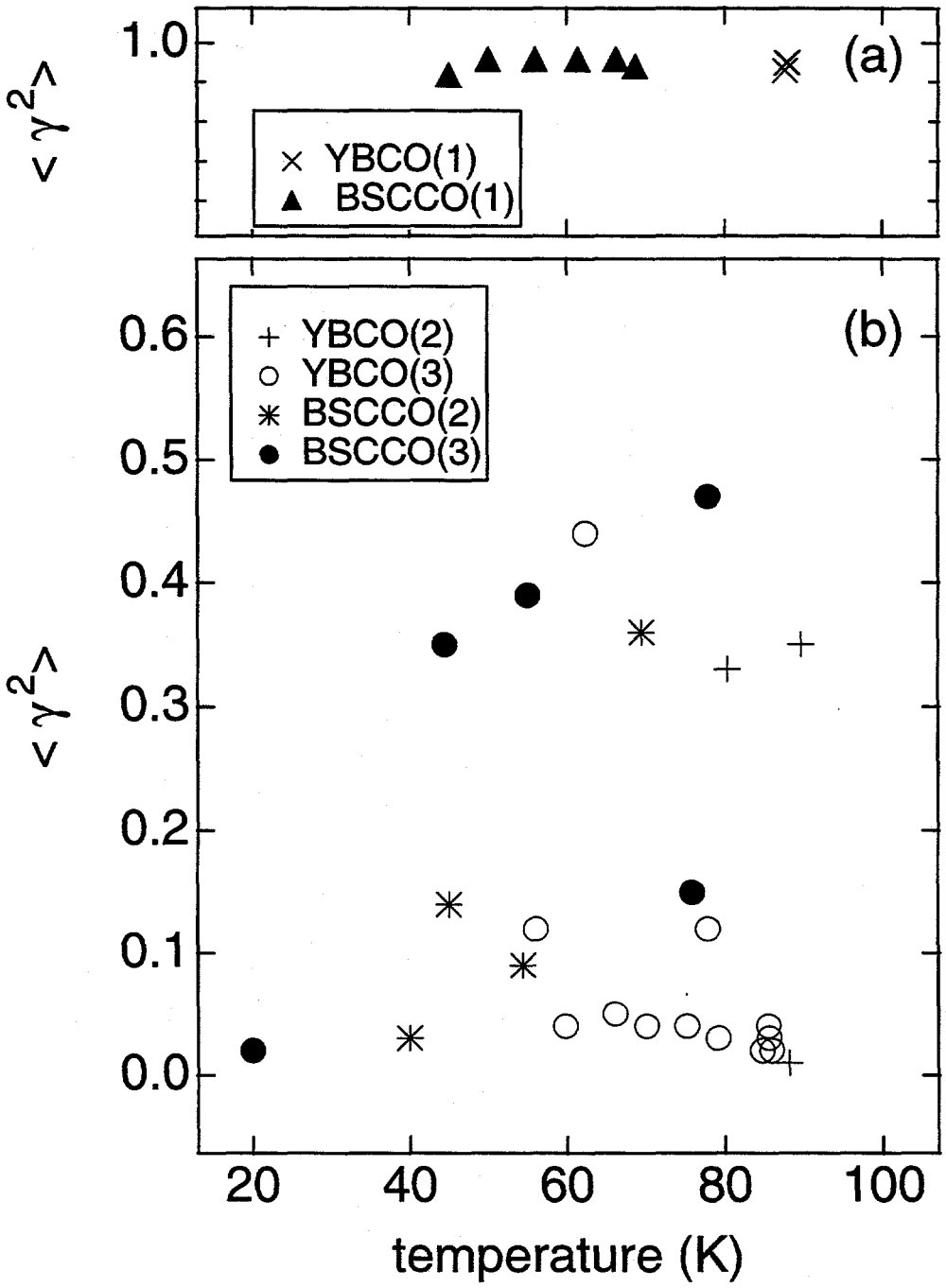

Figure 5.3: $< \gamma^2 >$ vs. temperature for $S \geq 0.9$ for (a) thin films and (b) thick crystals. The data for each sample were obtained from 2 to 4 separate thermal cyclings through T_c.

prediction, but does not resolve the issue of whether the vortices move as rigid rods or as independent pancakes, since both yield high coherence in the thin film limit.

Turning to the four crystals, we confine our attention to temperatures for which $S \geq 0.9$, thereby excluding temperatures near T_o where $\lambda_{ab}(T)$ becomes greater than the sample thickness. In Figure 5.3(b) we show $< \gamma^2 >$ vs. temperature obtained from 2 to 4 thermal cyclings of each of the four samples. We note that many of the plotted values are near zero; however, the associated values of $\theta(f)$ are typically within $\pm 50°$ of $0°$, implying that the coherence, although small, is indeed nonzero. In other cases $< \gamma^2 >$ is as high as 0.4. If we assume that each vortex has a probability p to hop in a highly correlated manner [Figure 5.1(a)] and $1 - p$ in an uncorrelated manner [Figure 5.1(b)], then it can be shown that $\gamma^2(f) = p^2$ for the ensemble of RTSs generating $1/f$ noise. Thus, the value of $< \gamma^2 > = 0.4$ for $1/f$ noise suggests that about 60% of the vortices are moving as rigid rods at any given moment, while if we take a typical low value, $< \gamma^2 > = 0.05$, about 20% have rigid rod behavior. Thus, even for $1/f$ noise with values of $< \gamma^2 >$ as low as 0.05, a significant fraction of the vortices contributing to the noise must have correlated motion.

A perusal of Figure 5.3(b) shows that for a given sample $< \gamma^2 >$ has no systematic temperature dependence. Since the $1/f$ noise in a given frequency interval arises from progressively weaker pinning sites as the temperature is lowered, this result indicates that p is not a monotonic function of the pinning energy. Furthermore, each thermal cycling yields a different value of $< \gamma^2 >$ at a given temperature, suggesting that processes with a given pinning energy have a variety of values of p. There is no significant difference between the coherence for the 4 μm and 29 μm thick BSCCO crystals, and no evidence for the coherence being higher in YBCO than in BSCCO, despite the fact that the predicted overall coupling energy between pancake vortices in adjacent layers is at least 20 times higher in YBCO. This behavior is complementary to results obtained in the transport measurements on BSCCO [13, 14], in which the force due to the current drives the vortices unidirectionally, causing them to shear. Lastly, the coherence in the columnar-defect YBCO crystal is similar to that observed in the other crystals, while its transport properties are vastly different [22].

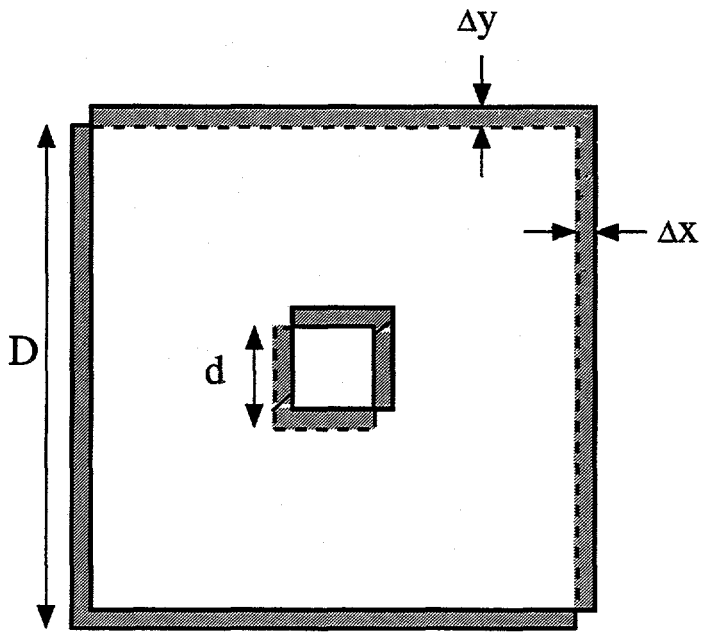

Figure 5.4: SQUID misalignment. Hatched region corresponds to the misalignment area, $A_{misalign}$.

5.2.3 Potential Effects of SQUID Misalignment on Coherence Measurements

As discussed in Section 4.4, the SQUIDs can be aligned with each other within about $\pm 25\ \mu$m along each lateral direction. We must consider the potential impact of this misalignment on the coherence measurements. The misalignment raises the possibility that a vortex, moving as a rigid rod, would be sensed by one SQUID, but barely at all by the other. This could substantially reduce the measured γ^2 below its true value. In order to estimate the potential effect, let us define the area of misalignment, $A_{misalign}$, as the area of the sample overlapping only one SQUID (the hatched regions in Figure 5.4). For misalignments of Δx and Δy, we have $A_{misalign} = 2(D+d)(\Delta x + \Delta y) - 4\Delta x \Delta y$, where D and d are the inner and outer washer dimensions, respectively. The sensitive area of each SQUID *excludes* the hole, since a vortex under the middle of the hole does not cause a flux change when it moves by a small amount; essentially all of its flux is captured by the hole both before and after it moves. In contrast, the flux from a vortex positioned under the body of the SQUID washer is coupled into the SQUID hole by varying amounts, depending on its radial position with respect to the center of the SQUID. The total area of the sample sensed by either of the two SQUIDs, A_{sense}, is equal to the sum of the misalignment area and the overlap area between the SQUIDs. From Figure 5.4, we derive $A_{sense} = (D+\Delta x)(D+\Delta y) - (d-\Delta x)(d-\Delta y)$. Finally, let us assume that any vortex which lies in a misalignment region is sensed by only one SQUID, so that its motion contributes an uncorrelated (zero-coherence) signal.

In the case of RTSs, if one assumed that *all* such events were actually due to rigid-rod vortex hopping [Figure 5.1(a)], then one would expect that a fraction $A_{misalign}/A_{sense}$ would be mistakenly measured as *uncorrelated* RTSs [Figure 5.1(b)] due to SQUID misalignment. The ratio $A_{misalign}/A_{sense}$ is simply the probability that a given vortex resides in a misalignment region, where only one SQUID can sense it. For $\Delta x = \Delta y = 25\ \mu$m, $D = 900\ \mu$m, and $d = 180\ \mu$m, we find $A_{misalign}/A_{sense} = 0.13$. In contrast, we actually found about half of the RTSs to exhibit uncorrelated behavior. Hence, we believe that the observation of single-ended vortex-hopping [such as that in Figure 5.1(b)] is not an artifact of SQUID misalignment. However, we cannot say with certainty that a *particular* uncorrelated RTS is not due to SQUID misalignment.

For $1/f$ flux noise, let us assume that all the vortices and pinning sites are uni-

formly distributed throughout the sample. Then, if we measure $\gamma^2_{measured}$, the actual value is $\gamma^2_{actual} = [A_{sense}/(A_{sense} - A_{misalign})]\gamma^2_{measured}$. Again, the assumption is that vortices lying in the misalignment regions are measured to have zero-coherence. The scaling factor in brackets is the ratio of the full sensing area to the overlap area between the SQUIDs. Given the parameters in the previous paragraph, we find $\gamma^2_{actual} = 1.15\gamma^2_{measured}$ for the worst-case misalignment. So the coherence values quoted above for $1/f$ noise have an upper error bar of +15%, except when $\gamma^2_{measured} > 0.87$ (since the coherence cannot exceed unity).

5.3 Conclusions

The data show that flux vortices as long as 30 μm along the c-axis in crystals of YBCO and BSCCO, cooled in nominally zero magnetic field and in the absence of any driving current, can exhibit coherent motion for time scales greater than 10^{-2} sec. The observation of both RTSs and $1/f$ noise indicate that typically 20 to 60% of the vortices exhibit such coherence. Both YBCO and BSCCO exhibited similar behavior, and there is no discernible dependence of the degree of coherence on sample thickness, temperature (provided $\lambda_{ab}(T) \ll$ sample thickness and $T < 0.9T_c$) or the presence of columnar defects. We interpret these results to imply that the differences between coherent and incoherent motion appear to be due to the distribution of pinning energies along the axis of the flux line. When the flux line is pinned at a single site with a given pinning energy, it hops to another site as a rigid rod when given enough thermal energy. This means that thermal fluctuations alone are insufficient to disrupt the stack of pancake vortices, so that the lateral motion of a pancake at one point on a vortex can be transmitted to another point thousands of lattice spacings away.

Conceivably, if the vortex is pinned at two or more sites with comparable energies, hopping at one site could induce hopping at another site. In contrast, when the flux line is pinned by at least one site with a much stronger pinning energy than any other pinning site along its length, then only part of the flux line is free to move at a given temperature, thereby producing incoherent motion. Thus, the flux lines in YBCO and BSCCO are flexible enough to bend at points of strong pinning, yet rigid enough to resist shearing due to thermal fluctuations. Finally, we believe that any effect of columnar defects on the coherence does not appear at low vortex densities because the vortices whose motion we observe are mainly those pinned by native defects.

5.4 Future: Magnetic Field Studies

The main limitation of the present set-up is that there is no provision for applying a large (greater than 1 gauss) magnetic field to the sample. The ability to apply a field could yield further insight into flux dynamics in two ways. First, by increasing the number density of vortices, one should be able to fill with vortices a substantial number of the artificial pinning sites in samples having columnar defect, which would allow the SQUIDs to probe the effects of this type of pinning on vortex rigidity. Second, if one could increase the field to values such that vortices begin to interact with each other, then special phases such as the vortex fluid [24] and the vortex glass [25] could be explored. One technical consideration at very high applied fields is that the SQUIDs cannot operate above 0.1 T, as this exceeds the critical field of niobium (in fact, the junctions probably would become unoperational at much lower fields). Hence, one would need to keep the SQUIDs in a region outside of the large field and use NbTi flux transformers as the pick-up elements.

Part II

High-Tc SQUID Microscope for Room Temperature Samples

Chapter 6

Introduction to SQUID Microscopes

In recent years there has been substantial growth in the use of the dc SQUID as a "scanning SQUID microscope" in which a sample is scanned in close proximity to the SQUID to produce a two-dimensional magnetic field image [26]. Broadly speaking, these devices can be split into two classes, one with the sample at the temperature of the SQUID ("cold sample") and the other with the sample at room temperature ("warm sample"). Furthermore, although the original microscopes involved low transition temperature (Tc) SQUIDs, more recently high-Tc SQUIDs have been successfully used. Examples of the use of cold sample microscopy at helium temperatures include the study of vortex structure and dynamics in superconducting networks and clusters [27] and the determination of the pairing symmetry in high-Tc superconductors [28, 29, 30]. Black and co-workers have pioneered the use of high-Tc SQUIDs operated at liquid nitrogen temperature to examine cold samples with a variety of techniques, including static magnetization [31], eddy current [32], radio frequency [33], and microwave imaging [34]. Low-Tc SQUID microscopes have been used extensively for nondestructive evaluation (NDE) of warm samples in many different modes [26], and a number of different systems have been described [35, 36, 37, 38]. More recently, high-Tc systems for NDE of room temperature samples have been introduced [39, 33].

A crucial parameter relevant to all SQUID microscopes is the separation z between the SQUID and the sample. Under optimum circumstances, the best spatial resolution[1] that

[1]By "spatial resolution" we mean the smallest separation of two magnetic objects (for example, tiny bar magnets) placed side by side. One can often detect a displacement of a magnetic source – for example, a

can be achieved for the image of a magnetic object is approximately equal to z, although the relative sizes of the object and the SQUID and the noise of the SQUID also play roles [40]. Thus, the great advantage of cold sample microscopes is that the SQUID can be brought into physical contact with the sample, allowing one to achieve values of z as low as a few micrometers. Obvious disadvantages of cold sample microscopes are that the sample size is constrained and that the time required for thermally cycling is necessarily long. Furthermore, samples that have to be maintained at room temperature and pressure cannot be examined. In warm sample microscopes, the usual practice is to mount the SQUID in vacuum on a cold finger and bring it as close as possible to a thin window, on the outside of which one places or scans the sample. The major thermal load on the SQUID (or flux transformer coupled to it) is due to blackbody radiation from the window. In the case of low-Tc SQUIDs, this thermal load generally requires one to place a radiation shield between the window and the SQUID, thereby increasing z. To our knowledge, the smallest value of z achieved in a system of this kind is 0.85 mm [38]. On the other hand, the much higher operating temperature of high-Tc SQUIDs implies that a radiation shield is no longer required, so that the SQUID can be brought substantially closer to the window. Recently, Black and co-workers [41] developed a high-Tc microscope in which the SQUID can be brought to within 40 μm of a room-temperature object placed beneath it. This major reduction in z compared with what has been achieved with low-Tc SQUIDs offers a substantial improvement in spatial resolution of room temperature samples.

I describe the design, construction, performance and applications of a high-Tc, warm sample microscope in which the SQUID-sample distance is as small as 15 μm. In contrast to previous SQUID microscopes, the vacuum window is situated above the SQUID. This configuration enables one to place a sample, which may be immersed in water if it is biological, directly on the window, in order to minimize its separation from the SQUID.

---

magnet or a current carrying wire – that is vastly less than z. In this case, the smallest detectable change in position is the rms flux noise of the SQUID in a given bandwidth divided by an appropriate magnetic field gradient produced by the source at the SQUID.

Chapter 7

Design and Construction

7.1 Basic Design Scheme

The essential task of the microscope is to maintain a SQUID at 77K as close as possible to a sample at room temperature and pressure. To accomplish this, the SQUID is mounted in vacuum at the end of a cold finger which is thermally anchored to a can of liquid nitrogen. A thin vacuum window separates the SQUID and the sample. The position of the window can be adjusted to reduce its separation from the SQUID to less than 10 μm. The sample is either placed directly on the window or raster-scanned over the SQUID by a two-dimensional scanning stage. To eliminate external noise the entire microscope is surrounded by three layers of mu-metal. In the following sections we discuss in turn the design considerations and construction of the vacuum window, the SQUIDs, the dewar, the scanning stage, the magnetically-shielded enclosure, the SQUID electronics, and the data acquisition system.

7.2 Vacuum Window

7.2.1 Window Design

The parameters of the vacuum window play a large role in determining how small one can make z. Assuming a planar sample, one can write

$$z = t + g + b, \tag{7.1}$$

where t is the thickness of the window, g is the vacuum gap between the window and the SQUID and b is the bow in the window due to the pressure differential (Figure 7.1).

Reducing the gap g clearly reduces z, but the trade-off between t and b is more subtle, since for a given window area a reduction in t always increases b. To minimize $b + t$ we consider a circular window with radius a; we neglect the possible influence of residual stresses in the material resulting from its manufacture [42]. By minimizing the total deflection energy for a rigidly fixed boundary [43], one finds that b and t satisfy the approximate relation

$$(1 + 0.488b^2/t^2)b/t = 0.188P(1 - \nu^2)a^4/Et^4. \tag{7.2}$$

Here, P is the pressure difference across the window, ν is Poisson's ratio, and E is Young's modulus. The b^2 term arises from the energy required to stretch the bowed window along its surface; when $b \ll t$, this term is negligible, and one finds $b \propto a^4/t^3$, which is the well-known result for small deflection bending [43]. In the opposite limit $b \gg t$, the stretching energy dominates and $b \propto a^{4/3}/t^{1/3}$, which is a much weaker dependence on a and t. Equation 7.2 is a cubic equation for b which one can solve analytically for $b(t)$. The sum $b(t) + t$ is minimized for the optimum thickness t_{opt} which must be found numerically for specified values of P, ν, E and a.

It is clear from Equation 7.2 that one should strive to reduce a in order to decrease the bow for a given window thickness and thus achieve a lower value of z. However, for the configuration shown in Figure 7.1(a), the window must encompass the chip on which the SQUID is grown to enable one to bring the two surfaces as close as possible to each other. Thus, the window diameter cannot be smaller than the largest dimension of the chip. Smaller transverse dimensions also imply that any tilt between the chip and the window due to imperfect alignment becomes less critical. Hence, the key to achieving lower values of z is to make the SQUID chip as small as possible.

The choice of material for the window is dictated by the need for high elastic modulus, a low electrical conductivity to eliminate Johnson noise (see Section 7.4.1), and optical transparency to enable one to center the SQUID chip under the window. We first chose single-crystal sapphire. We decided on a diameter of 5 mm to accommodate SQUID chips up to about 3 mm on a side. Using $a = 2.5$ mm, $E = 345$ GPa and $\nu = 0.3$ we have computed $b(t) + t$, which we plot vs. t in Figure 7.1(b). As expected, $b + t \propto t$ for $b \ll t$, and $b + t$ increases as t is reduced for $t \ll b$. The minimum value $b + t \approx 62\ \mu$m occurs

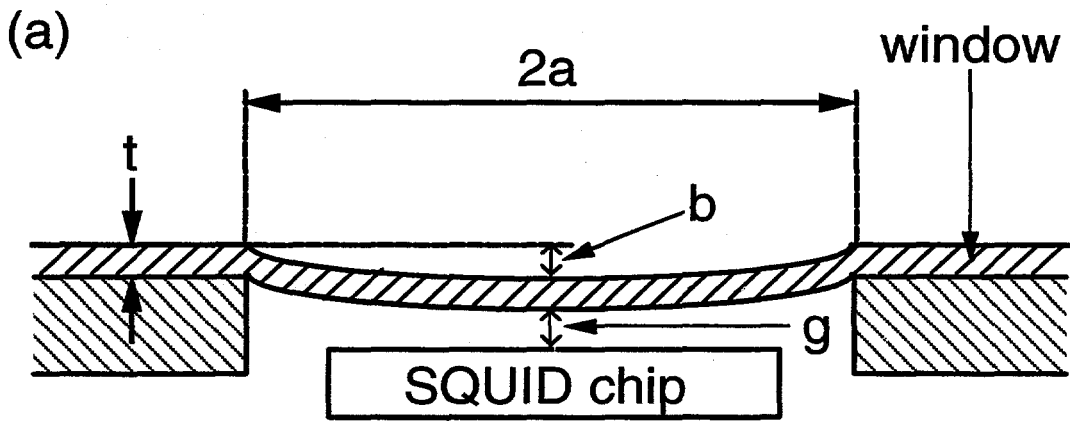

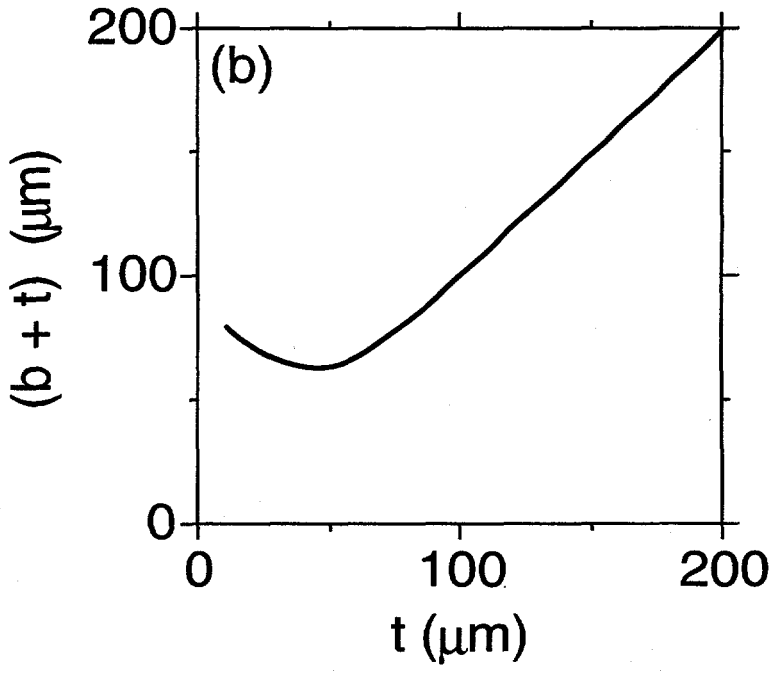

Figure 7.1: (a)Cross section of vacuum window of radius a and thickness t (not to scale); g is the vacuum gap and b the bow. (b) Predicted values of $b(t) + t$ for the sapphire window with $a = 2.5$ mm.

at $t_{opt} \approx 45\ \mu$m. We were able to obtain readily a 75 μm-thick window (Crystal Systems, Inc.), for which we predict $b \approx 4\mu$m and $b + t \approx 79\mu$m, a value that is 17 μm greater than the value we predict for t_{opt}. Using a microscope, we measured the actual bow to be $9 \pm 2\ \mu$m, two times higher than the predicted value.

In order to achieve even smaller values of $b+t$, we also used silicon nitride (Si_xN_y) as a window material. Si_xN_y has a high elastic modulus (≈ 245 GPa) [42], is an electrical insulator, and is optically transparent at thicknesses of interest (several micrometers). Furthermore, it is easily microfabricated into thin square membranes on silicon substrates, as described in Section 7.2.2. Others have measured and modeled the dependence of the bow on t, the areal dimensions, and the pressure across it [42]. I used these results to estimate that a window of thickness 3 μm and area 400 μm x 400 μm should yield $t + b$ less than 10 μm. Exact calculation is difficult because material parameters such as the elastic modulus and the residual stress differ depending on the exact Si_xN_y processing conditions. The dimensions of the fabricated windows were 440 μm x 440 μm x 3.2 μm-thick. The measured bow is 2 μm under atmospheric pressure, so that $t + b$ is only 5 μm, about 17 times smaller than that of the sapphire window.

7.2.2 Window Fabrication

The circular sapphire window was assembled in the following way (the slanted part letters refer to Figure 7.8(a) inset on page 72). A 75-μm-thick sapphire disk *c* is glued (Stycast 1266) to a 250 μm-thick quartz or silicon ring *d* with inner and outer diameters of 5 mm and 15 mm. This ring, in turn, is glued to the end of a quartz tube *e*. As a precaution against air leaking into the vacuum system in the event of a crack in the sapphire window, a 2.5 μm mylar sheet is stretched over it and sealed against the side of the tube with vacuum grease and a rubber band *f*. The tube is glued into an acrylic ring *g* which is clamped with nylon screws into an o-ring-sealed socket on the microscope; the entire window assembly can be easily removed by loosening the screws. As mentioned before, the measured bow of this window is $9 \pm 2\ \mu$m.

I fabricated the silicon nitride windows using a conventional micromachining process (Figure 7.2) [42]. In Step 1, Si_xN_y is deposited to a thickness of about 3 μm using low-pressure chemical vapor deposition (LPCVD) onto both sides of a (100)-oriented, 100-mm-diameter P-type silicon wafer. Square windows in the Si_xN_y are then opened on the

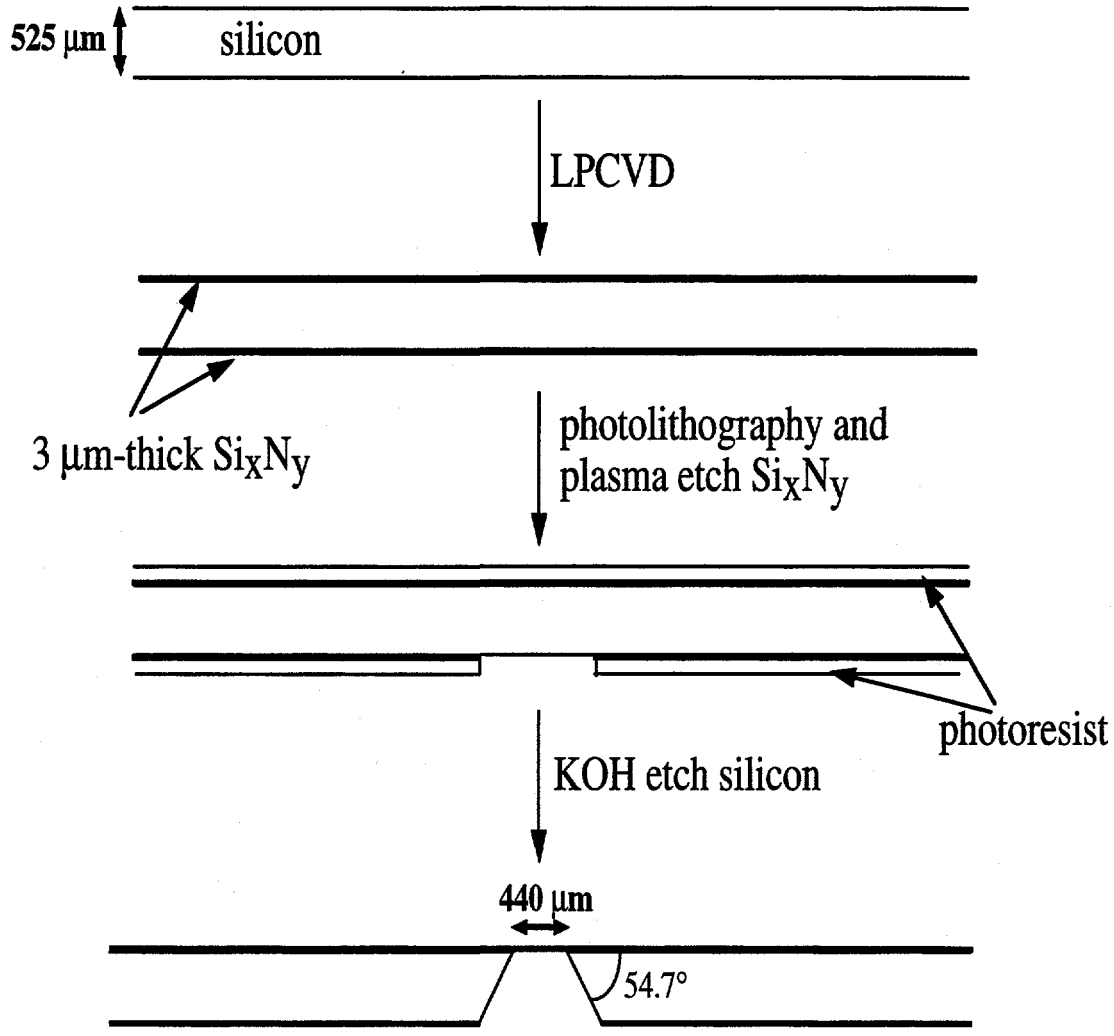

Figure 7.2: Micromachining process for fabricating silicon nitride windows.

backside of the wafer by photolithography and SF_6 plasma etching (Steps 2 and 3). In the last step, the wafer is placed in an 80°C KOH bath (1000 g KOH in 1500 ml of water) which anisotropically etches the exposed silicon at a rate of about 1 μm/min along the [100] direction. The remaining Si_xN_y serves as an etch stop. This leaves an unsupported square (440 μm x 440 μm) of thickness 3 μm. The 54.7° angle results from the anisotropic nature of the etch process. I cut an octagonal area of side length 5.5 mm with one membrane in the center to produce each window chip. Next, about 6 of these window chips are wax-mounted membrane-side-down onto a polishing block and lapped down to a final substrate thickness of 250 μm. This step insures that the window substrate will not touch the basepiece (see Section 7.3.3) on which the SQUID chip is mounted. Finally, I mount each window chip onto a silicon ring and quartz tube as described for the sapphire window.

7.2.3 Fabrication of Wires on Silicon Nitride Windows

We must know the SQUID-window distance in order to avoid crashing the window into the SQUID chip and to deduce the SQUID-sample distance z. One method we use is based on measuring the mutual inductances between the SQUID and two wires of known separation (see Section 8.1.2). This method requires the fabrication of two thin-film wires directly on the vacuum window. I patterned wires only on silicon nitride windows, as a different z-measurement method (see Section 8.1.1) was used for the sapphire window.

I made the wires after each silicon nitride chip was lapped down to its final thickness. A conventional liftoff process is used to fabricate the 5-μm-wide, 100-nm-thick aluminum wires, a layout of which is shown in Figure 7.3. Four wires, rather than two, are made for redundancy. After the window chip is attached to the silicon ring and quartz tube, the contact pads are extended over the chip edges by 45°-incidence silver (200-nm-thick) evaporations through shadow masks. Leads are then silver-pasted to the edge pads, with the requirement that neither the paste nor the leads extend above the plane of the window. This insures that a sample scanned over the window will not touch the bonds.

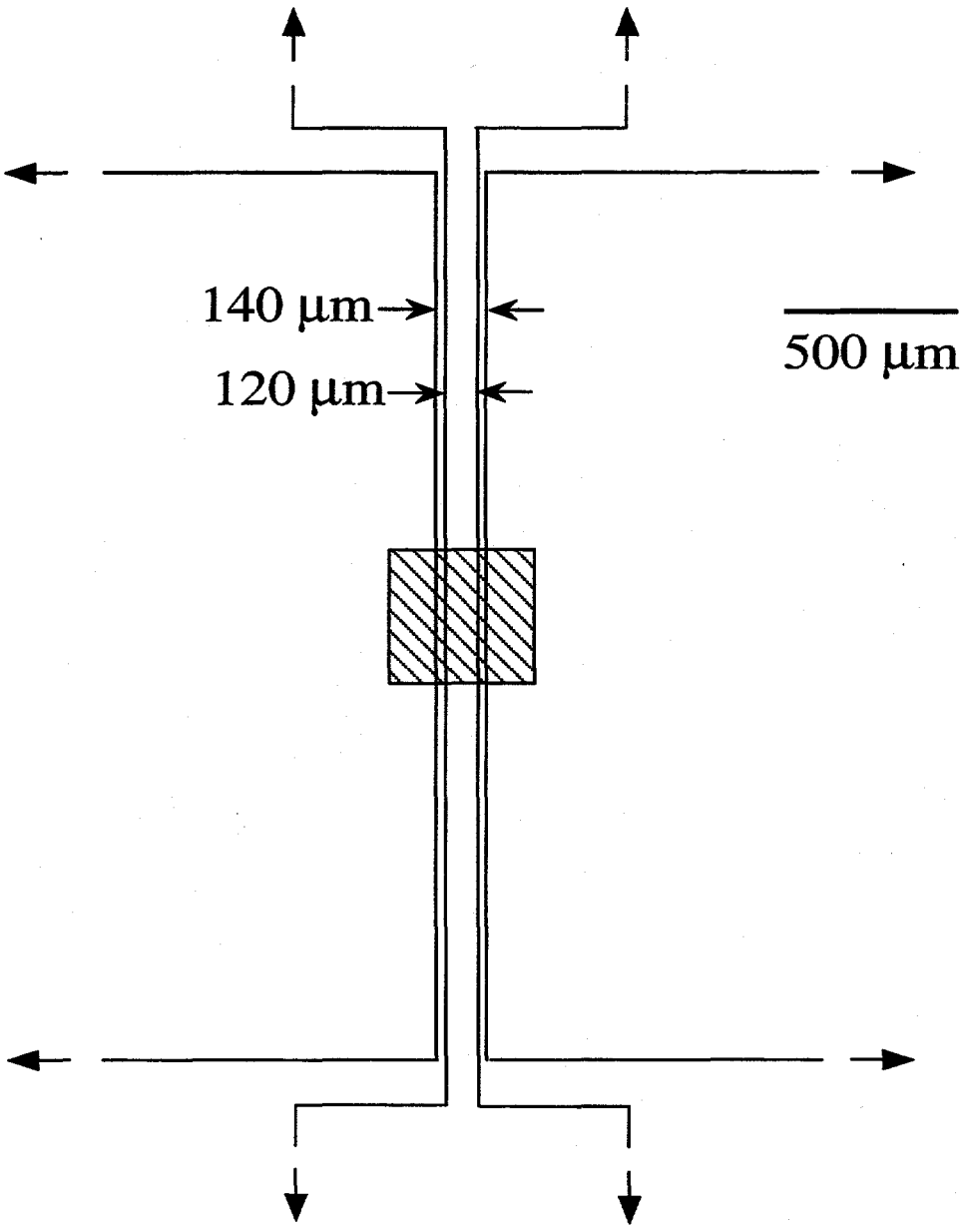

Figure 7.3: Layout of aluminum wires on silicon nitride window. Arrows point towards contact pads.

7.3 SQUIDs

7.3.1 SQUID Optimization

In our implementation of the microscope, we have chosen to use a bare SQUID as the sensor, rather than to use a superconducting flux transformer as have some other authors [37, 38]. For a given separation between the SQUID and the sample, one wishes to optimize the dimensions of the SQUID to achieve a compromise between spatial resolution and sensitivity to magnetic field. Others have considered this problem for circular sensors, and concluded that the best choice is to make the diameter comparable to z [38, 40]. Reducing the diameter much below z decreases the amount of captured flux, thereby reducing the signal amplitude from a given source, without appreciably improving the spatial resolution. Choosing a diameter much greater than z, on the other hand, markedly degrades the spatial resolution. In our microscope, the high-Tc SQUIDs we have used to date (Figure 7.5) are square washers rather than circular loops. In analogy to the optimization of circular sensors, we model the square washers as thin square loops of effective side length $s = A_{eff}^{1/2}$, where A_{eff} is the effective sensing area of the SQUID measured in a uniform magnetic field. We then design our system so that $s \approx z$.

For situations in which the efficiency of flux coupling is much more important than the spatial resolution, the optimization condition changes. For example, one can choose $s = (2.54)z$ in order to maximize the flux coupled into the SQUID loop from a magnetic dipole oriented perpendicularly to the SQUID plane and laterally positioned over the center (see Section 8.2). Another special situation occurs when the sample has linear dimensions of order ℓ such that $\ell \gg z_{min}$, where z_{min} is the distance between the SQUID and the closest surface of the sample. If one wants to maximize the net signal from the entire sample without spatially resolving features on a length scale less than ℓ, then one should make the SQUID loop comparable to ℓ rather than to z_{min}. To illustrate this principle, I have calculated the dependence of the coupled flux on the ratio s/ℓ for a cubic sample uniformly magnetized along the SQUID axis and centered directly over the SQUID loop (Figure 7.4); for the solid line, I have set $z_{min} = 0.1{*}\ell$. The total flux is equal to the volume integral of the magnetization, where each volume element is weighted by a geometrical factor. In this case, the maximum flux is achieved when $s \approx (1.5)\ell$.

In reality, z_{min} is not completely independent of s, due to the geometrical constraints imposed by the vacuum window. First, we know that $z_{min} = (t + b)_{min} + g_{min}$.

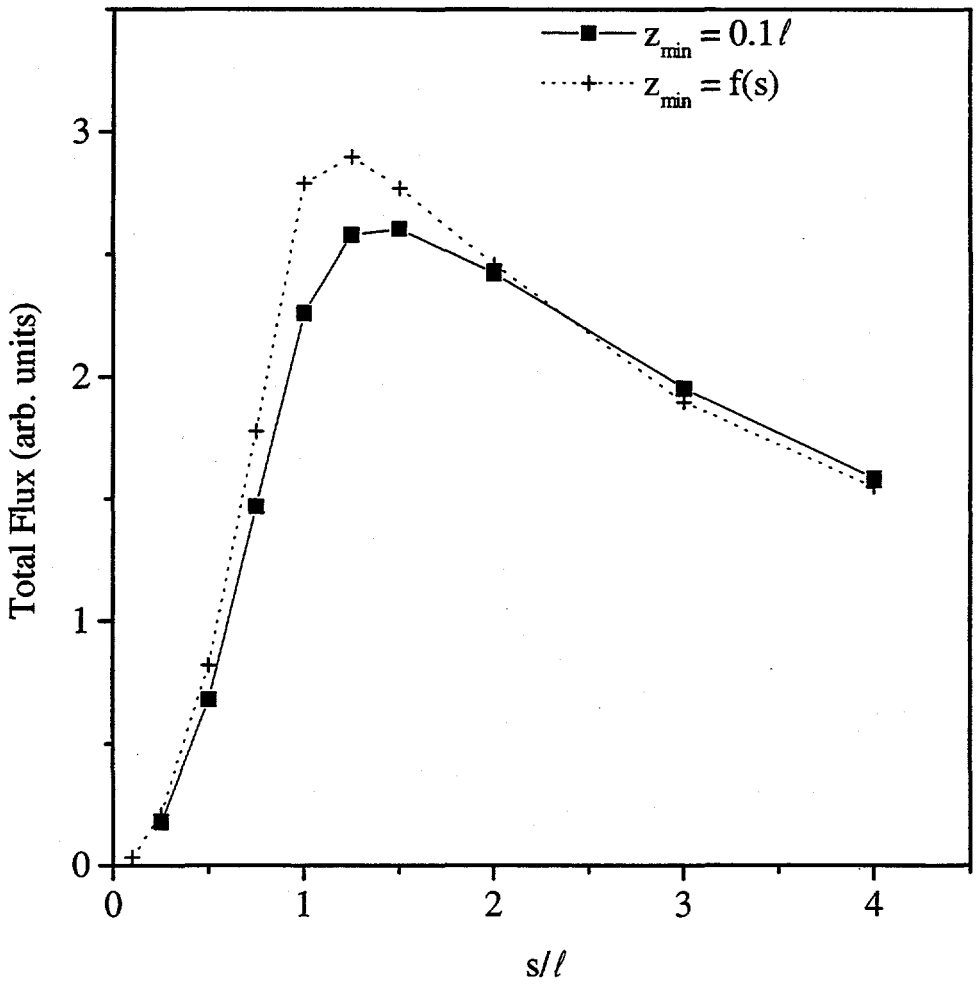

Figure 7.4: Calculation of coupled flux versus effective square loop size s for a uniformly magnetized cube of side length ℓ. Dotted line represents the calculated flux when z_{min} is set by s according to Equation 7.4.

However, for a circular window, $(t+b)_{min}$ depends on the window radius a, via Equation 7.2. For mathematical simplicity, we use the formula $b = 0.188P(1-\nu^2)a^4E/t^3$, which is strictly only true in the limit $b \ll t$. Using this relation, the sum $(t+b)$ is then easily minimized to yield:

$$(t+b)_{min}(a) = (\frac{4}{3^{3/4}})(\frac{0.188P(1-\nu^2)}{E})^{1/4}a. \tag{7.3}$$

(Note that when $(t+b) = (t+b)_{min}$, then $t = 3b$, in partial agreement with the assumption $b \ll t$.) In addition, we know that a is bounded below by the constraint $2a > \sqrt{2}s =$ the largest dimension of the SQUID (assuming a square loop), in order to facilitate the smallest possible vacuum gap. We therefore set $2a = \sqrt{2}s$ in order to achieve the minimum $(t+b)$ for a given loop size s. We also use that $g_{min} \approx \sqrt{2}\theta s$, where θ is the tilt of the SQUID chip relative to the window. Putting all these relations together, we obtain:

$$z_{min} = [(\frac{4}{3^{3/4}\sqrt{2}})(\frac{0.188P(1-\nu^2)}{E})^{1/4} + \sqrt{2}\theta]s \equiv f(s). \tag{7.4}$$

I can now calculate the flux as a function of s/ℓ with z_{min} given by Equation 7.4. The dotted line in Figure 7.4 shows the result for a sapphire window ($E = 345$ GPa and $\nu = 0.3$) under atmospheric pressure. In this particular case, the optimization condition ($s \approx (1.3)\ell$) is close to that obtained by simply setting $z_{min} = 0.1\ell$.

7.3.2 SQUID Layout and Fabrication

We have used two types of SQUIDs with substantially different washer designs, as shown in Figure 7.5. I heretofore will refer to these as the hole SQUID and the slit SQUID. Table 7.1 lists typical characteristics of each, including the junction parameters and maximum voltage modulation. The values of A_{eff} were measured in a uniform magnetic field; the corresponding values of s differ by a factor of about 3 although the inductances are comparable. A hole SQUID designed with the same value of s as the listed slit SQUID would have an impractically small voltage modulation ΔV due to its large inductance L. This upper practical limit on L results from the low intrinsic normal resistances of high-T_c bicrystal junctions [44]. Thus, the slit SQUID allows one to achieve a large value of s (or A_{eff}) without raising L beyond the practical limit.

The optimization condition demands that $s \approx z$. We achieved a different minimum value of z, z_{min}, for each vacuum window. For the sapphire window (thickness = 75 μm), we obtained $z_{min}(\text{sapphire}) \approx 140$ μm. $s(\text{slit SQUID}) = 114$ μm is comparable to

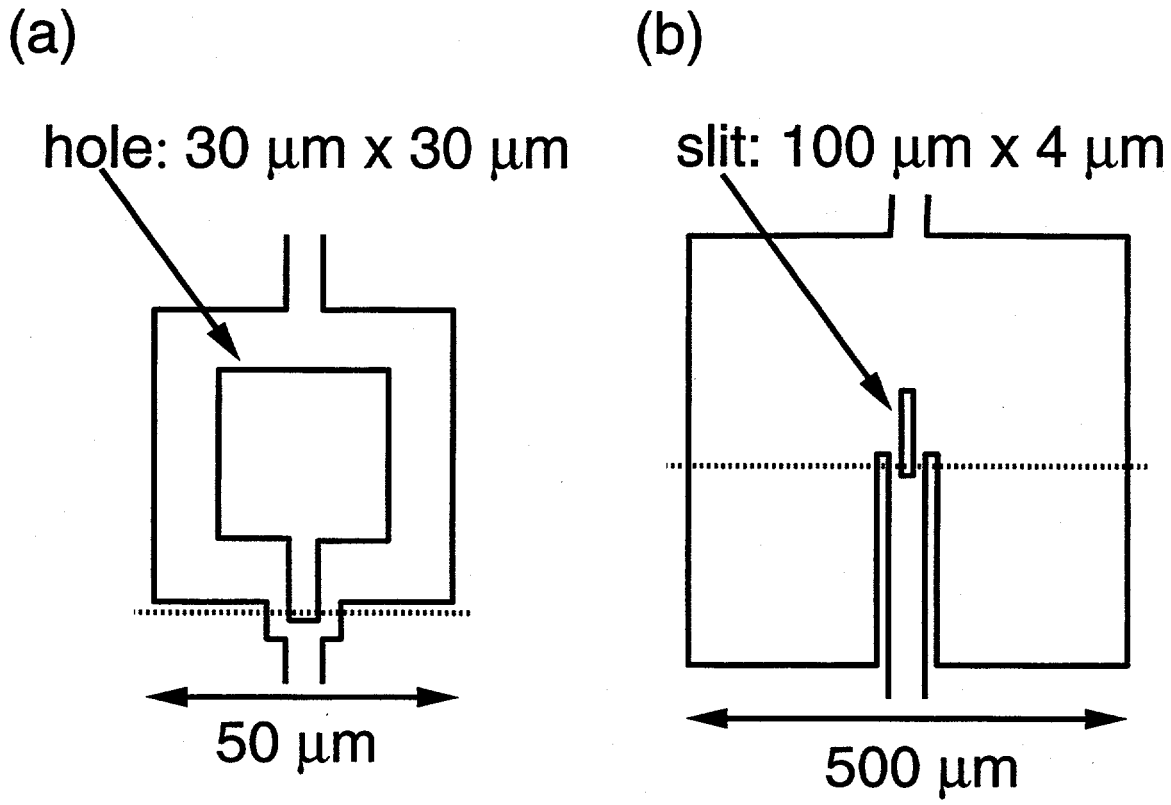

Figure 7.5: Configuration of (a) hole and (b) slit SQUIDs. Dashed line indicates bicrystal grain boundary.

SQUID	A_{eff} (mm^2)	s (μm)	L (pH)	R (Ω)	I_0 (μA)	ΔV (μV)
hole)	1.65×10^{-3}	41	57	4.0	11	11
slit	13.1×10^{-3}	114	40	1.8	80	15

Table 7.1: Representative SQUID parameters. A_{eff} is the effective sensing area, $s = \sqrt{A_{eff}}$, L is the SQUID inductance, R and I_0 are the resistance and critical current per junction, ΔV is the peak-to-peak voltage modulation.

z_{min}(sapphire), representing a reasonable level of optimization. However, for substantial variations of the magnetic signal over distances less than the outer dimension (500μm) of the slit SQUID, flux focusing by the superconducting washer may introduce some undesirable distortions into the image. Under these circumstances, we use the hole SQUID, which distorts the field less but has reduced sensitivity due to its smaller effective area. For the silicon nitride vacuum window (thickness = 3 μm), $z_{min}(Si_xN_y) \approx 15$ μm. For this case, we have fabricated and used smaller hole SQUIDs (not shown here) having s $\approx$ 20 μm, although we primarily used hole SQUIDs with s $\approx$ 40 μm for the work described here.

We fabricate the SQUIDs by laser-depositing a 160 nm-thick film of $YBa_2Cu_3O_{7-x}$ (YBCO) on a (100) $SrTiO_3$ bicrystal [44]. The film has a typical transition temperature of 90K and the bicrystal has a 24° misorientation angle, a thickness of 0.5 mm, and an area of 10 mm x 10 mm. The film is patterned with photolithography and Ar-ion milling to include two microbridges 1-2 μm wide across the grain boundary of the bicrystal to form the Josephson junctions of each SQUID (multiple SQUIDs are usually fabricated on the same substrate). Each substrate has one or more SQUIDs with the accompanying contact pads.

7.3.3 Preparing SQUID Chips

In order to prepare SQUIDs for the microscope, we must cut the SQUID substrate into smaller chips and fabricate easily accessible electrical contacts. As described in Section 7.2.1, decreasing the lateral dimensions of the chip allows for smaller values of z to be achieved. As a first try, I used a diamond grit dicing saw to cut a square chip of area 3 mm x 3 mm holding five SQUIDs (one of which is the hole SQUID listed in Table 7.1). This did not seem to damage the devices as their junction parameters were nearly the same as before cutting. This chip is small enough to use with the 5-mm-diameter sapphire window described in Section 7.2.2. We made electrical contacts to the SQUIDs by multiple silver evaporations (each 200-nm-thick) at 45° incidence through mylar shadow masks. This method extends the contact pads over the edges of the substrate and obviates the need for bonds on the top of the substrate, which would otherwise limit the minimum spacing between the SQUID and the window. After gluing the chip to the end of the cold finger (see Section 7.4.2), we then used silver paste bonds or indium pellets to attach leads to the pads on the chip edges. A similar procedure was carried out for chips containing slit SQUIDs.

The net contact resistance to each SQUID is typically on the order of 1 Ω.

In order to prepare SQUID chips for the silicon nitride vacuum window, I had to develop a process for cutting the substrate down to areas of less than 400 μm on a side. Initial attempts to cut the substrate using a dicing saw seemed to damage the Josephson junctions, presumably due to stress imposed on the grain boundary by the blade. I therefore implemented a gentler dicing procedure (see Figure 7.6). The idea for this process was kindly suggested to me by Scott Sachtjen of Conductus, Inc. First, an outline of the final chip area is scribed around each SQUID to a depth of about 150 μm using a dicing saw. In order to minimize stress placed on the chip, the scribing is carried out in three succesive cuts of increasing depth (about 50 μm increments) and performed with the lowest possible translational cutting speed (0.3 mm/sec). Next, the partially cut substrate is flipped over and polished down from the backside, thereby releasing the final chips (150-μm-thick) from the original substrate. SQUIDs exposed to this process seemed to maintain the critical currents and junction resistances as measured before cutting. I managed to cut SQUID chips 250 μm x 300 μm in area, smaller than the silicon nitride window, as required. In order to evaporate the leads, each chip is first glued to the top of a larger silicon basepiece (see Figure 7.7) with cyanoacrylate adhesive. Mylar evaporation shadowmasks are then fashioned so that 200-nm-thick silver strips, evaporated at 45°-incidence, link the SQUID pads to the lower edges of the basepiece. The four potentially weak links where the silver films must cross gaps are reinforced with small drops of silver paste to ensure electrical continuity. Leads are attached to the lower edge pads with silver paste. The net contact resistance to the SQUID is usually less than 2 Ω.

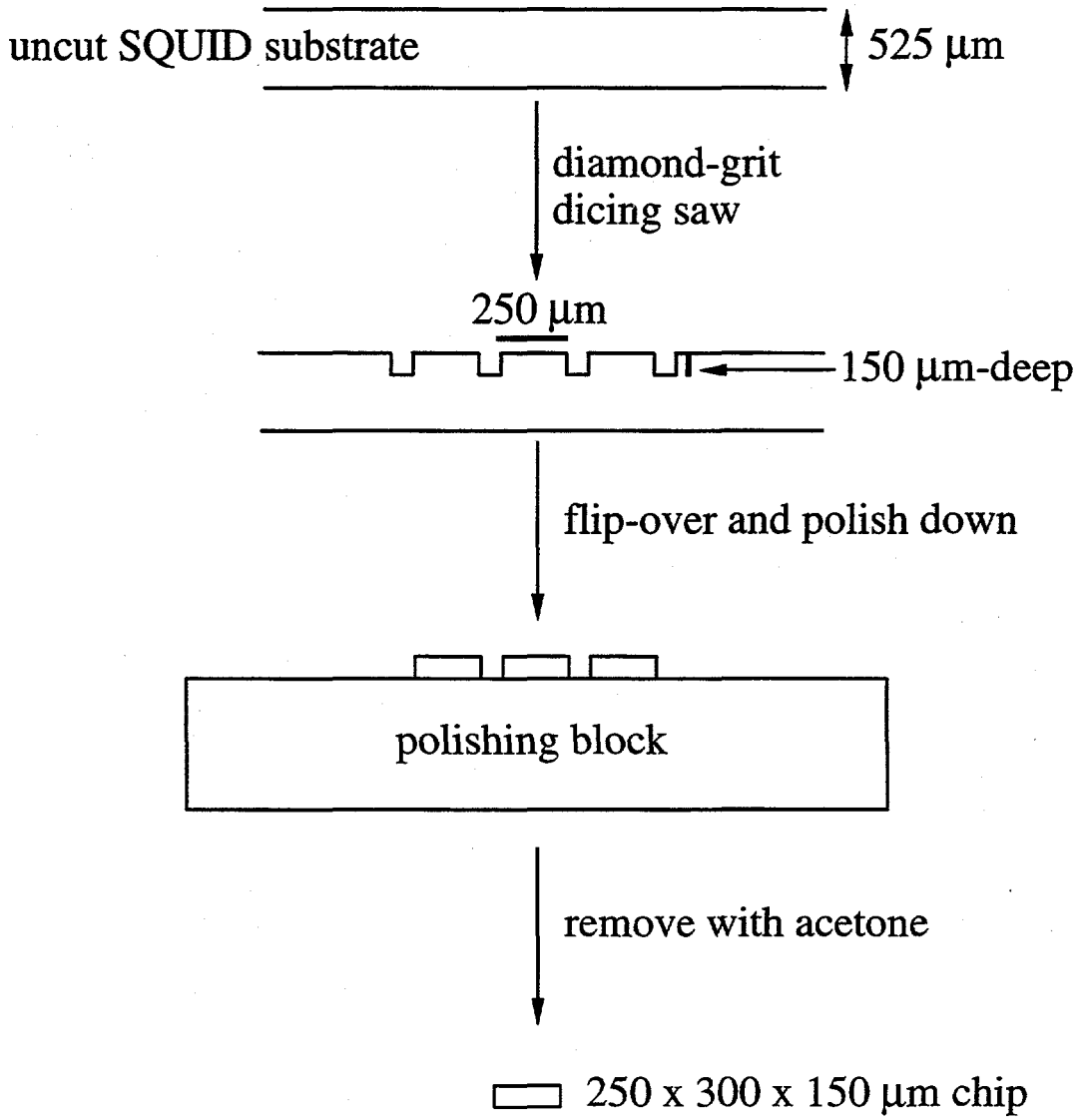

Figure 7.6: Dicing process for SQUID chips to be used with silicon nitride vacuum windows.

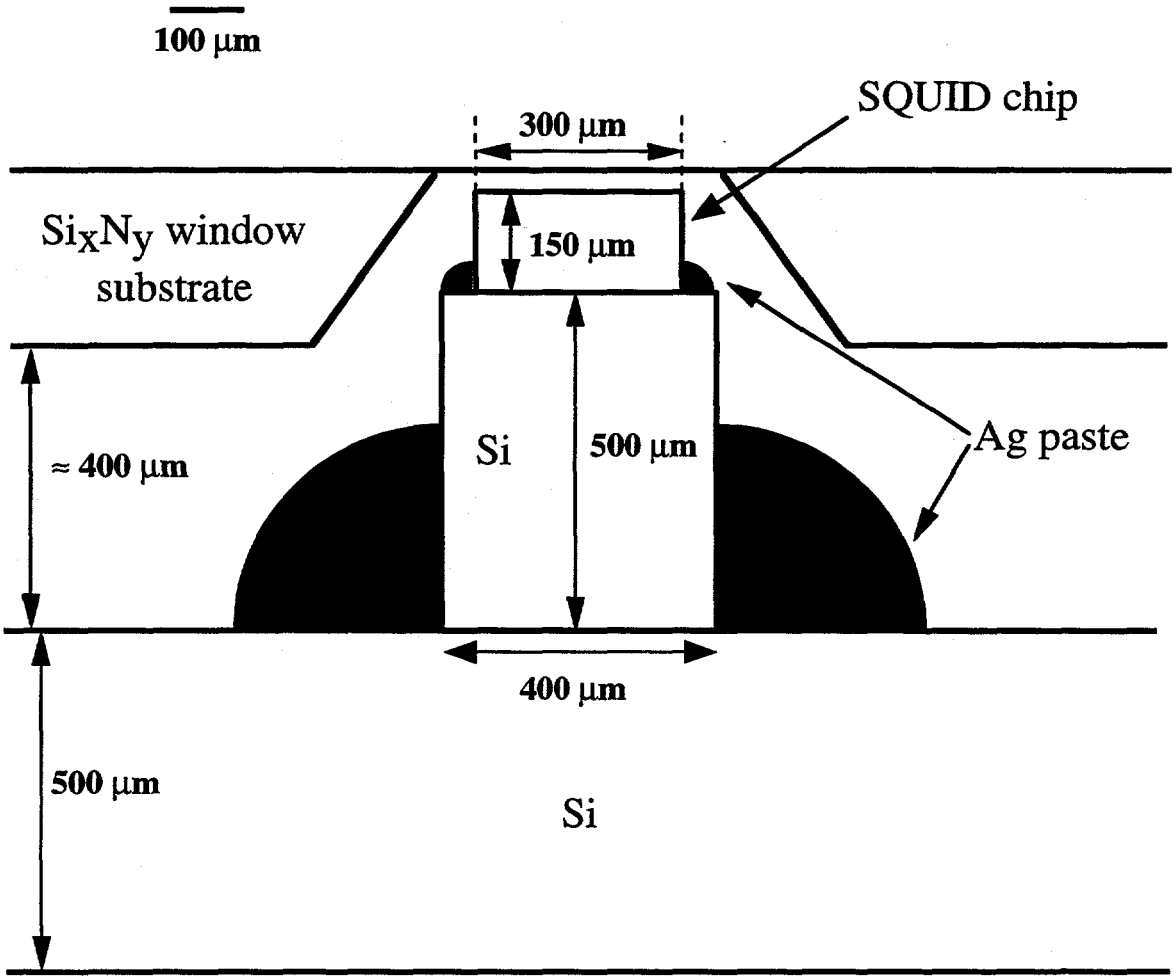

Figure 7.7: Silicon basepiece with a SQUID chip mounted.

7.4 Dewar

7.4.1 Requirements

Our goal in designing the dewar was to achieve a reasonable hold-time for the liquid nitrogen ($\geq$ 1 day) while maintaining moderate overall dimensions ($\approx$0.25 m). A major design criterion is that the dewar should produce levels of magnetic field noise arising from magnetic impurities or from Nyquist noise currents in electrically conducting components that are below the intrinsic noise level of the SQUID. We found that G-10 fiberglass and metals such as copper, brass and aluminum contain sufficiently low levels of magnetic impurities that their magnetic field noise is not an evident problem in our instrument. However, the issue of Nyquist noise currents is potentially more serious [45, 46, 1]. For example, it is more straightforward to construct the liquid nitrogen can from metal than from fiberglass, but one must ensure that the volume of metal involved and its distance from the SQUID are such that the ensuing magnetic field noise is negligible. To design the metal components, we used a formula for the spectral density of magnetic field noise, $S_B(f)$, due to Clem [1]

$$S_B^{1/2}(f < f_c) = (4k_B T \mu_0^2 g/\rho_n)^{1/2}, \tag{7.5}$$

where the units are T $\mathrm{Hz}^{-1/2}$. Here, k_B is Boltzmann's constant, T is the temperature, μ_0 is the permeability of free space, ρ_n is the electrical resistivity and g is a geometrical factor (with units of an inverse length) that depends on the dimensions of the component and its distance z_0 from the SQUID. The spectral density of the noise is white for frequencies f below a crossover frequency $f_c = \rho_n/4\mu_0 t z_0$, and falls off as $1/f^2$ for frequencies above f_c [46, 1]; here, t is the thickness of the metal object. Thus, $S_B^{1/2}(f < f_c)$ sets an upper bound on the spectral density at all frequencies. The geometrical factor g is generally a somewhat complicated function of the relevant parameters, and is given by Clem for various simple cases. Table 7.2 lists the estimated values of g, f_c and $S_B^{1/2}(f < f_c)$ for five components that we initially believed to be potential sources of noise. In some cases, we have estimated g by superimposing the relevant expressions from Clem's paper. As a result of our design criteria, the estimated noise levels are negligible, summing to about 70 $\mathrm{fT}/\sqrt{\mathrm{Hz}}$. This value is a factor of about 30 below the intrinsic noise of the most sensitive SQUID we have used to date.

	T (K)	$\rho_n(T)$ (Ω m)	g (m^{-1})	f_c (Hz)	$S_B^{1/2}(f < f_c)$ (fT /$\sqrt{\text{Hz}}$)
Brass bellows	293	7×10^{-8}	2.5×10^{-4}	10^4	10
3 brass arms	293	7×10^{-8}	8.9×10^{-3}	100	60
Copper clamp	77	2×10^{-9}	2.4×10^{-5}	0.3	10
Brass can	77	4×10^{-8}	5.4×10^{-4}	7	10
Magnetic enclosure	293	6×10^{-7}	9.4×10^{-4}	800	10
				Total RMS :	70

Table 7.2: Estimates of Nyquist noise $S_B^{1/2}(f < f_c)$ from selected components with resistivity ρ_n at temperature T; g is a geometric factor, and f_c a crossover frequency estimated from [1].

7.4.2 Description

The configuration of the dewar is shown in Figure 7.8. The vacuum enclosure P is made of G-10 fiberglass with top and bottom plates sealed with viton o-rings. The top plate can easily be removed to service the liquid nitrogen can and the cold finger attached to it. Liquid nitrogen fill tubes N, electrical feedthroughs R, and a pump-out flange Q are sealed into the fiberglass with epoxy. The height is 0.35 m and the diameter 0.25 m. The brass can J holds 1 liter of liquid nitrogen, and consists of a cylinder with a 3.2 mm-wall thickness hard soldered to a 12.7 mm-thick upper disk and a 6.4 mm-thick lower disk. An OHFC copper rod K, 12.7 mm in diameter, is hard soldered into the can to provide a high conductivity thermal link to the top. If we had made the can from copper, the additional thermal link would not have been necessary, and the magnetic field noise would have been roughly a factor of 3 higher. Since this noise level is still negligible, it would have been somewhat simpler to make the can from copper, and to omit the rod. We note that the rms magnetic noise produced by the can at the SQUID increases rapidly as the separation is decreased. However, had the separation been halved, the estimated noise would have quadrupled to about 40 $fT/\sqrt{Hz}$, a value that is still negligible.

A charcoal panel L for adsorbing residual gas such as Ar, N_2 and O_2 is attached to the bottom of the nitrogen can, as are (M) a 30 Ω cartridge heater that enables us to warm-up the can in about 1.5 hours, and an iron-constantin thermocouple. The nitrogen can is supported from the top-plate of the vacuum enclosure by three fiberglass rods O, and two stainless steel nitrogen fill tubes N are soldered into the wall of the can. The can, fill tubes and support rods are each wrapped with 15 layers of double-sided aluminized mylar (not shown) for radiative heat shielding.

The cold finger H consists of two sapphire rods, the lower one 61 mm long and 6.35 mm in diameter and the upper 51 mm long and 4 mm in diameter, joined end-to-end with a copper clamp. The lower end of the finger is clamped to a copper base I that is screwed to the top of the liquid nitrogen can J. An intervening layer of 125 μm-thick silver foil in each joint ensures high thermal conductivity. A platinum thermometer, carbon resistor heater and two ferrite-core transformers (allowing two SQUIDs to be operated in the same run) are bonded to the side of the finger. The entire cold finger, other than the SQUID chip, is wrapped with 10 layers of double-sided aluminized mylar.

The SQUID chip a is attached to the top of the upper sapphire rod with GE

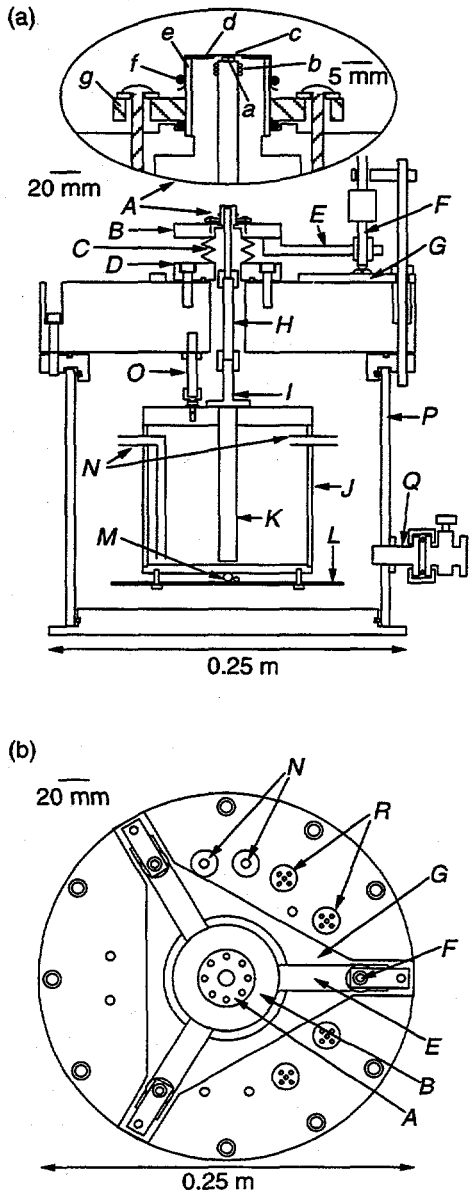

Figure 7.8: Sectional side view of microscope (without X-Y scanner). *A* Vacuum window assembly, *B* upper fiberglass disk, *C* brass bellows, *D* lower fiberglass disk, *E* brass arm, *F* positioning screw, *G* phenolic baseplase, *H* sapphire cold-finger, *I* copper base, *J* liquid nitrogen can, *K* OFHC copper rod, *L* charcoal panel, *M* thermocouple and cartridge heater, *N* nitrogen fill tubes (connected to top of enclosure), *O* fiberglass support rod, *P* vacuum enclosure, *Q* pump-out valve. Inset: *a* SQUID chip, *b* flux modulation coil, *c* vacuum window, *d* quartz ring, *e* quartz tube, *f* rubber band, *g* acrylic ring. (For clarity, electrical wires and aluminized-mylar insulation are not shown). (b) Top view of microscope (without X-Y scanner). Labeling as in (a); *R* electrical feedthroughs.

varnish, and a modulation/feedback coil b (25 turns, diameter 4.5 mm and self-inductance 300 nH) is wrapped around the rod immediately below. The mutual inductance between the coil and the SQUIDs is about 4 pH and 40 pH for the hole and slit devices respectively. As explained in Section 7.2.2, the quartz tube e supporting the window is clamped into a socket on a fiberglass disk B; an o-ring provides the vacuum seal. A brass bellows connects this disk to a lower one D sealed with another o-ring against the top of the vacuum enclosure. The upper disk is supported by three brass arms E riding on aluminum positioning screws F (3.15 turns/mm) or, alternatively, commercial micrometers (Newport, Corp.) that enable one to adjust the height and tilt of the window. To ensure lateral stability the screws are mated to a kinetic mount on a phenolic baseplate G which is also screwed to the top-plate. The lateral position of this baseplate can be adjusted to center the window over the SQUID. If desired, flexible delrin couplings can be used to link the positioning screws to fiberglass rods that can be turned from outside the magnetic shield.

In order to minimize the SQUID-window distance, it is critical that the top surface of the SQUID chip be as parallel as possible to the plane of the vacuum window. Since the tilt of the flat end of the cold finger largely determines the extent of the SQUID-window relative tilt, we must level the cold finger end as parallel as possible to the window plane. This is accomplished in the following way. The SQUID and the quartz tube holding the vacuum window are removed from the microscope. A clean glass slide of length L is placed on the flat end of the cold finger (Figure 7.9). The plane of the slide is parallel with the cold finger end to within milliradians or less (this can be confirmed by seeing the Newton rings between the two surfaces). The tilt of the slide relative to the top surface of the upper fiberglass disk B is then determined by measuring the vertical distances (h_1 and h_2) between the ends of the slide and the disk, as shown in Figure 7.9. The same measurement is repeated with the slide rotated at another angle. Two tilt angles are thereby determined, and we adjust the positioning screws to reduce the net tilt. Using this method, we can level the fiberglass disk and the cold finger end to within 1°, which is much greater than any residual misalignment between the plane of the disk and the mounted vacuum window. Therefore, we can make the window and the end of the cold finger parallel to within about 1°.

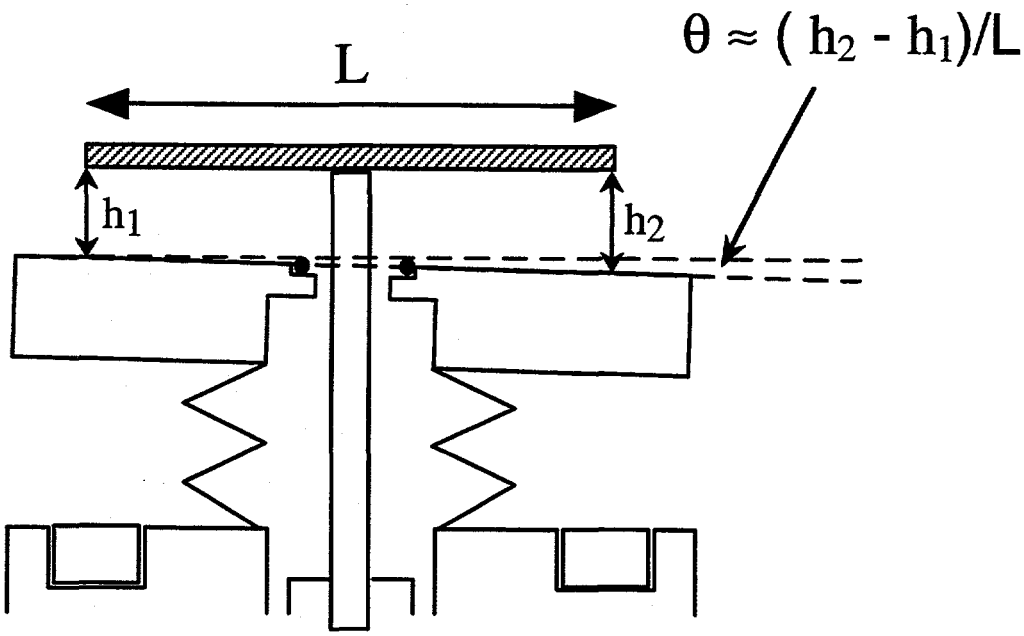

Figure 7.9: Method for measuring the tilt of the cold finger relative to the fiberglass disk supporting the vacuum window assembly.

7.5 Sample Scanner

The essential requirements for the sample scanner are that it have positioning errors much smaller than z, in order not to degrade the spatial resolution, and that it be made of non-magnetic and non-metallic materials to minimize magnetic noise. It is particularly important that moving components be non-magnetic. Thus, we constructed the scanner from phenolic, delrin and G-10 fiberglass, joined together with epoxy and nylon screws. These materials are non-metallic, only very weakly magnetic, and have sufficient structural integrity to make positioning errors unimportant.

The components of the scanner, shown in Figure 7.10, are of phenolic unless labeled otherwise. The translation stage I', which is attached to tubes A' that slide on closely-fitting rods B', is pulled against positioning screws C' (2.31 mm/turn) by rubber bands F'. Vertical fiberglass rods J' extending through the bottom of the shielded enclosure are coupled to the positioning screws by 1:1 beveled delrin gears E' and coupling sleeves D'. Computer-controlled stepping motors outside the magnetic shield turn the rods. The minimum step size is 5.77 μm and the backlash upon reversal of the scanning direction is 20 μm. Backlash can be eliminated in the data acquisition software, leaving a residual positioning error of about $\pm 2\,\mu$m due primarily to wobble in the positioning screws. In any case, the positioning error is much less than the lowest value of z (15 μm) achieved so far. The maximum scan range is ± 12.5 mm and the maximum scan speed is 7.2 mm/sec.

As shown in the inset of Figure 7.10, the sample is glued or taped beneath a 12.5 μm-thick mylar sheet stretched over a circular fiberglass frame H'. The frame is attached to the translation stage I' with nylon screws, thereby pressing the sample against the vacuum window, which is robust enough to withstand the contact force. This force can be adjusted by means of shims between the frame and the translation stage. If necessary, an additional 2.5 μm mylar sheet can be positioned under the sample to protect it during scanning. Demounting the frame is straightforward, but requires one to remove the top of the magnetic shield. If we wish to change samples without opening the shield, we use an alternative frame (not shown) that accepts samples inserted through a hole in the shield.

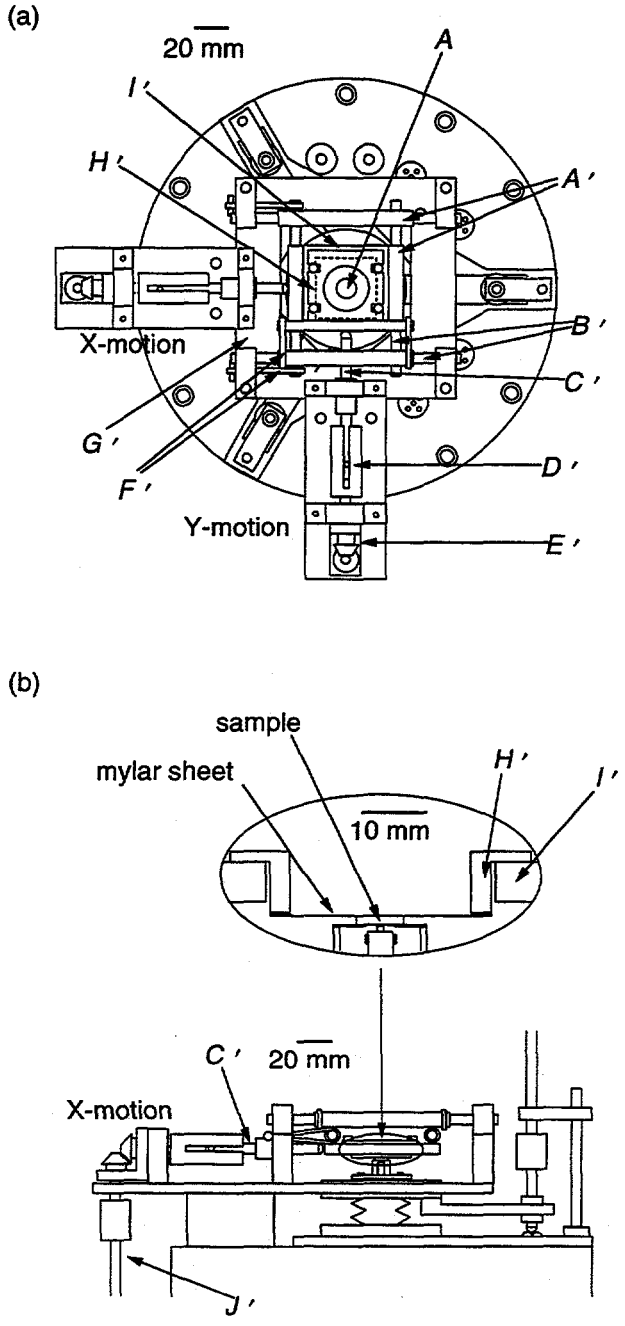

Figure 7.10: Sample scanner mounted on dewar top. (a) Top view: A vacuum window, A' phenolic tubes, B' phenolic rods, C' positioning screw, D' phenolic coupling piece, E' Delrin gearbox, F' rubber bands, G' scanner baseplate, H' fiberglass frame, I' translation stage (dotted rectangle indicates a hole obscured by the fiberglass frame). (b) Side view: J' fiberglass rod, other lettering as in (a); Y-positioning mechanism omitted for clarity. Inset: cut-away side-view with a mounted sample.

7.6 Magnetically Shielded Enclosure

To exclude stray 60 Hz magnetic fields, which can be as high as 10 nT/$\sqrt{\text{Hz}}$ in our laboratory, we enclosed the microscope in a mu-metal shield. The shield also provides a very low ambient static field, which precludes the generation of excess $1/f$ flux noise in the SQUID by the thermally activated hopping of vortices trapped during cooldown [3]. Finally, the shield provides a high degree of isolation against radiofrequency (rf) interference arising from radio, television, computers and other electronic instruments.

The enclosure consists of three layers of mu-metal 1 mm thick enclosing a cylindrical volume 0.45 m high and 0.4 m in diameter (Amuneal Manufacturing Corp.). Prior to heat treatment of the mu-metal, holes were punched in the bottom and removable lid to allow for sample access, electrical and mechanical feedthroughs and a fiber optic light pipe. The light pipe provides illumination of the sample to facilitate its mounting and positioning with the lid of the magnetic enclosure in place. The holes are sufficiently small that magnetic field leakage is negligible. The manufacturer's guaranteed minimum shielding factors are 13,000 and 52,000 at 0 Hz and 60 Hz, respectively. The earth's static field is thus reduced to about 5 nT and the maximum 60 Hz noise to about 200 fT/$\sqrt{\text{Hz}}$, well below the intrinsic noise of the SQUIDs. The rf shielding is sufficient to eliminate any observable effects on the characteristics of the SQUIDs. Finally, the relatively high electrical resistivity of mu-metal ensures a negligible Nyquist noise contribution (Table 7.2).

7.7 SQUID Electronics and Data Acquisition

The SQUIDs were operated in a flux-locked loop (Figure 7.11) with a flux modulation frequency of 100 kHz and with optional bias-current reversal at 3.125 kHz to reduce the $1/f$ noise due to critical current fluctuations [47]. The bandwidth is 1.5 kHz and 36 kHz, respectively, with and without bias current reversal. The SQUID is connected via one of the two liquid nitrogen-cooled transformers (Section 7.4.2) with voltage gains of 23 and 28, respectively, to a low-noise preamplifier. The flux modulation and feedback signal are coupled to a coil below the SQUID chip (Figure 7.8(a) inset). Typically, we adjust the gain of the output stage of the loop to give a dynamic range of $\pm$ 100 Φ_0, where $\Phi_0 = h/2e$ is the flux quantum. The magnetic flux noise $S_\Phi^{1/2}(f)$ and magnetic field noise $S_B^{1/2}(f) = S_\Phi^{1/2}(f)/A_{eff}$ achieved with current bias reversal for two representative SQUIDs are listed

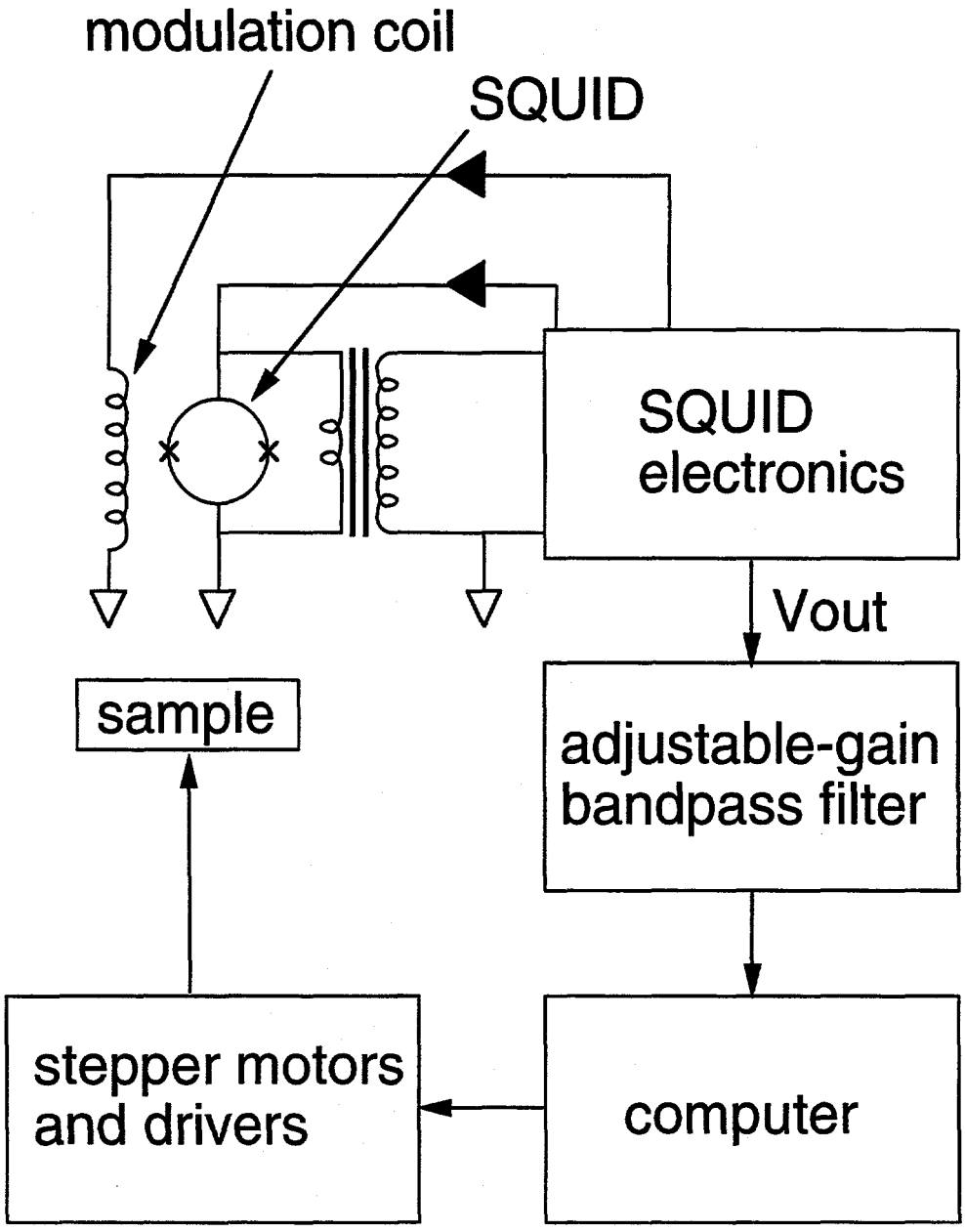

Figure 7.11: Schematic layout of electronics and data acquisition system.

in Table 8.1 on p. 86. In both cases, $1/f$ noise became dominant at frequencies below a few Hz. At higher frequencies, the flux noise of about 20 $\mu\Phi_0/\sqrt{Hz}$ leads to a dynamic range of about $\pm 100\Phi_0/20\mu\Phi_0/\sqrt{Hz} = \pm 5 \times 10^6\sqrt{Hz}$. The output voltage V_{out} of the SQUID electronics is low-pass filtered at a frequency, typically 30-100 Hz, somewhat higher than the maximum signal frequency produced by scanning. The signal voltage is coupled to a 12-bit A-to-D interface board and stored in a Macintosh II computer. The maximum data acquisition rate of 127 samples/sec is set by the A-to-D board. The computer also supplies pulses to the stepper motors that drive the translation stage.

Chapter 8

Performance and Discussion

8.1 SQUID-Sample Separation

8.1.1 Sapphire Window

When using the sapphire window, we estimate the SQUID-sample distance by measuring the field pattern produced by a current passing through a wire. I deposited a long 5 μm-wide, 90 nm-thick aluminum wire on a mylar sheet for the measurement. The wire, carrying a current of 2 mA, is scanned across the window, and the variation in magnetic field is measured. A measurement with the smallest value of z achieved with the sapphire window is illustrated in Figure 8.1(a), where we used a hole SQUID ($s = 40\,\mu$m) on a 3 mm x 3 mm substrate. We have fitted the data using the single parameter $z = 139 \pm 5\,\mu$m. Assuming that the wire lies in a plane and given the bow (9 μm) of the window, we infer that the gap between the window and the SQUID is about 55 μm. In actuality, the vacuum gap may be as large as $55 + 9 = 64$ μm because the wire is pressed against the window with a small weight, thereby reducing the contribution of the bow to the SQUID-wire vertical separation. We find that we can consistently achieve a gap between 55 and 65 μm. The minimum gap is consistent with a net SQUID-window relative tilt of the order of 1°; this is comparable to the accuracy with which the cold finger end is leveled with the vacuum window (see Section 7.4.2). The SQUID-sample separation of about 140 μm is a factor of 6 smaller than the lowest value quoted for a low-Tc SQUID microscope [38], but substantially higher than the value of 40 μm achieved by Black and co-workers [41] with their high-Tc microscope using a 25 μm-thick, 1 mm-diameter sapphire window.

(a)

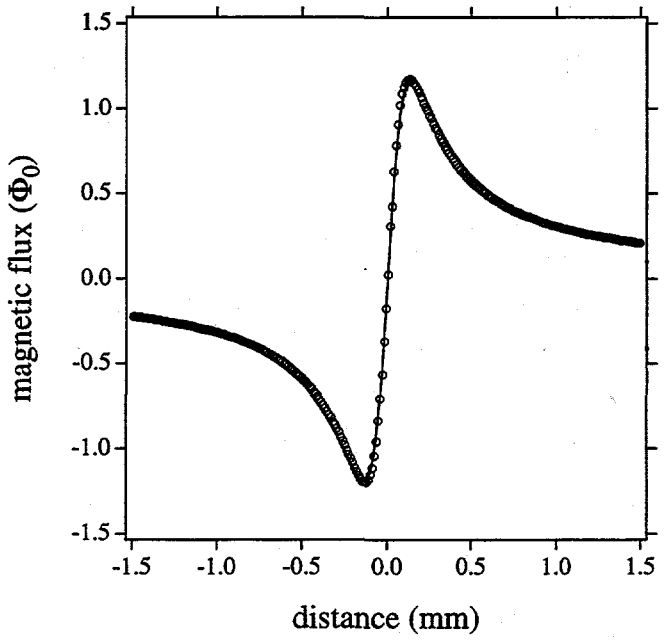

(b)

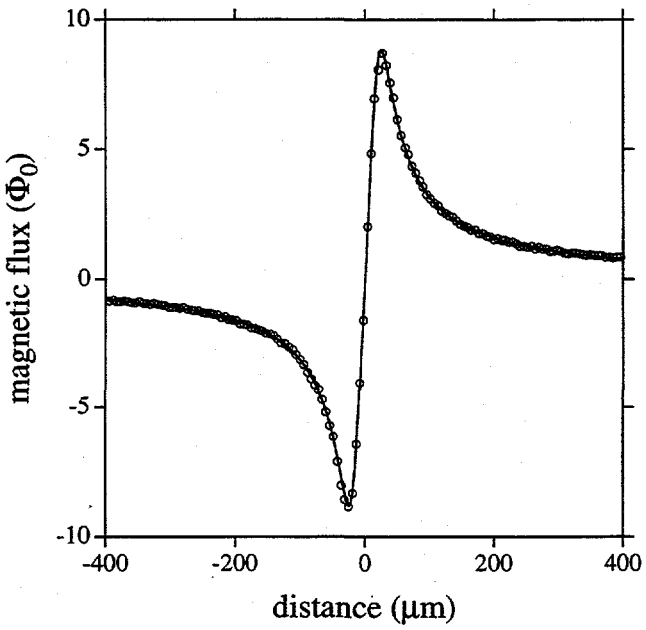

Figure 8.1: Magnetic field produced by wire scanned over (a) sapphire window and (b) silicon nitride window. Circles are data, and the solid lines are theoretical fits.

8.1.2 Silicon Nitride Window

We measure the SQUID-sample distance in two ways when using the silicon nitride window. The first method is the same as that used for the sapphire window. Figure 8.1(b) shows the field pattern acquired with a hole SQUID ($s = 40\ \mu$m) at the lowest value of z achieved with the silicon nitride window. The fitted value is $z = 15 \pm 2\ \mu$m. To our knowledge, this is the smallest SQUID-sample separation achieved to date for a warm sample SQUID microscope. Furthermore, since two layers of 2.5 μm-thick mylar separate the wire from the window, the actual distance from the SQUID to the outside of the window is only 10 μm. If we subtract the window thickness and bow from this value, then we deduce that the vacuum gap is only 5 μm.

The second way to deduce z is to measure the mutual inductance between the SQUID and each of two of the wires fabricated on the window (see Figure 7.3 on page 59). We define the separation between the plane containing the wires and the SQUID as z_{wires}, so that $z = z_{wires} + b$, where b is the window bow (despite the window curvature resulting from the bow, it is still a good approximation to assume that the wires lie in a plane tangent to the center of the window). The separation between the wires is defined as D. We typically use either the inner or the outer pair ($D = 100$ and 140μm, respectively). An oscillating current (typically having an amplitude of 400 μA and a frequency of 100 Hz) is sent through wire 1, and the flux amplitude is deduced by measuring the SQUID signal with a lock-in amplifier. The mutual inductance is equal to the flux amplitude divided by the current amplitude. This is repeated with wire 2, giving us the two mutual inductances, M_1 and M_2. There are two geometrical unknowns: the vertical separation z_{wires}, and the distance x, which is the lateral displacement of the SQUID center relative to wire 1 (x is positive in the direction pointing from wire 1 to wire 2; so wire 2 is at position $x = +\ D$). We can therefore use the two known quantities, M_1 and M_2, to solve for the unknown distances, z_{wires} and x. The absolute errors in z_{wires} and x are determined largely by the uncertainty in the equivalent loop size s. The experimental uncertainty in measuring M_1 and M_2 due to the intrinsic SQUID noise is negligible for sufficiently large current amplitudes (several hundred μA). The *absolute* error in z_{wires} is important here since we want to avoid touching the SQUID against the window. For fixed x, we have the following relation between z_{wires} and s:

$$z_{wires} = \sqrt{\frac{(x + s/2)^2 - e^{(4\pi M_1/\mu_0 s)}(x - s/2)^2}{e^{(4\pi M_1/\mu_0 s)} - 1}}. \tag{8.1}$$

The error in z_{wires} can be calculated from $\Delta z_{wires} = (\frac{\partial z_{wires}}{\partial s} |_{x=x_0})\Delta s$. For example, for D = 100 μm, $z_{wires} \approx 20\,\mu$m, $x = x_0 = 50\ \mu$m, $s = 40 \pm 1\mu$m($\pm$2.5 %), the error in z_{wires} is $\Delta z_{wires} \approx \pm 3\mu m$ ($\pm$15%).

The main advantage of the mutual inductance technique is the ability to monitor z continously. This is particularly useful whenever we lower the window towards the SQUID. For instance, in the magnetotactic bacteria measurements of the type described in Section 9.2, we were able to achieve vacuum gaps as small as 5 - 10 μm without bringing the window and the SQUID chip into direct contact. The ability to monitor z continuously over long times also greatly helps in identifying sources of drift in z (see Section 8.1.3). Furthermore, we can in principle measure the separation while scanning a sample. The only requirements are that the sample's magnetic permeability at the monitor frequency (100 Hz to several kHz) is sufficiently low and that the frequency range encompassed by the sample signal excludes the monitor frequency. One can also envision incorporating the technique into an active feedback mechanism that maintains a given z_{wires} at all times. In such an application, each wire would carry a current of a different frequency, and two lock-in amplifiers would be used to measure z_{wires} and x on a sub-second timescale. Most likely, active feedback will become mandatory in the next generation of instruments designed to achieve separations on the order of several micrometers.

8.1.3 Sources of Drift and Hysteresis in z

Using the mutual inductance technique to monitor z_{wires}, we found several sources of drift and hysteresis in the SQUID-window separation. First, hysteresis in the positioning screws (F in Figure 7.8 on page 72) appeared intermittently when cycling the screws between two positions. We suspected that wear between the tip of each screw and its respective kinetic mount contact point was responsible. These interfaces were originally composed of stainess steel rubbing against stainless steel. In order to minimize the effects of wear, we rebuilt the kinetic mount out of highly wear-resistant materials including sapphire, hardened-steel and chrome-plated steel. In addition, we replaced the original positioning screws with commercial micrometers having hardened-steel ends. These changes seemed to eliminate this source of hysteresis.

Second, we noticed both drift and hysteresis in z_{wires} associated with filling the nitrogen can. We observed that z_{wires} seemed to decrease $\approx$ 10 μm over a period of $\approx$ 2

hours after a nitrogen filling and then increase again, eventually settling at a value a few micrometers either larger or smaller than its value before filling. We initially thought that this might be due to cooling and subsequent warming of the dewar support rods (O in Figure 7.8 on page 72). However, measurements of the typical temperature changes of a rod during and after filling nitrogen ruled out this possibility. I then performed a measurement of z_{wires} while gently flowing liquid nitrogen through the can for 1.3 hours. Over this period plus 0.5 hours after the flow was stopped, I found that z_{wires} steadily decreased a total of $40\,\mu$m. Subsequently, the rate of decrease slowed until the separation began increasing. This strongly implied that the cooling of the fill tubes, due to nitrogen flowing through them, was somehow related to the drift in the separation. My hypothesis about the cause of the drift is as follows. When nitrogen is flowed through the nitrogen can, the fill tubes cool and contract, thereby exterting a large net upward force on the can. This thermal stress compresses the fiberglass rods supporting the can and slowly raises the height of the can, resulting in a decrease in z_{wires}. The rate of this compression depends on the magnitude of the stress and on the mechanical properties of the rods. After the nitrogen flow is stopped, the separation continues to decrease while the fill tubes remain cold. Then, as the tubes begin to warm back up, the thermal stress decreases and the support rods begin to expand, causing z_{wires} to increase. After several hours, the thermal stress is greatly reduced, and each rod settles at a final length which, due to hysteresis in the contraction and expansion of fiberglass, is generally different from its value before filling nitrogen. This hypothesis seems consistent with what we observe and with the estimated thermal stresses and compressions of the support rods. I suggest a cure for this problem (not implemented yet) in Section 8.5.1. As a workaround, before using the microscope, we first allow the fill tubes to warm for at least several hours after the most recent filling of the dewar.

8.2 SQUID Noise and Magnetic Dipole Moment Sensitivity

The measured flux noise and the corresponding magnetic field noise values of representative SQUIDs are shown in Table 8.1. The slit SQUID is the same device as that listed in Table 7.1 on page 64, whereas the hole SQUID has the same geometry ($s = 40\,\mu$m) as that of Table 7.1 except that its substrate that has been cut for use with a silicon nitride window (see Section 7.3.3). It is useful to represent the combined effects of the SQUID flux noise and the separation z in terms of the microscope's sensitivity to a magnetic dipole

moment. We can represent the resolution in terms of the spectral density of the magnetic dipole moment noise, $S_m(f)$, which has units of $(\mathrm{A\ m^2})^2/\mathrm{Hz}$. Along the lines of Section 7.3.1, we model the SQUID as a square loop of side $s = A_{eff}^{1/2}$ and assume that the dipole is centrally located above the SQUID and oriented perpendicularly to its plane. The SQUID couples the maximum amount of flux Φ_{max} when $s/z = 2.54$. Table 8.1 lists the dipole moment noise values of the SQUIDs at the respective measured values of z. For the hole SQUID at $z = 15\ \mu\mathrm{m}$, we find $s/z = 2.67$ and that the coupled flux is within 0.15% of Φ_{max}, representing nearly optimal flux coupling. For comparison, at 1 kHz in a 1 Hz bandwidth, the noise amplitude($2.5 \times 10^{-18}\ \mathrm{A\ m^2}$) corresponds to the moment of a single-domain sphere of magnetite (Fe_3O_4) 22 nm in diameter. Furthermore, this noise level is about 450 times lower than the smallest value achieved to date with a low-T_c, warm-sample microscope [37].

8.3 Other Performance Parameters

The time for one fill of liquid nitrogen to boil away is about 29 hours, implying that the average heat leak is about 1.7 W. We estimate that a heat leak of about 0.3 W can be ascribed to the rods and tubes supporting the vacuum can; thermal conduction through the residual gas, with a pressure below 10^{-4} Torr, is negligible. Thus, we infer that radiative heat gain is dominant. In the future, we expect to be able to extend the hold time significantly by wrapping the liquid nitrogen can with many more layers of aluminized mylar. We find that the temperature of the vacuum window is several degrees kelvin below room temperature because of radiative cooling by the SQUID chip. However, by comparing the critical current and voltage modulation of a given SQUID with the values obtained for the same device immersed in liquid nitrogen, we conclude that the temperature of a SQUID mounted at the end of the cold finger is at most 1 K above the temperature of the liquid nitrogen can. This is also true for SQUIDs mounted on silicon basepieces used for the silicon nitride window. To demonstrate the absence of scanning artifacts, we acquired images with no sample present and found that any noise produced by the scanner was less than the intrinsic noise of all SQUIDs currently used.

SQUID	$S_\Phi^{1/2}(1\,\mathrm{Hz})$ ($\mu\Phi_0/\sqrt{\mathrm{Hz}}$)	$S_\Phi^{1/2}(1\,\mathrm{kHz})$ ($\mu\Phi_0/\sqrt{\mathrm{Hz}}$)	$S_B^{1/2}(1\,\mathrm{Hz})$ ($\mathrm{pT}/\sqrt{\mathrm{Hz}}$)	$S_B^{1/2}(1\,\mathrm{kHz})$ ($\mathrm{pT}/\sqrt{\mathrm{Hz}}$)
hole	60	20	72	25
slit	25	17	3.8	2.6

SQUID	$z(measured)$ μm	s μm	s/z	$S_m^{1/2}(1\,\mathrm{Hz})$ ($\mathrm{A\,m^2}/\sqrt{\mathrm{Hz}}$)	$S_m^{1/2}(1\,\mathrm{kHz})$ ($\mathrm{A\,m^2}/\sqrt{\mathrm{Hz}}$)
hole	15	40	2.67	7.5×10^{-18}	2.5×10^{-18}
slit	140	114	0.81	8.4×10^{-17}	5.7×10^{-17}

Table 8.1: Representative SQUID noise performance. $S_\Phi^{1/2}(f)$, $S_B^{1/2}(f)$ and $S_m^{1/2}(f)$ are the magnetic flux, field, and dipole moment noises per unit bandwidth at the specified frequency f. $z(measured)$ is the measured value of the SQUID-sample separation, and s is the effective square loop size of the SQUID.

8.4 Images of George

To illustrate the imaging capabilities of the microscope, we obtained a magnetic image of the ferromagnetic ink particles in a $1.00 bill [41], scanned approximately 150 μm above the SQUID (hole-type, $s = 40$ μm) using the sapphire vacuum window. The resulting image of George Washington and a line scan through it are shown in Figure 8.2. From the line scan we see that a feature 130 μm wide is easily resolved, confirming that a resolution comparable with z is certainly achievable. Figure 8.3 shows a close-up of the eye region imaged at $z = 40\,\mu$m with a silicon nitride window and a hole SQUID ($s = 40$ μm). Again, feature sizes comparable to z are easily resolvable.

8.5 Discussion

8.5.1 Lessons for Future Microscopes

There are several things I learned from the construction and performance of this microscope which may prove useful for future designs. First, given the intrinsic noise levels of high-Tc SQUIDs, many of the fiberglass dewar parts could instead have been made out of nonmagnetic metals without contributing significant Nyquist noise. This would have made machining the dewar somewhat easier. Second, it would be useful to have a high-power optical microscope equipped with a camera integrated on top of the SQUID system. This would allow us to overlay an optical image on top of a magnetic image. Of course, this would only work in the case of thin or transparent samples, since the SQUID and the optical microscope would see opposite sides of the sample. However, for opaque samples, one should be able to devise a way to place an optical objective on the same side as the SQUID and with a well-defined lateral offset from it. This would allow magnetic and optical images of the same sample side to be referenced with respect to one another. Third, in order to minimize the vertical force exerted on the nitrogen can by the thermal contraction of the fill tubes, one could insert thin-walled, low-spring-constant bellows at one point along each tube. This would relax the thermal stresses and greatly decrease the drift in z.

8.5.2 Even Smaller z?

It should be possible to improve upon the present design and achieve SQUID-sample separations of only a few micrometers, comparable with what cold-sample micro-

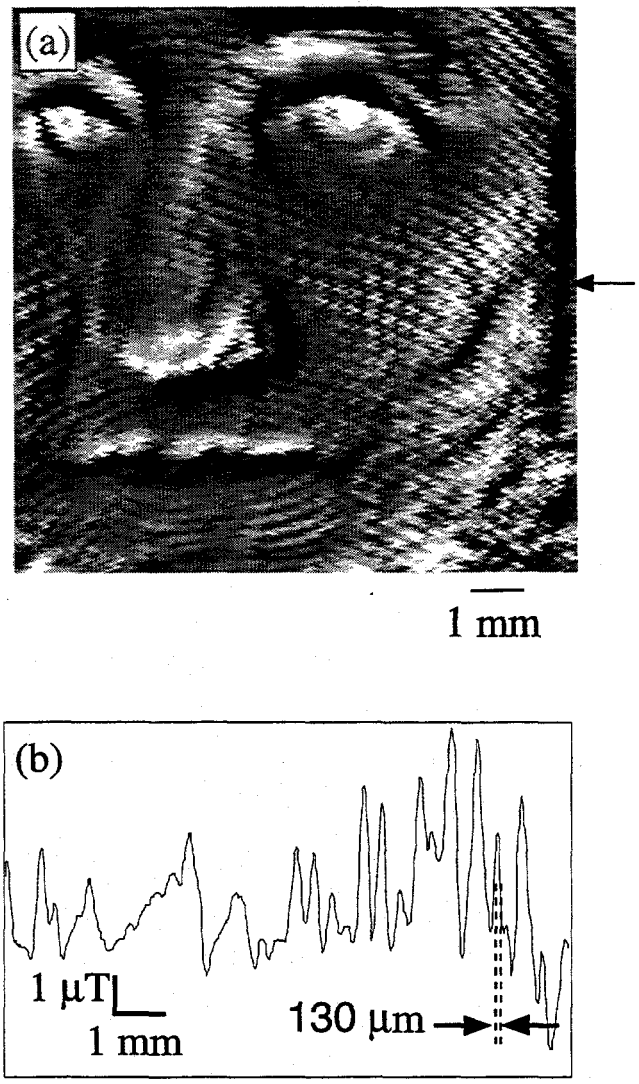

Figure 8.2: (a)Magnetic image of a portion of a $1.00 bill scanned 150 μm above a SQUID using the sapphire vacuum window. The gray scale varies from about -9 μT(black) to +10 μT(white). (b)Line scan of the magnetic field along the horizontal line indicated by an arrow in (a).

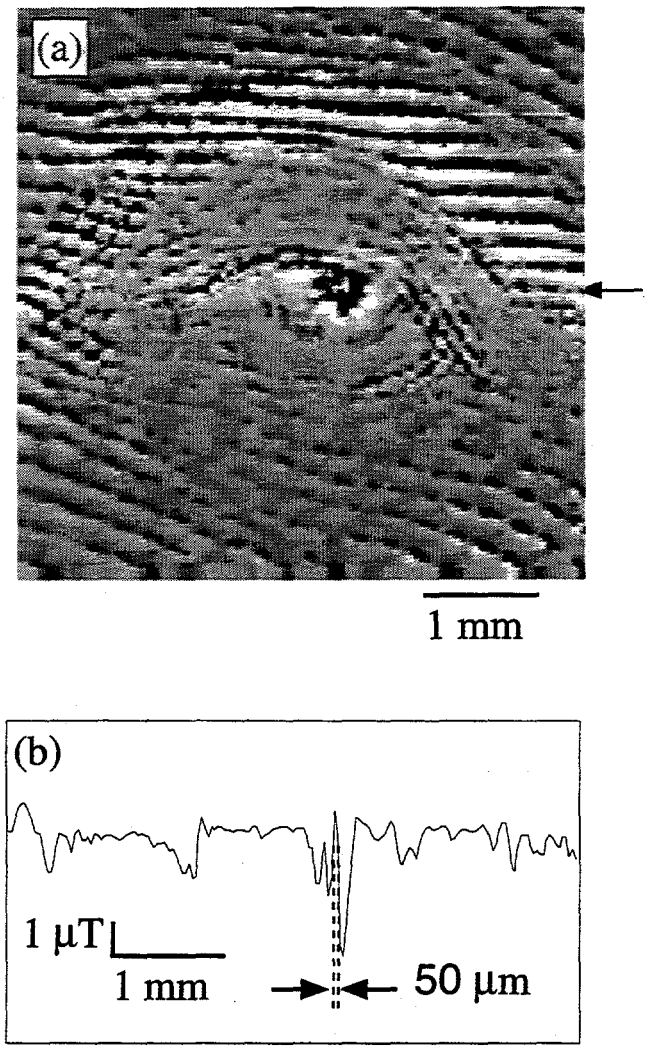

Figure 8.3: (a)Close-up image of George Washington's eye on a $1.00 bill scanned using a silicon nitride vacuum window with $z = 40$ μm. The gray scale varies from about - μT(black) to + μT(white). (b)Line scan of the magnetic field along the horizontal line indicated by an arrow in (a).

scopes can presently achieve. The silicon nitride window can easily be made smaller in area and thickness. It should also be possible to cut and handle SQUID chips less than 100 μm on a side using micromanipulation instruments. In order to cancel out residual thermal drifts, it may be necessary to incorporate an active feedback system to maintain the SQUID-window separation. At such small separations, room dust caught between the window and the sample may start to limit the minimum z. In order to reduce this effect, the area of the window substrate (not just the window itself) should be made as small as possible, and the window and the sample surface should be thoroughly cleaned and maintained in a dust-free environment. Due to the small window substrate area, it will be more difficult to maintain parallelism between the window and sample planes while scanning. Hence, a non-contact method of scanning (leaving a constant gap between the sample and the window of less than 1 μm) may have to be implemented.

8.5.3 Re-Examining Low-Tc Warm-Sample Microscopes

The elimination of radiation shielding between the SQUID and the vacuum window is the main reason why high-Tc microscopes have achieved values of z much smaller than those obtained by low-Tc warm-sample systems. However, if one calculates the equilibrium temperature of a low-Tc device mounted on a sapphire cold finger, one finds that there is no *fundamental* reason why a low-Tc device cannot operate without radiation shielding as well. Hence, in principle, it should be possible to achieve the same reductions in z with a low-Tc microscope as have been achieved with high-Tc systems. The presence of significant interfacial thermal resistances in the thermal path between the pick-up loop and the helium bath (such as that between the sensor chip and the end of the finger) most likely explains the present need for radiation shielding. Perhaps reductions of these stray thermal resistances and improvements in cooling power, such as those possible with helium flow cryostats, would allow low-Tc devices to operate without radiation shields.

Chapter 9

Magnetotactic Bacteria

9.1 Introduction

I began exploring various problems in biology soon after the completion of the work described in Part I of this thesis. I was motivated by a long-standing interest in biology and a desire to find an interdisciplinary project for the remainder of my dissertation. I spent several months working in a biochemistry laboratory and educating myself about current knowledge in a variety of subfields in biology. It was during this time that I first learned about magnetotactic bacteria.

Richard Blakemore discovered magnetotactic bacteria in 1975, while examining mud samples collected from a marsh near Woods Hole, Massachusetts [48]. Numerous species of magnetotactic micro-organisms have since been discovered [49]. In most magnetotactic bacteria, single-domain magnetite (Fe_3O_4) particles, or magnetosomes, are arranged in one or multiple chains aligned roughly parallel with the body axis (Figure 9.1(a)). A magnetosome is typically 50 nm in diameter and is biochemically generated by the bacterium. The magnetosome dipoles in a single chain are aligned parallel to the chain axis. The net moment of a chain is typically $5 \times 10^{-16}\,\mathrm{A\,m^2}$, which gives a magnetic alignment energy in the earth's magnetic field of about $10k_BT$ at room temperature [50]. Hence, the bacteria tend to align and swim along the earth's magnetic field lines. Each bacterium typically has one or several tails ("flagella") which propel it. Many species utilize the ability to align with the earth's field as an aid to survival. Since the earth's field is inclined with respect to the earth's surface (except at the equator), bacteria can use the field to distinguish between upwards and downwards. For example, in the Northern hemisphere, certain

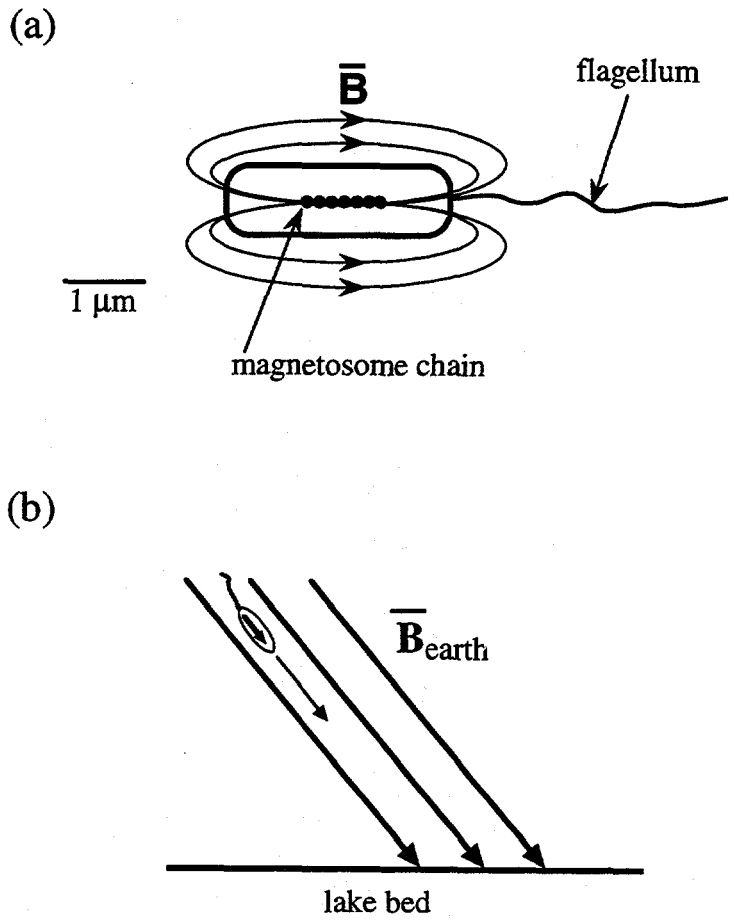

Figure 9.1: (a)Schematic of magnetotactic bacterium. (b)Migration of bacterium down the inclined geomagnetic field.

singly-flagellated species swim down along the inclined field lines towards nutrient-rich sediments (Figure 9.1(b)) [50]. In the Southern hemisphere, the polarity of the magnetosome chain in bacteria of the same species is reversed. These bacteria still swim downwards because the vertical component of the earth's field is also reversed in the Southern hemisphere. Essentially, any bacterium with the "wrong" polarity in a given hemisphere will tend to swim upwards towards the air-water interface where lethal concentrations of oxygen exist. Therefore, "North-seeking" bacteria predominate in the Northern hemisphere, and "South-seeking" bacteria populate the Southern hemisphere. Since the field is parallel to the earth's surface at the equator, the selection mechanism is inactive, and approximately equal numbers of both polarities are found there [50].

It was clear to me that the translational and rotational motion of magnetotactic bacteria could be sensed by a SQUID. In fact, it seemed that a SQUID, if placed sufficiently close to the sample, could sense the dipole moment of a single swimming bacterium. In addition, my experience with measuring flux spectral densities of high-Tc superconductors led me to wonder what the magnetic flux noise produced by these bacteria looked like. The intriguing possibility of exploring the dynamics of these organisms was a major impetus for me to build the microscope.

9.2 Experiments in Free Solution and Zero Magnetic Field

9.2.1 Experimental Set-up

The first experiments Yann Chemla and I carried out focused on measuring the bacteria in free solution and in nominally zero magnetic field, which means that the magnetic alignment energy of the bacteria due to residual AC or DC fields was less than k_BT. The magnetic shields attenuate enivironmental fields such that they contribute less than $0.001k_BT$ for a bacterium dipole moment of 5×10^{-16} A m^2. During the operation of the SQUID, the SQUID electronics feed AC and DC currents to the feedback coil immediately below the SQUID, in close proximity to the sample. The 100 kHz AC field was always less than 0.4 μT in amplitude, and the DC field was kept below about 3 μT. These components contributed only $0.05k_BT$ and $0.4k_BT$, respectively.

Figure 9.2 shows the basic schematic of the experiment (note that the figure is not drawn to scale). An inverted silicon nitride window (440 x 440 μm, 3 μm thick) is used as

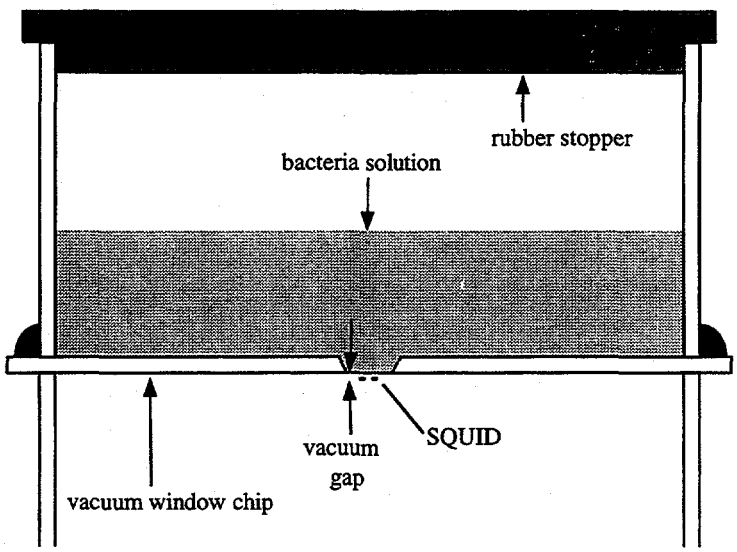

Figure 9.2: Experimental set-up for free-solution bacteria measurements. Cold finger not shown for clarity. Not drawn to scale.

the sample well. This allows the SQUID (hole-type, $s = 40\ \mu$m) to be positioned within a few tens of micrometers of the sample bottom. In order to form a large reservoir of bacteria solution, a quartz tube is sealed with Crystalbond 509 adhesive (Aremco, Inc.) to the top of the window chip. Another quartz tube is glued to the bottom of the chip, as with other vacuum windows described previously, to allow mounting on the microscope. Aluminum wires patterned on the vacuum-side of the window are used to measure the SQUID-window distance with the mutual inductance technique. A rubber stopper is inserted into the top of the upper quartz tube to prevent leakage of air into the sample chamber. The temperature of the well due to radiative cooling by the SQUID chip was measured to be about 18.5°C (1.5°C below the temperature of the room), which is within the allowed range for bacteria of the type we examined.

Since the liquid cell is rigidly fixed to the window-adjustment mechanism of the microscope, we cannot laterally scan the sample relative to the SQUID. The SQUID is positioned a few tens of micrometers below the window, as shown in Figure 9.2. Using a digital spectrum analyzer, we measure the spectral density of the SQUID output and acquire time traces.

9.2.2 Culturing and Handling Bacteria

Professor Dennis Bazylinski of Iowa State University kindly provided us with starting cultures of the magnetotactic bacterium *Magnetospirillum magnetotacticum*, or MS-1. These bacteria typically live at the sediment-water interface near the bottoms of lakes. The spiral-shaped body contains a magnetosome chain having an average dipole strength of about 1.3×10^{-15} A m^2, representing a magnetic energy of about 16 $k_B T$ in the earth's field ($5 \times 10^{-}5$ T) [50]. There is typically one flagellum on each end of the body, allowing the bacterium to swim bi-directionally. This species must be cultured in specially-prepared liquid media with precisely controlled oxygen concentrations. Optimal growth and magnetosome production occurs when the O_2 concentration is on the order of 1%. Magnetite synthesis shuts down at concentrations substantially higher than this [51].

Mike Adamkiewicz (of Professor Bob Buchanan's group) and Yann developed self-sustaining cultures based on protocols provided by Professor Bazylinski. A typical growth curve is shown in Figure 9.3. The doubling time during the logarithmic growth phase, in which the logarithm of the cell number density increases linearly with time, is about 10

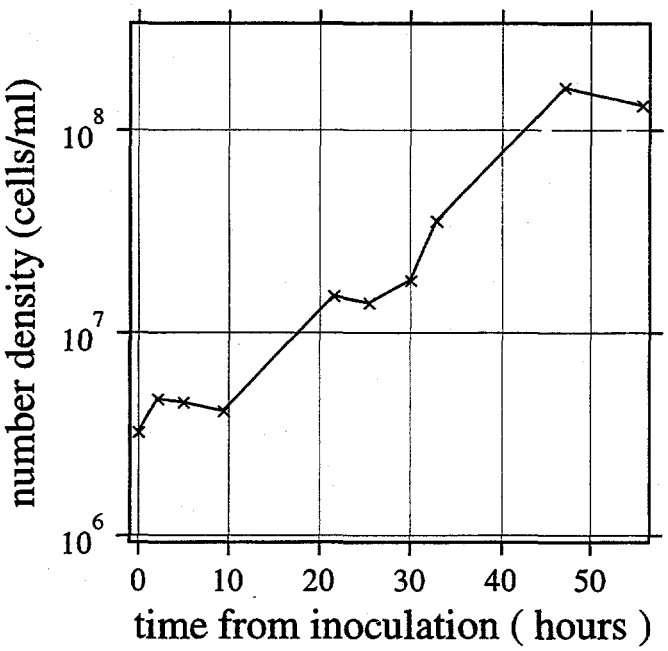

Figure 9.3: Representative growth curve for magnetotactic bacteria MS-1.

hours, and the time from inoculation to saturation is about 50 hours. The cell concentrations reflect the total number of bacteria, whether alive or dead. In our SQUID measurements, we sampled bacteria from the log-phase of growth, when the bacteria are presumably the healthiest.

Before inserting bacteria into the liquid well, Yann and Mike confirm that more than 90% of the bacteria are swimming by observing an aliquot of the solution under a phase-contrast optical microscope. This insures that the net magnetic signal from the culture will be dominated by swimming, or motile, bacteria. Non-motile or dead bacteria generate magnetic fluctuations characteristic of thermal Brownian motion, which will be discussed in detail below. Our initial goal was to measure the signal from swimming bacteria, so we needed to minimize the contribution from non-swimming cells.

Once the culture solution exhibits high motility and high cell concentration (at least 1×10^7 cells/ml), we then prepare the sample well on the microscope in the following way. First, we clean the well with ethanol, RBS soap and de-ionized water. After the rubber stopper is inserted, we flush the well with a gas mixture composed of $1\%0_2/99\%N_2$ using inlet and outlet syringe needles pressed through the stopper. We inject the bacteria solution into the well using a third needle and then remove the gas needles.

Keeping the cells alive in the sample well for long periods of time proved to be difficult. Several well designs proved inadequate before we finally settled on the type described above. We suspect that previous wells allowed lethal levels of oxygen to leak or diffuse into the sample chamber, thereby killing the cells. Furthermore, in the present well, a larger volume (about 1 ml) of bacteria solution can be accomodated, which greatly dilutes any residual chemical or oxygen contamination. However, even with this well design, the bacteria solutions do not maintain more than 90% motility after 12 hours, whereas bacteria left in the original culture bottle do. The cause of this long-term degradation in the well is not known. However, for the free-solution experiments described below, more than 90% of the bacteria were motile over the duration of each measurement(several hours), except when they were intentionally lysed by the addition of formalin or iodine.

9.2.3 Flux Spectral Density: Motile vs Non-Motile

Figure 9.4 shows flux spectral densities for motile ($> 90\%$ of population) and non-motile bacteria measured by Yann. The cell number density was 4.4×10^7 cells/ml, dilute

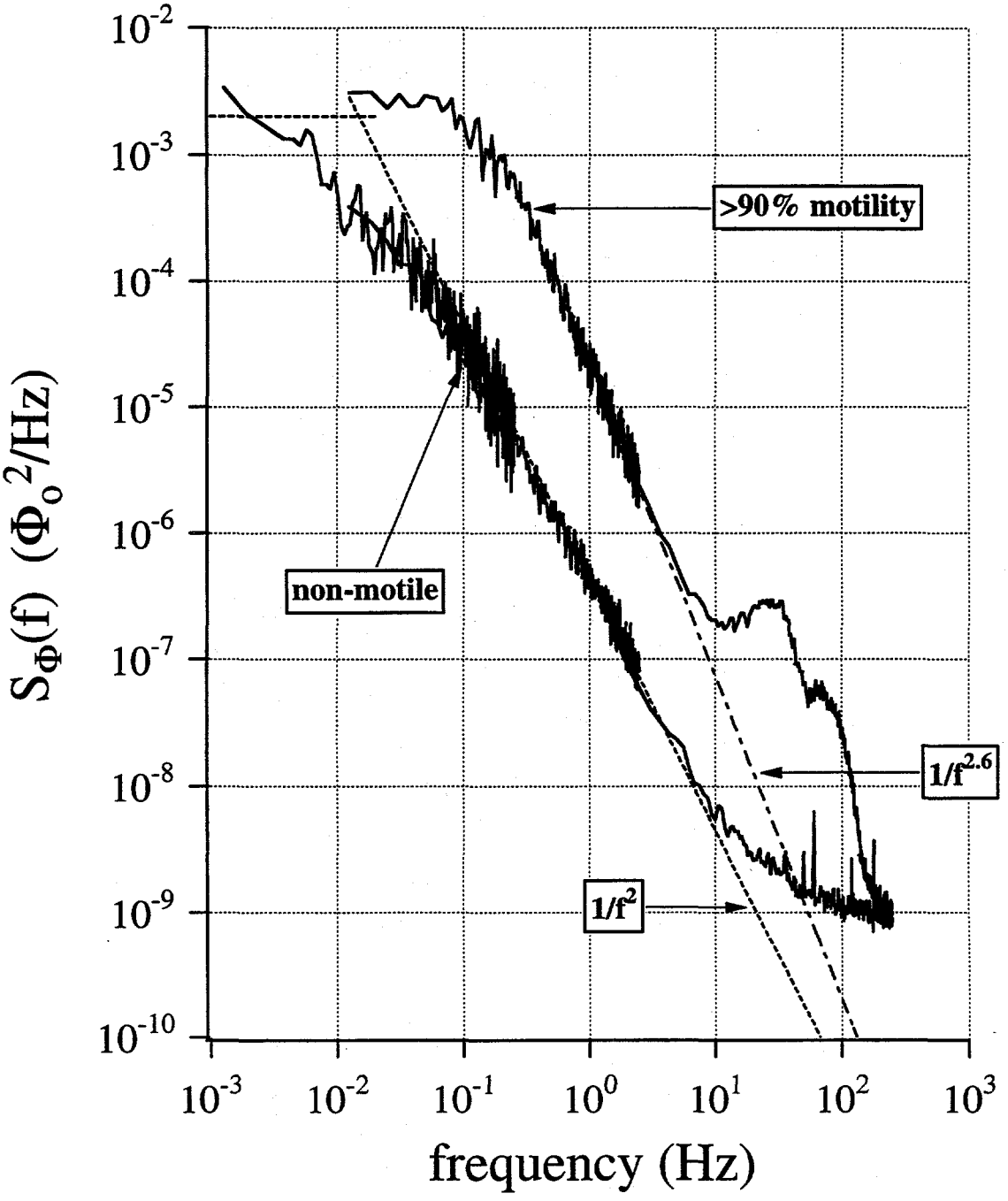

Figure 9.4: Flux spectral densities of magnetotactic bacteria MS-1 in free solution. The upper trace is for a solution with more than 90% swimming bacteria. The lower trace is the signal from the same solution after the addition of formalin to halt swimming. The dashed lines indicate how the approximate knee frequency of the lower trace is extracted. The dashed-dotted line shows the extrapolated $1/f^{\alpha}$-part of the upper trace.

enough so that cell-to-cell magnetic interactions were negligible. The separation between the SQUID and the liquid-side of the window was about 25 μm, and the volume of bacteria solution in the well was about 400 μl. The spectrum for motile bacteria exhibits two high frequency peaks at 26 $\pm$ 3 Hz and 70 $\pm$ 5 Hz. Such peaks have been observed in optical measurements of other bacteria by Lowe, Meister, and Berg [52]. These authors attribute the peaks to the action of the bacterial flagella on the body. Figure 9.5(a) shows a physical interpretation of the peaks, drawn in the rest frame of a flagellum (the other flagellum is not shown). For simplicity, we take the magnetosome chain to be exactly parallel with the body axis, $\hat{\mathbf{z}}_b$.

The higher frequency peak arises from the gyration of $\hat{\mathbf{z}}_b$ with respect to a gyration axis, $\hat{\mathbf{z}}_g$, at the rotation frequency of the flagellum (Figure 9.5(a)). The half-angle of the cone around which the magnetosome chain gyrates is θ_g. Berg has attributed this motion to a net imbalance in the drag forces on the flagellum perpendicular to the flagellum axis [53]. This occurs when the helical flagellum contains a non-integral number of turns along its length. The peak frequency ($\approx$ 70 Hz) is comparable with typical flagellar rotation rates observed for other bacteria [54, 55].

The lower frequency peak represents the precession of $\hat{\mathbf{z}}_g$ around the flagellum axis, $\hat{\mathbf{z}}_f$ (Figure 9.5(a)). This occurs in order to equalize the torque generated by the flagellum and has been observed for other bacteria whose flagella were attached to surfaces [56]. The precession rate ($\approx$ 26 Hz) is smaller than that of the flagellum due to the mismatch in hydrodynamic drag between the flagellum and the body. The precession angle, θ_p, is related to the angular misalignment between the axis of the flagellum and the body axis.

We have observed that the peaks sometimes shift to lower frequencies over time, as shown in Figure 9.6 (note that the upper two traces have been offset for clarity). In Figure 9.7, I subtract the $1/f^{2.6}$-part of each spectrum underlying the peaks and expand the frequency axis in order to see the peaks more clearly. The ratio between the two peak frequencies seems to remain roughly constant ($f_g/f_p = 2.7 \pm 0.2$) when the peaks shift. This bolsters the interpretation of these peaks as being derived from a single source, namely flagellar rotation. Perhaps chemical or gas contamination causes the flagellar rotation to slow, although this must be further examined experimentally.

The ratio between the heights of the peaks also seems to stay constant when the peak frequencies shift [$S_\Phi(f_p)/S_\Phi(f_g) = 5.3 \pm 0.5$]. A physical interpretation of this ratio can be deduced from Figure 9.5(b), which shows vector components of the magnetosome dipole

(a)

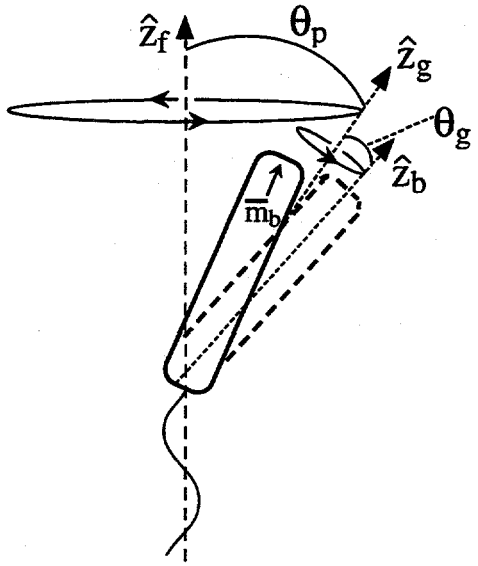

(b)

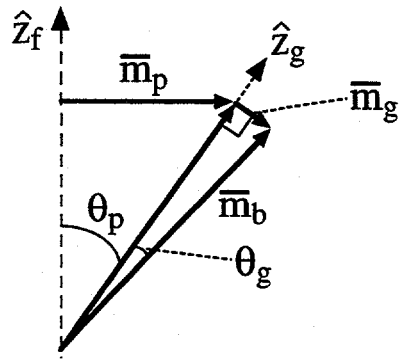

Figure 9.5: (a)Schematic of simultaneous precession and gyration of bacterium as viewed in the rest frame of the flagellum. $\overline{\mathbf{m}}_b$ is the magnetic dipole moment of the bacterium. Other variables defined in the text. (b) Vector components of the bacterium dipole moment. $\overline{\mathbf{m}}_g$ and $\overline{\mathbf{m}}_p$ rotate at frequencies f_g and f_p, respectively.

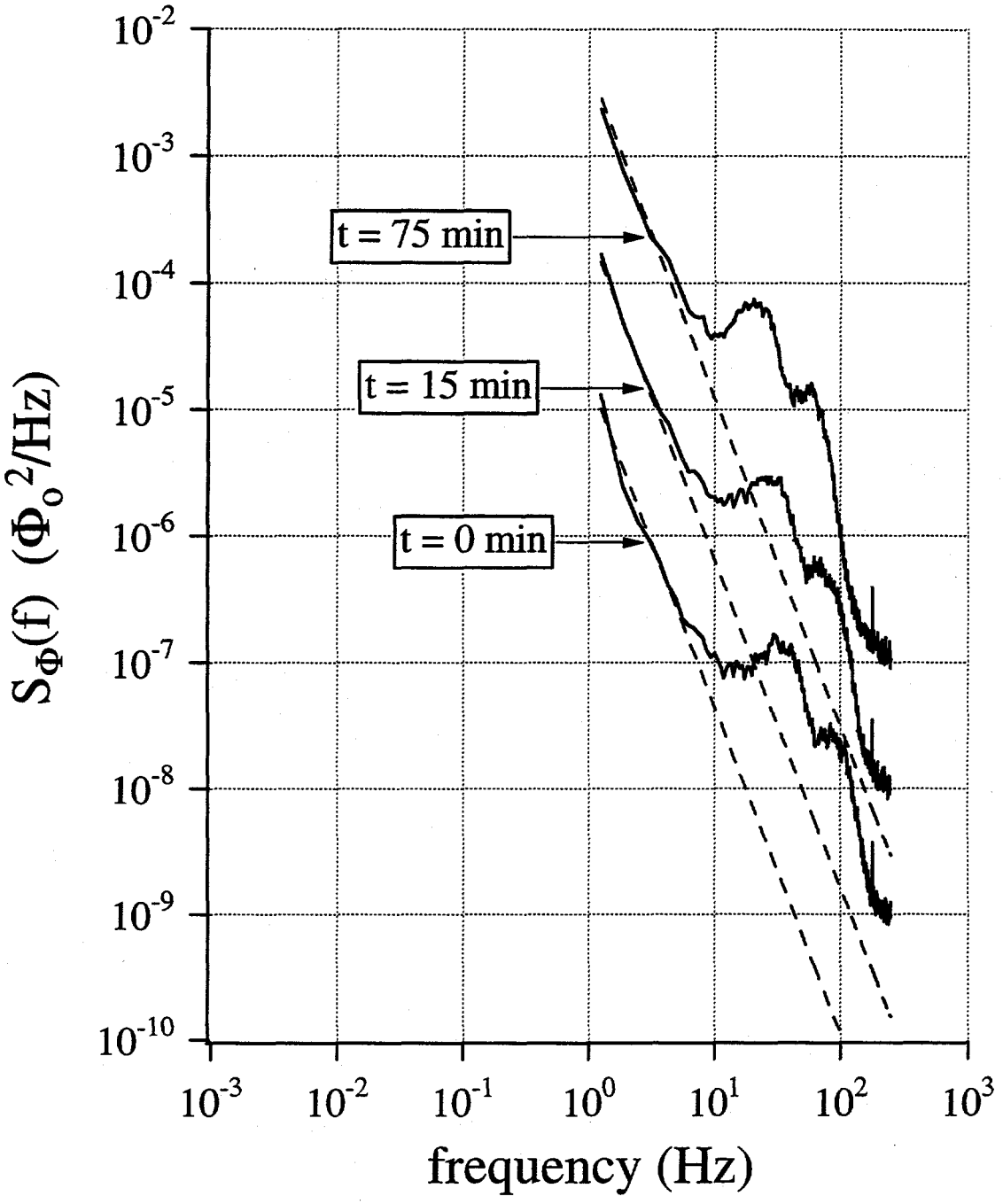

Figure 9.6: Spectra of motile bacteria acquired at successive times. The t = 15 min and 75 min traces have been multiplied by factors of 10 and 100, respectively, to offset the curves for clarity. The t = 15 min spectrum is the high-frequency part of the upper curve shown in Figure 9.4. The dashed lines indicate the extrapolated $1/f^{2.6}$-part of each spectrum.

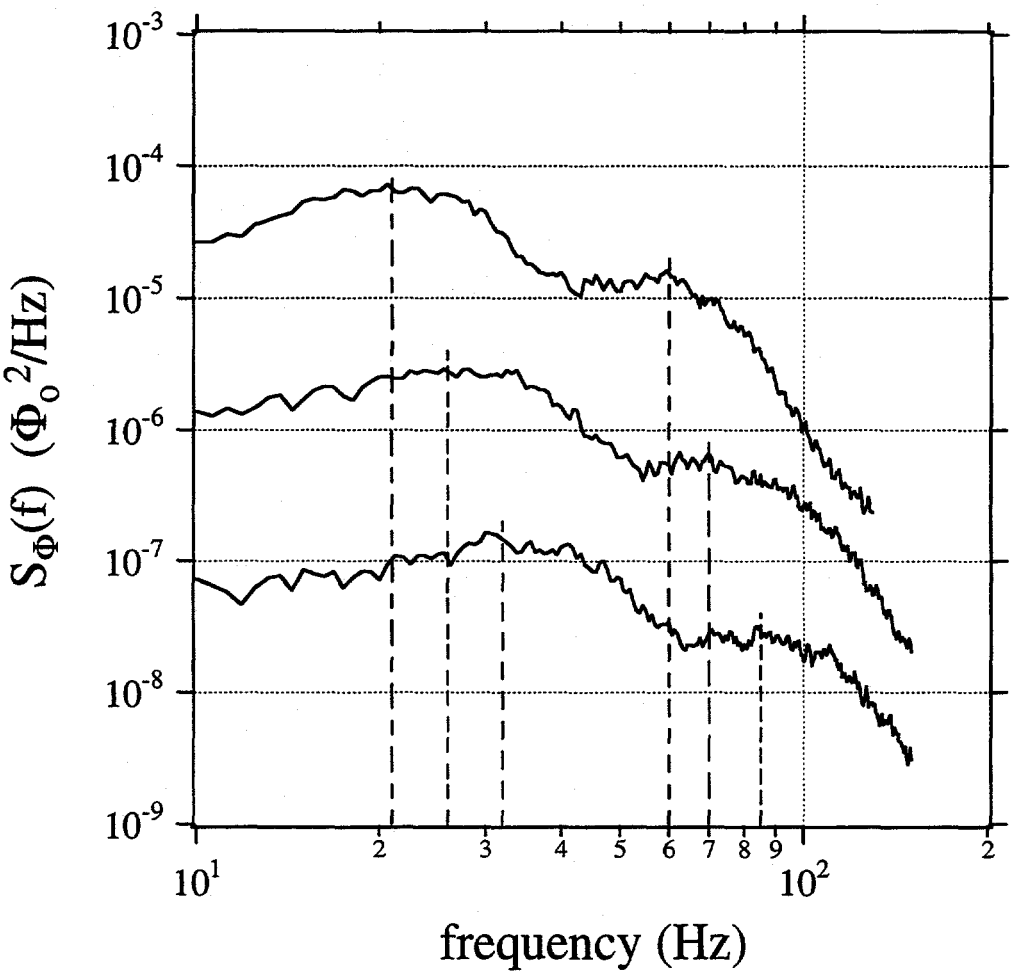

Figure 9.7: Expanded-view of the motile-bacteria spectra of Figure 9.6 with the $1/f^\alpha$-backgrounds (dotted lines in Figure 9.6) subtracted away. The lower, middle, and upper curves correspond to t = 0, 15 and 75 min, respectively. The vertical dotted lines represent the estimated peak positions. The middle and upper curves are multiplied by factors of 10 and 100, respectively, to shift them upwards for the sake of clarity.

moment derived from the model in Figure 9.5(a). The dipole vector $\overline{\mathbf{m}}_g$ rotates in a plane at frequency f_g, corresponding to the gyration of $\hat{\mathbf{z}}_b$ around $\hat{\mathbf{z}}_g$. Similarly, $\overline{\mathbf{m}}_p$ rotates in a plane at frequency f_p due to the precession of $\hat{\mathbf{z}}_g$ around $\hat{\mathbf{z}}_f$. The magnitudes of these vector components are: $|\overline{\mathbf{m}}_g| = m_b sin(\theta_g)$ and $|\overline{\mathbf{m}}_p| = m_b cos(\theta_g) sin(\theta_p)$. Over a large population of bacteria in nominally zero magnetic field, the directions of $\overline{\mathbf{m}}_g$ and $\overline{\mathbf{m}}_p$ at a given instant of time are uniformly distributed over all directions *in the laboratory frame of reference.* Hence, the measured flux spectral densities are averaged over all possible orientations of these two vectors. This implies that:

$$\frac{S_\Phi(f_p)}{S_\Phi(f_g)} = \frac{|\overline{\mathbf{m}}_p|^2}{|\overline{\mathbf{m}}_g|^2} = \frac{sin^2(\theta_p)}{tan^2(\theta_g)} \tag{9.1}$$

For relatively small θ_p and θ_g, we have $S_\Phi(f_p)/S_\Phi(f_g) \approx \theta_p^2/\theta_g^2$. This yields: $\theta_p/\theta_g \approx \sqrt{S_\Phi(f_p)/S_\Phi(f_g)} = 2.3 \pm 0.1$. To my knowledge, this is the first measurement of θ_p/θ_g for a particular species of bacteria. In contrast, the interpretation of the relative peak heights measured by Lowe et al. [52] is uncertain, due to the nonlinear response of their optical detector.

As shown in Figure 9.4, the flux spectral density of the motile bacteria rises in a $1/f^\alpha$-like fashion (where $\alpha \approx 2.6$) at low frequencies, and levels off below a characteristic knee frequency, $f_k(motile) \approx 0.13$ Hz. The frequency $f_k(motile)$ most likely is related to both the average time between changes in swimming direction and the average traversal time of a bacterium across the SQUID washer. Numerical simulations will be required to relate the values of $f_k(motile)$ and α to fundamental swimming parameters. However, if we assume that the rotational motion due to changes in swimming direction is what determines $f_k(motile)$, then the average time between directional changes is roughly given by $\tau(motile) = 1/2\pi f_k(motile) \approx 1.2$ sec.

When 50 μl of formalin is injected into the sample, the bacteria almost immediately lose their motility, and the spectral density transforms to the lower curve in Figure 9.4. The high-frequency peaks completely disappear, and the knee frequency shifts to a lower value. The flux fluctuations produced by Brownian rotation of the bacteria dominate the spectrum. The translational Brownian motion of non-swimming bacteria significantly contributes to the spectral density only at frequencies below our experimental bandwidth. For example, since the mean time for a non-swimming bacterium to diffuse across the SQUID washer (40 μm) is about 7000 seconds, the knee frequency for translational diffusion is on the order of

10^{-5} Hz. In contrast, for swimming bacteria (speed $\approx$ 10 - 100 μm/sec), the traversal time is of order 1 second, corresponding to a frequency of about 1 Hz.

The flux spectral density produced by Brownian rotation of bacteria having *uniform* size can be calculated from the Langevin equation (unpublished calculation by Yann and me). For a large ensemble of non-motile bacteria, the spectral density is given by the sum of two Lorentzians:

$$S_{\Phi}^{Brownian\,rot.}(f) = K_1 \frac{2\tau_r}{1+(2\pi\tau_r f)^2} + K_2 \frac{2(\tau_r/2)}{1+(2\pi(\tau_r/2)f)^2} \tag{9.2}$$

where τ_r is the rotational relaxation time, and K_1 and K_2 are constants with units of Φ_o^2. The reason for this form of the spectral density can be understood in the following way. Let us focus on the vertical component of the magnetic field in the plane of the SQUID, $B_z(x,y,z,\theta_b,\phi_b)$, generated by a single bacterium, as shown in Figure 9.2.3. The SQUID is parallel to the x-y plane, so that the total coupled flux is given by the integral of $B_z(x,y,z,\theta_b,\phi_b)$ over the area of the SQUID hole. The magnetic field produced by the dipole of the bacterium is given by:

$$B_z(x,y,z,\theta_b,\phi_b) = \frac{\mu_o m_b}{4\pi r^3}[\frac{3z}{r^2}(xsin\theta_b cos\phi_b + ysin\theta_b \sin\phi_b + zcos\theta_b) - cos\theta_b] \tag{9.3}$$

where μ_o is the free-space permeability, and m_b is the dipole moment of the bacterium. We now assume that only θ_b and ϕ_b vary with time. In reality, $\bar{\mathbf{r}}$ also changes over time due to Brownian translation, but on a timescale that is much longer than that of our measurement (see argument of the previous paragraph). So the assumption of a translationally-fixed bacterium is a good approximation.

We can write the correlation function for the total flux of the bacterium captured by the SQUID:

$$\begin{aligned} &< \Phi(z,\theta_b(0),\phi_b(0))\Phi(z,\theta_b(t),\phi_b(t)) >= \\ &\quad < [\int B_z(x,y,z,\theta_b(0),\phi_b(0))dxdy][\int B_z(x',y',z,\theta_b(t),\phi_b(t))dx'dy'] >, \end{aligned} \tag{9.4}$$

where the integrals area taken over the area of the SQUID. Since x, y, x', y' do not change over the ensemble, we can bring the ensemble-average brackets inside the integrals:

$$\begin{aligned} &< \Phi(z,\theta_b(0),\phi_b(0))\Phi(z,\theta_b(t),\phi_b(t)) >= \\ &\quad \int\int < B_z(x,y,z,\theta_b(0),\phi_b(0))B_z(x',y',z,\theta_b(t),\phi_b(t)) > dxdydx'dy'. \end{aligned} \tag{9.5}$$

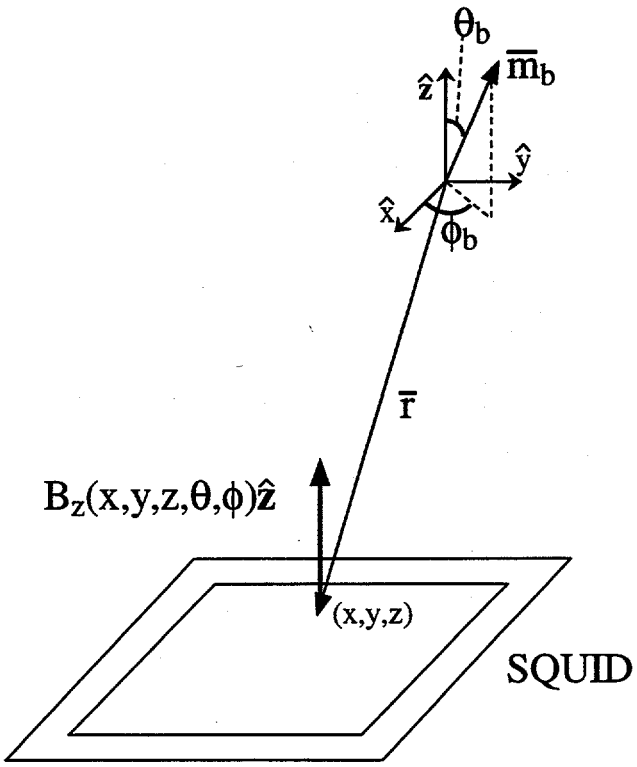

Figure 9.8: Schematic used to calculate the field produced by a bacterium. The origin (0,0,0) is at the position of the bacterium.

From Equation 9.3, one can see that the field-correlation function, $< B_z(x,y,z,\theta_b(0),\phi_b(0))B_z(x',y',z,\theta_b(t),\phi_b(t)) >$, will include correlation functions of products of trigonometric terms: $< sin\theta_b(0)cos\phi_b(0)sin\theta_b(t)cos\phi_b(t) >$, $< sin\theta_b(0)sin\phi_b(0)cos\theta_b(t) >$, etc. If we assume that $\theta_b(t)$ and $\phi_b(t)$ are independent, we can factorize each correlation function into θ_b and ϕ_b parts; for example, $< sin\theta_b(0)cos\phi_b(0)sin\theta_b(t)cos\phi_b(t) >=< sin\theta_b(0)sin\theta_b(t) >< cos\phi_b(0)cos\phi_b(t) >$.

From Langevin's equation, one can show that $< f(0)g(t) >=< f(0)g(0) > e^{-t/\tau_r}$, where f and g are each either *sin* or *cos*. But many of the ensemble averages at $t = 0$, such as $< sin\theta_b(0)cos\theta_b(0) >$ and $< cos\theta_b(0) >$, are equal to zero, so that we arrive at the following expression for the field correlation function:

$$\begin{aligned} < B_z(x,y,z,\theta_b(0),\phi_b(0))B_z(x',y',z,\theta_b(t),\phi_b(t)) >= (\frac{\mu_o m_b}{4\pi r^3})^2\times \\ \{(\frac{3xz}{r})(\frac{3x'z}{r'}) < sin\theta_b(0)sin\theta_b(t) >< cos\phi_b(0)cos\phi_b(t) > \\ +(\frac{3xy}{r})(\frac{3x'y'}{r'}) < sin\theta_b(0)sin\theta_b(t) >< sin\phi_b(0)sin\phi_b(t) > \\ +(\frac{3z^2}{r^2}-1)(\frac{3z^2}{(r')^2}-1) < cos\theta_b(0)cos\theta_b(t) >\}. \end{aligned} \tag{9.6}$$

By inserting the expressions for the trigonometric correlation functions, we obtain:

$$\begin{aligned} < B_z(x,y,z,\theta_b(0),\phi_b(0))B_z(x',y',z,\theta_b(t),\phi_b(t)) >= (\frac{\mu_o m_b}{4\pi r^3})^2\times \\ \{[(\frac{3xz}{r})(\frac{3x'z}{r'}) < sin^2\theta_b(0) >< cos^2\phi_b(0) > + \\ \frac{3xy}{r})(\frac{3x'y'}{r'}) < sin^2\theta_b(0) >< sin^2\phi_b(0) >]e^{-2t/\tau_r} + \\ (\frac{3z^2}{r^2}-1)(\frac{3z^2}{(r')^2}-1) < cos^2\theta_b(0) > e^{-t/\tau_r}\}. \end{aligned} \tag{9.7}$$

By using this expression in Equation 9.5, one can see that the integrals over x, y, x', and y' will determine the coefficients in front of each of the time-dependent exponential terms in the final expression for $< \Phi(z,\theta_b(0),\phi_b(0))\Phi(z,\theta_b(t),\phi_b(t)) >$. Thus, the Fourier transform of $< \Phi(z,\theta_b(0),\phi_b(0))\Phi(z,\theta_b(t),\phi_b(t)) >$, which is the flux spectral density, is the sum of two Lorentzians of the same form as in Equation 9.2 (the Fourier transform of e^{-at} is a Lorentzian). Furthermore, if we assume that all the bacteria in the ensemble are independent of each other (a good assumption at number densities of interest), then the contributions of individual bacteria simply add together. Hence, the total flux spectral density of non-motile bacteria can be expressed as the sum of two Lorentzians (Equation 9.2)

with coefficients (K_1 and K_2) depending on the measurement geometry (SQUID size, sample size, etc.) and the number density of bacteria.

The roll-off frequency, $f_k(Brownian)$, of Equation 9.2 is on the order of $1/2\pi\tau_r$. The relaxation time τ_r is approximately the average time it takes for a bacterium to execute a full rotation by Brownian motion. For a finite cylinder, which crudely approximates the shape of an MS-1 bacterium, the relaxation time for "propeller"rotation modes is [57]:

$$\tau_r = \frac{\pi\eta L_b^3}{3k_BT}(ln\frac{L_b}{d_b} - \gamma)^{-1}\,, \tag{9.8}$$

where d_b and L_b are the effective bacteria diameter and length, respectively, η is the viscosity of the carrier fluid, and the correction $\gamma \approx (0.662 - 0.92d_b/L_b)$ is due to the cylinder ends. Hence, in the limit of $L_b \gg d_b$, τ_r is proportional to L_b^3, so that $f_k(Brownian) \propto 1/L_b^3$.

Note that the experimental curve for non-motile bacteria in Figure 9.4 rolls off as $1/f^2$ at high frequencies, consistent with Brownian rotation. However, the low-frequency roll-off is not well-modeled by Equation 9.2. I believe that this is caused by a distribution of bacteria lengths (L_b), giving rise to a superposition of spectral densities with different τ_r. In principle, one could fit the measured spectrum by assuming that the distribution of τ_r has a specific form, such as a Gaussian. However, this would yield uncertain results, at best, for two reasons. First, as shown in Figure 9.4, we did not measure the low-frequency-part of the roll-off, for fear that long-term thermal drifts in the SQUID-window separation would cause the window to crash into the SQUID. Second, we presently do not have independent knowledge of the type of distribution function appropriate for τ_r.

However, for the sake of argument, we can extract rough estimates for the average values of $f_k(Brownian)$ and τ_r by noting the intersection of the two dashed lines shown in Figure 9.4. This yields $\overline{f_k(Brownian)} \approx 0.015$ Hz or $\overline{\tau_r} \approx 11$ sec. Assuming that $d_b = 1\,\mu$m, we use Equation 9.8 to get $\overline{L_b} \approx 3.5\,\mu$m, which is in a range consistent with observations using an optical microscope. If we interpret $\tau(motile) \approx 1.2$ sec as the time between changes in swimming direction, then we see that the average rotation time decreases by about a factor of 9 when swimming is halted. This would imply that swimming bacteria change direction significantly more often than non-swimming bacteria that are subject only to Brownian motion.

Figure 9.9 shows a measurement on a different solution of non-motile bacteria, in which the spectral density is closer to the form of Equation 9.2. Presumably, the distribution

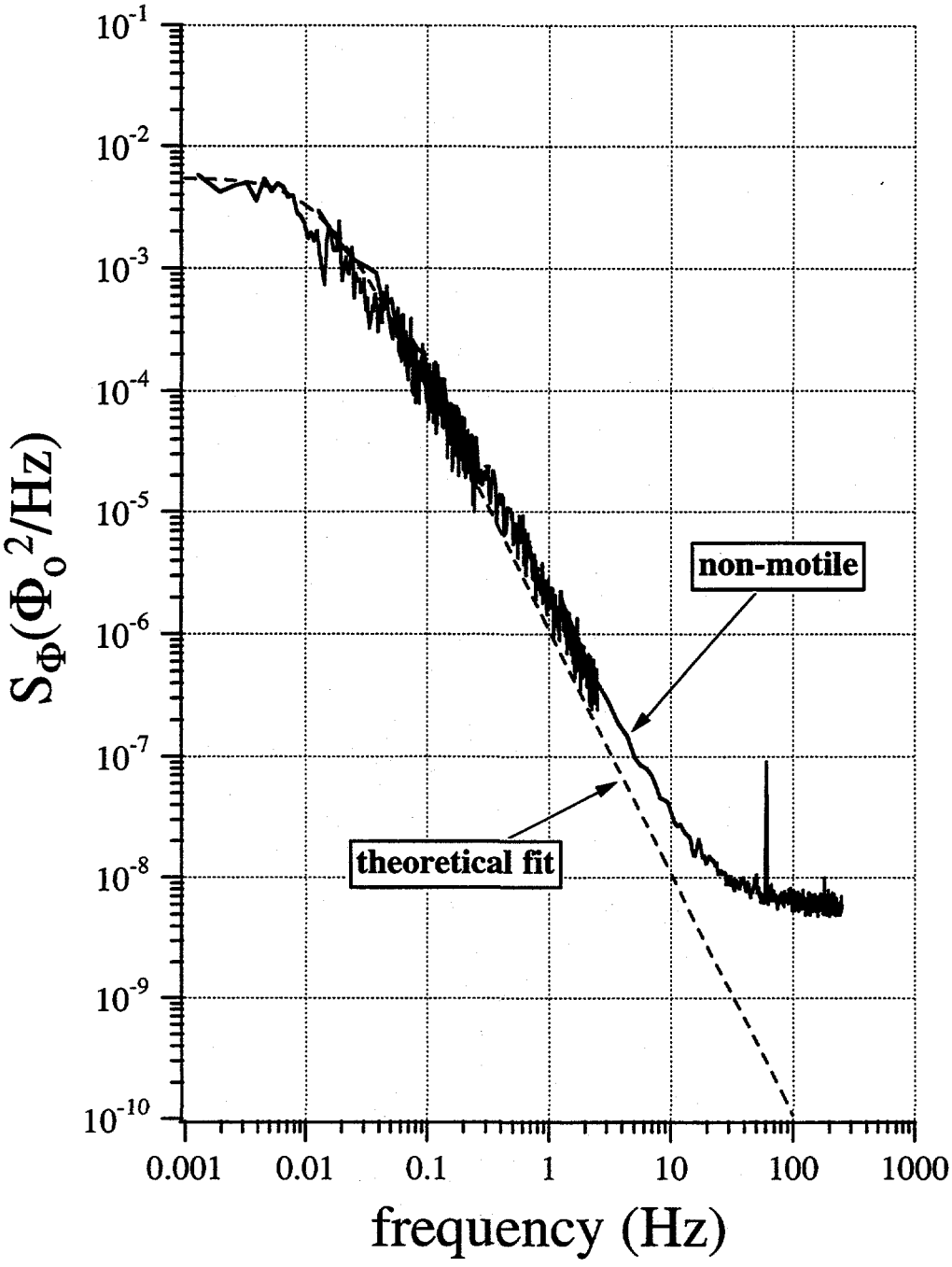

Figure 9.9: Spectral density of non-motile bacteria (MS-1) taken from a different culture solution. The dashed-line represents a theoretical fit based on Equation 9.2. The white noise of the SQUID is apparent at high frequencies.

of L_b was narrower in this sample than in that of Figure 9.4. The dashed-line indicates a theoretical fit based on Equation 9.2 with $\tau_r = 16$ sec and $f_k(Brownian) \approx 0.01$ Hz. Assuming that $d_b = 1\ \mu$m, Equation 9.8 gives $L_b \approx 4\ \mu$m, which roughly agrees with observations made with an optical microscope. Note that we have chosen the theoretical fit to match better at low frequencies in the region of the roll-off. The fact that the data begins to deviate from it at high frequencies (excluding the emergence of the SQUID white noise) indicates that the bacteria spectrum probably represents a sum of curves with different τ_r.

9.2.4 Observing a Single Bacterium

During one of the measurement runs on motile bacteria, we observed very large oscillations in approximately 1 out of 10 time traces. As shown in Figure 9.10(a), the oscillations were much greater than the net signal derived from many bacteria uniformly distributed throughout the sample well. We eliminated environmental noise as the cause since these oscillations never appeared when there was no sample in the well. Furthermore, given the low oscillation frequency, it was extremely unlikely that body precession resulting from flagellar rotation was the cause. I then realized that the oscillations were very likely due to the motion of single bacteria executing circular swimming orbits directly over the SQUID and in the plane of the window (Figure 9.10(b)). In fact, we had observed such motion near glass surfaces when looking at bacteria under an optical microscope. Orbits near planar surfaces have also been observed for other bacteria [58]. For a bacterium swimming close to a surface, hydrodynamic simulations predict that the rotation of the body about its own axis combined with translational motion gives rise to orbits. [59]. However, what is not understood is the physical origin of the attractive interaction keeping the bacterium in close proximity to the surface for long stretches of time. Electrostatic and van der Waals forces may play important roles [58].

Although the exact positions of the orbits relative to the SQUID are not known, the amplitudes and periods of the oscillations roughly agree with estimates based on the known average dipole moment and swimming speed of the bacteria. These estimates assume that the bacterium swims in and out of the SQUID loop at a vertical distance equal to the separation between the SQUID and the side of the window facing the liquid (about 15 μm). The diameter of an orbit is assumed to be comparable to the size of the SQUID (40 μm), which roughly agrees with that of orbits observed under an optical microscope.

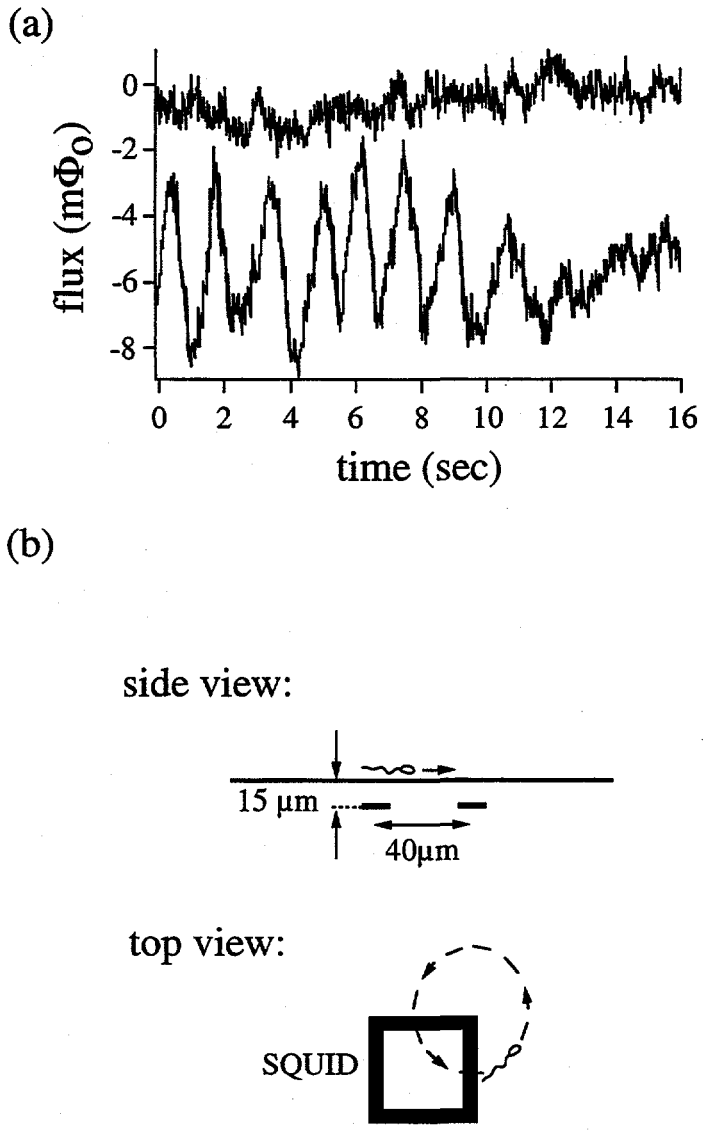

Figure 9.10: Signal from single bacterium. (a)The upper time trace represents the net signal from many bacteria uniformly distributed throughout the sample well. Large oscillations in the lower trace (offset for clarity) reflect the contribution from a single bacterium circling above the SQUID. (b) Physical interpretation of the oscillations as arising from orbits near the window surface.

We did not observe these large oscillations during the measurement of the motile-bacteria spectral density in Figure 9.4. I speculate that the absence of orbits is due to the suppression of the attractive force between bacteria and the window. Over several consecutive experiments in the same well, dead bacteria gradually adsorb to the window surface and become impossible to wash off without damaging the window. These bacteria do not significantly contribute to the signal, since they are essentially immobile. However, their presence may disrupt the attractive interaction between motile bateria and the window surface, thereby eliminating the orbits.

9.2.5 Other Potential Measurements in Free Solution

One can imagine several other experiments on bacteria in free solution. For example, one could look at the effects of applied magnetic fields, both DC and AC, on the flux spectral density of motile bacteria. In particular, a sufficiently strong DC field would very likely shift the knee frequency to lower values, since directional changes would be supressed by the magnetic torque. Furthermore, the ratio between the heights of the high frequency peaks may be changed by the perturbing influence of the field. Another experiment would be to measure the decay time of the magnetization, for both motile and non-motile bacteria, following the application of a magnetic field. The decay time for non-motile bacteria should agree with the relaxation time ($\approx$ 16 sec) extracted from spectral density measurements.

One could investigate the impacts of chemoattractants and other chemical stimuli on the flux spectral density. For example, during some of our measurements, we observed that the high frequency peaks shifted to lower frequency over time, while the ratio of the peak frequencies seemed to remain constant. This might be explained by the slowing of the flagellar motor as a result of chemical or oxygen contamination. Furthermore, chemoattractants often cause the mean time between changes in swimming direction to lengthen [60]. This would very likely push $f_k(motile)$ to lower frequencies.

The difficulty in interpreting the value of $f_k(motile)$ in Figure 9.4 arises from accounting for the effects of both translational and rotational motion. However, there is a way to arrange the experimental geometry such that flux changes to translational motion are largely frozen out. Let us imagine that all 3 dimensions of the sample well are several times smaller than the size of the pick-up loop (s). We further assume that the spacing between the sample bottom and the pick-up loop is much smaller than s. Then one can see

that the translation of a bacterium, with fixed orientation, anywhere inside the sample well will produce only a small change in flux compared to the flux change induced by rotating a bacterium by 180 degrees. This experimental arrangement would allow one to measure the rotational component of the motion, while suppressing the translational contribution.

9.3 Remote-Sensing through Porous Media

9.3.1 Application to Bioremediation

One would like to apply the SQUID microscope to a problem in bacterial motion which optical techniques cannot address. I formulated one possibility during a foray into the biology literature. While skimming through a biophysics journal, I came across an article by Professor Roseanne Ford's group at the University of Virginia describing calculations of the dynamics of bacterial migration in porous media [61]. One of the key references [62] described her group's experimental measurements of the effective diffusion constant of swimming bacteria in a liquid-saturated sand column in the presence of a chemoattractant gradient. Bacteria were placed in the lower half of a column and chemoattractant in the upper half. The bacteria were allowed to migrate for a certain length of time up the step gradient in chemoattractant concentration. The column was then cut into sections, and the bacteria in each section were counted in order to acquire the spatial distribution of the bacterial number density over the length of the column. The effective diffusion constant was then fitted to this distribution. The experiment was repeated for different sand particle sizes to measure the dependence of the diffusion constant on the particle diameter.

The motivation behind this work was to develop numerical models relevant to bioremediation applications. Bioremediation is concerned with using living organisms to convert hazardous environmental waste into benign products. Bacteria can be genetically selected to swim towards, process, and neutralize a particular waste product, which can act as a chemoattractant for the cells. One approach to waste cleanup is to inject such bacteria into an underground waste site, where the waste is often mixed with soil and water. In this case, bioengineers need to understand and predict how bacteria will migrate throughout the site and respond to concentration gradients of the waste. This requires understanding bacterial migration dynamics in the porous soil matrix. Hence, researchers carry out model studies, such as the one described above, in order to formulate and test theories of potential

use to bioremediation engineers in the field.

There are several limitations associated with determining bacterial distributions using the sectioning method. First, one cannot visualize the evolution of the bacterial distribution continuously. A separate column must be made for each sampling time, since a column cannot be re-used after it is sectioned. This reduces the flexibility of the technique and limits the time resolution. Second, the experimental error in measuring the bacterial density in a given section of the column is quite large. Very often, the density can only be determined to within a factor of 5-10 of the actual value. It is likely that the invasiveness of the technique is mainly responsible for this large error. In order to address these difficulties, researchers have searched for an in situ, non-destructive method for measuring the bacterial distribution. Since the porous matrix is often optically opaque or a strong light scatterer, optical measurements are ineffective.

Researchers have attempted to apply diffusion-weighted magnetic resonance imaging (MRI) to the problem [63]. The idea is to create contrast between water protons inside and outside the bodies of bacteria by measuring the relative diffusion lengths of the water molecules. Since water inside a bacterium is confined by the cell membrane to a small volume, the diffusion length of a water molecule is effectively smaller than that of water outside the cell. Since the concentrations of water inside and outside the bacteria are roughly the same, the number density of bacteria is simply proportional to the fraction of total protons found inside cells. This proton fraction can be measured and spatially-mapped with an appropriate MRI pulse sequence, including the application of a gradient pulse. These researchers were able to visualize variations in bacteria number density over millimeter length scales. However, for a $(1\,\mathrm{mm})^3$ voxel size, their minimum detectable cell density, n_{min}, is on the order of 5×10^8 cells/ml achieved by averaging 128 scans taken over a period of 20 minutes. This value of n_{min} is above the range of cell densities (10^4 to 10^8 cells/ml) typically encountered in migration experiments and in bioremediation applications.

Upon encountering Ford's work, I wondered whether it would be possible to map the distribution of *magnetically-tagged* bacteria in an opaque, porous matrix using a SQUID microscope. My first thought was to use magnetotactic bacteria as a naturally-tagged, model organism in a migration experiment to gauge the feasibility of the technique. If this proved successful, then perhaps a suitable method for magnetically-tagging any type of micro-organism could be developed so that the SQUID method could be extended.

9.3.2 Proposed Experiment

My proposal for a migration experiment using magnetotactic bacteria is shown in Figure 9.11. A porous matrix is sandwiched between two sheets, the bottom one of which is made particularly thin, perhaps out of mylar, to minimize the SQUID-sample distance. The SQUID should have a large pick-up area in order to maximize the coupled flux. For this experiment, spatial resolution of 1 mm would be adequate. Perhaps a large-area slit SQUID or a directly-coupled SQUID [64] could be used. Note that a sapphire vacuum window is used in order to minimize window bowing for the relatively large window area needed to accomodate the SQUID chip. A chemoattractant step-gradient is established by saturating the right half of the liquid chamber with chemoattractant. Bacteria are initially placed in the left half. At periodic intervals, the sample chamber is scanned over the SQUID to acquire either a one or two-dimensional image. In order to acquire true "snapshot" images, the imaging time is short compared to the characteristic time (perhaps several hours or so) over which the spatial distribution of bacteria changes significantly.

The signal intensity at each pixel of the image must be proportional to the local bacterial number density. My proposal for gauging the number density is to measure the height of the peak in the flux spectral density due to body precession. The peak height should be proportional to the number density, although this should be verified experimentally. The main virtues of this method are that it is non-invasive and requires relatively short averaging times due to the high frequency of the peak (25 Hz). A key parameter that must be measured is the value of n_{min} resolvable by the technique. n_{min} could be extracted from the peak height produced by known concentrations of cells placed in the sample chamber. For example, the signal-to-noise ratio of the 25 Hz peak in Figure 9.4 is about 250 (in power) for a cell density of 4.4×10^7 cells/ml (the SQUID noise at 25 Hz is $\approx 1 \times 10^{-9}\ \Phi_o^2/\mathrm{Hz}$). Hence, $n_{min} = 4.4 \times 10^7/250 = 1.8 \times 10^5$ cells/ml.

We can try to scale this result to the proposed experimental situation in the following way. Let us assume that the ratio between the peak height and the spectral density of the non-motile bacteria *at the peak frequency* (25 Hz) is intrinsic to the bacteria and independent of the cell density, the porosity of the matrix, and the geometry of the measurement set-up. This is a reasonable assumption since the peak and the signals from non-motile bacteria arise from small-scale motions of the bacteria. From Figure 9.4, we see that $S_\Phi(peak)/S_\Phi(nonmotile, f = 25\ \mathrm{Hz}) \approx 150$.

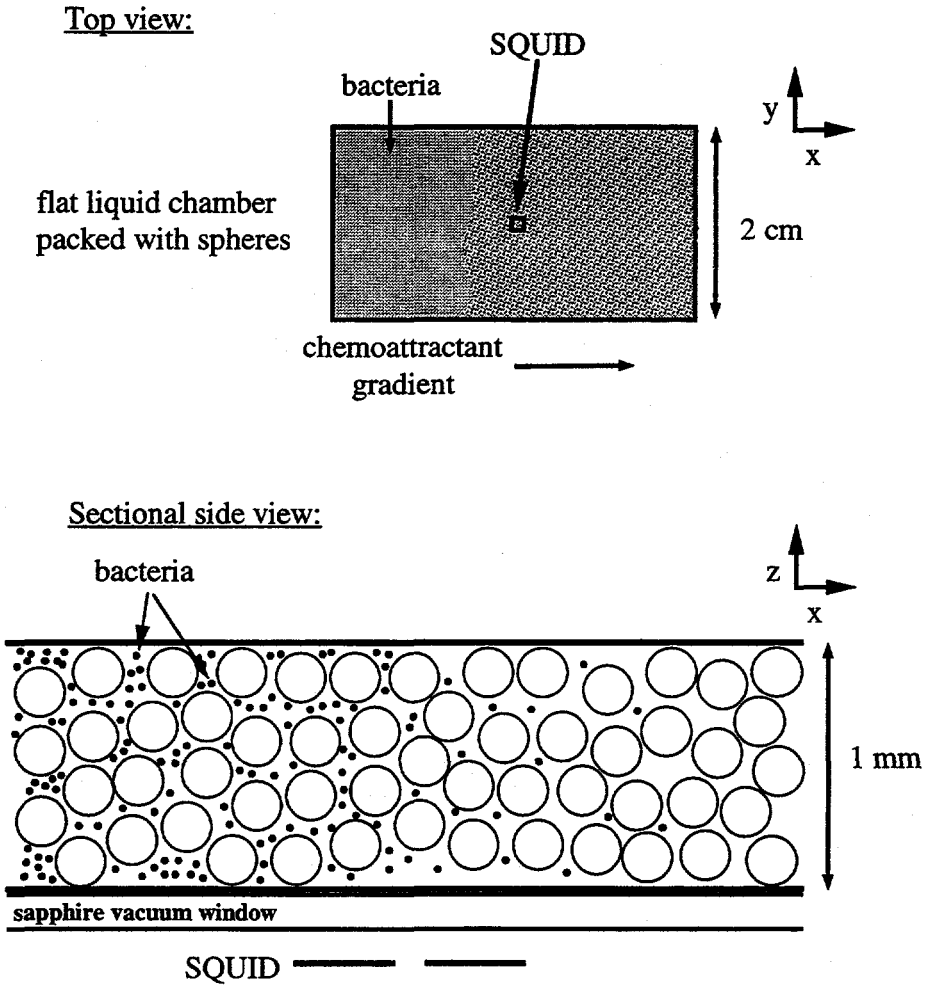

Figure 9.11: Proposed experiment to measure migration of magnetotactic bacteria through a porous matrix. Liquid chamber is scanned over the window to image the 2-dimensional bacteria distribution.

I have written a computer program which numerically calculates the total flux spectral density (Equation 9.2) over a population of non-motile bacteria uniformly distributed in a sample well of known dimensions and with a specific SQUID-window distance and SQUID size. For the proposed experimental geometry (sample dimensions = 2 mm x 2 mm area x 1 mm-thickness, SQUID-sample spacing = 250 μm, and square pick-up loop size = 1 mm), this program predicts that the spectral density should increase in magnitude by a factor of 80 over what is measured in Figure 9.4 for the same cell number density, based on the different geometrical parameters of the measurement. In other words, if we were to change the well dimensions, SQUID-sample spacing, and SQUID loop size from their original values to the those of the proposed experiment, then the spectral density of the non-motile bacteria would increase by 80 times. Since I assumed that $S_\Phi(peak)/S_\Phi(nonmotile, f = 25\,\text{Hz})$ remains constant, the peak height would also increase by a factor of 80. The other aspect of the proposed experiment that must be accounted for is the excluded volume due to the porous matrix. The bacteria solution will be confined to the interstitial spaces, which effectively reduces the total number of bacteria per sample volume. A reasonable value for the ratio between the interstitial and total volumes is about 0.4 [62]. Hence, this reduces the peak enhancement factor to 0.4(80) = 32, giving an absolute peak height in the proposed experiment of $9.6 \times 10^{-6}\,\Phi_o^2/\text{Hz}$ for a cell density (in interstitial spaces) of 4.4×10^7 cells/ml.

In order to deduce the rescaled n_{min}, we must know the sensitivity of the SQUID at the peak frequency. Given that I assumed a square pick-up loop with a 1 mm side length, let us assume that it is part of a directly-coupled SQUID [64]. I take the SQUID loop itself to be 10 μm on a side and the flux coupling coefficient between the pick-up loop and the SQUID to be unity. The ratio between the self-inductances of the pick-up loop and the SQUID is about 100, which therefore reduces the flux sensed by the SQUID by the same factor. So for a cell number density (interstitial) of 4.4×10^7 cells/ml, the measured spectral density of the peak is only $9.6 \times 10^{-6}\Phi_o^2/\text{Hz}/100^2 = 9.6 \times 10^{-10}\,\Phi_o^2/\text{Hz}$. For a SQUID of this size, we expect a noise of perhaps $(5\,\mu\Phi_o/\sqrt{Hz})^2 \approx 3 \times 10^{-11}\,\Phi_o^2/\text{Hz}$ at 25 Hz. Hence, the expected minimum detectable density is $n_{min} = (\frac{3\times10^{-11}\Phi_o^2/\text{Hz}}{9.6\times10^{-10}\Phi_o^2/\text{Hz}})\,4.4\times10^7\text{cells/ml} \approx 1.4\times10^6$ cells/ml. This is more than two orders of magnitude smaller than the value achieved with the MRI technique [63], although it is still 100 times larger than the lowest cell densities (10^4 cells/ml) encountered in migration experiments. Perhaps n_{min} could be lowered significantly by using a slit-type rather than directly-coupled SQUID, although calculating the flux coupled into a slit SQUID is considerably more difficult. In the end, direct measurement of the signal-

to-noise ratio for a given SQUID geometry will be the true test.

Other than the minimum detectable density, there are several other important issues that need to be addressed in order to determine the feasibility of the technique. First, adhesion of bacteria to the particles in the matrix should be quantified. It should be possible to choose a particle material which reduces adhesion to negligible levels [62], although some trial-and-error will probably be necessary. Second, if the peak-height method to measure number density is used, any shifts in the positions or heights of the peaks due solely to changes in chemoattractant concentration, as the bacteria migrate up the chemoattractant gradient, must be accounted for. Third, since the total time of the experiment may be relatively long (on the order of 24 hours), number density changes due to cell division and decreases in average swimming speed as the culture ages must be factored into the experiment. For simplicity of data interpretation, perhaps cell division could be halted in some biochemical fashion without lysing the cells. Barton [62] accounted for the decay in swimming speed when extracting effective diffusion constants for migrating bacteria . They attributed this observed decay to nutrient or oxygen deprivation as the culture reached the stationary phase of growth. Presumably, MS-1 bacteria experiences a similar effect, which must be quantified in order to properly interpret the migration data. Last, the cells must be kept alive and swimming for the duration of the experiment. Clearly, improvements on the present survival time (less than 12 hours) must be made.

Bibliography

[1] J.R. Clem. Johnson noise from normal metal near a superconducting SQUID gradiometer circuit. *IEEE Transactions on Magnetics*, MAG-23:1093–1096, March 1987.

[2] T. Van Duzer and C.W. Turner. *Principles of Superconductive Devices and Circuits.* Elsevier, New York, 1981.

[3] M.J. Ferrari, M. Johnson, F.C. Wellstood, J.J. Kingston, T.J. Shaw, and J. Clarke. Magnetic flux noise in copper oxide superconductors. *Journal of Low Temperature Physics*, 94:15–61, January 1994.

[4] T.H. Geballe and J.K. Hulm. Superconductivity-the state that came in from the cold. *Science*, 239:367–375, January 22, 1988.

[5] J.R. Clem. Two-dimensional vortices in a stack of thin superconducting films. a model for high-temperature superconducting multilayers. *Physical Review B*, 43:7837–7846, April 1, 1991.

[6] M.V. Feigel'man, V.B. Geshkenbein, and A.I. Larkin. Pinning and creep in layered superconductors. *Physica C*, 167:177–187, April 15, 1990.

[7] A. Buzdin and D. Feinberg. Electromagnetic interaction of vortices in layered superconducting structures. *J. Phys. (Paris)*, 51:1971–1978, September 1, 1990.

[8] S.N. Artemenko and A.N. Kruglov. Structure of 2-d vortex in a layered high-tc superconductor. *Physics Letters A*, 143:485–488, February 5, 1990.

[9] L.I. Glazman and A.E. Koshelev. Thermal destruction of phase coherence in layered superconductors. a new phase transition in an ordered vortex state. *Physica C*, 173:180–184, February 1, 1991.

[10] A. Kapitulnik. In K.S. Bedell, M. Inui, D. Meltzer, J.R. Schrieffer, and S. Doniach, editors, *Phenomenology and Applications of High-Temperature Superconductors*, page 34, Reading, 1992. Addison-Wesley.

[11] J.R. Clem. Effects of anisotropy and layering in the high-temerature superconductors. *Physica C*, 200:118–126, November 15, 1993.

[12] L.N. Bulaevskii, M. Ledvij, and V.G. Kogan. Vortices in layered superconductors with Josephson coupling. *Physical Review B*, 46:366–380, July 1, 1992.

[13] R. Busch, G. Ries, H. Werthner, G. Kreiselmeyer, and G. Saemann-Ischenko. New aspects of the mixed state from six-terminal measurements on BSCCO single crystals. *Physical Review Letters*, 69:522–525, July 20, 1992.

[14] H. Safar, E. Rodriguez, F. de la Cruz, P.L. Gammel, L.F. Schneemeyer, and D.J. Bishop. Observation of two-dimensional vortices in BSCCO. *Physical Review B*, 46:14238–14241, December 1, 1992.

[15] H. Safar, P.L. Gammel, D.A. Huse, S.N. Majumdar, L.F. Schneemeyer, D.J. Bishop, D. Lopez, G. Nieva, and F. de la Cruz. Observation of a nonlocal conductivity in the mixed state of YBCO:experimental evidence for a vortex line liquid. *Physical Review Letters*, 72:1272–1275, February 21, 1994.

[16] J. Clarke. SQUID concepts and systems. In H. Weinstock and M. Nisenoff, editors, *NATO ASI Series Vol. F59: Superconducting Electronics*, page 87, Berlin, 1989. Springer-Verlag.

[17] F.C. Wellstood. *Excess Noise in the dc SQUID: 4.2 K to 20 mK*. PhD thesis, University of California at Berkeley, 1988.

[18] J.N. Eckstein, I. Bozovic, M. Klausmeier-Brown, G.F. Virshup, and K.S. Ralls. Atomically layered growth and properties of high temperature superconducting single-crystal films and superlattices. *Thin Solid Films*, 216:8–13, August 28, 1992.

[19] K. Char, N. Newman, S.M. Garrison, R.W. Barton, R.C. Taber, S.S. Laderman, and R.D. Jacowitz. Microwave surface resistance of epitaxial YBCO thin films on sapphire. *Applied Physics Letters*, 57:409–411, July 23, 1990.

[20] L.W. Lombardo and A. Kapitulnik. Growth of BSCCO single crystals using MgO crucibles. *Journal of Crystal Growth*, 118:483–489, April 1992.

[21] L.F. Schneemeyer, J.V. Waszczak, T. Siegrist, R.B. van Dover, L.W. Rupp, B. Batlogg, R.J. Cava, and D.W. Murphy. Superconductivity in YBCO single crystals. *Nature*, 328:601–603, August 13, 1987.

[22] L. Civale, A.D. Marwick, T.K. Worthington, M.A. Kirk, J.R. Thompson, L. Krusin-Elbaum, Y. Sun, J.R. Clem, and F. Holtzberg. Vortex confinement by columnar defects in YBCO crystals: enhanced pinning at high fields and temperatures. *Physical Review Letters*, 67:648–651, July 29, 1991.

[23] J.R. Clem. 2-d pancake vortices in a finite stack of superconducting layers. *Physica C*, 235-240:2607–2608, December 1994.

[24] D.R. Nelson. Statistical mechanics of flux lines in high-tc superconductors. *Journal of Statistical Physics*, 57:511–530, 1989.

[25] D.S. Fisher, M.P.A. Fisher, and D.A. Huse. Thermal fluctuations, quenched disorder, phase transitions, and transport in type-ii superconductors. *Physical Review B*, 43:130–159, January 1, 1991.

[26] J. Wikswo. SQUID magnetometers for biomagnetism and nondestructive testing: important questions and initial answers. *IEEE Transactions on Applied Superconductivity*, 5:74–120, June 1995.

[27] L.N. Vu, M.S. Wistrom, and D.J. van Harlingen. Imaging of magnetic vortices in superconducting networks and clusters by scanning SQUID microscopy. *Applied Physics Letters*, 63:1693–1695, September 20, 1993.

[28] A. Mathai, Y. Gim, R. Black, A. Amar, and F. Wellstood. Experimental proof of a time-reversal-invariant order parameter with a pi-shift in YBCO. *Physical Review Letters*, 74:4523–4526, May 1995.

[29] J. Kirtley, M.B. Ketchen, K.G. Stawiasz, W.J. Gallagher, S.H. Blanton, and S.J. Wind. High-resolution scanning SQUID microscope. *Applied Physics Letters*, 66:1138–1140, February 1995.

[30] C.C. Tsuei, J.R. Kirtley, C.C. Chi, L.S. Yu-Jahnes, A. Gupta, T. Shaw, J.Z. Sun, and M.B. Ketchen. Pairing symmetry and flux quantization in a tricrystal superconducting ring of YBCO. *Physical Review Letters*, 73:593–596, July 1994.

[31] R.C. Black, A. Mathai, F.C. Wellstood, E. Dantsker, A.H. Miklich, D.T. Nemeth, J.J. Kingston, and J. Clarke. Magnetic microscopy using a liquid nitrogen cooled YBCO superconducting quantum interference device. *Applied Physics Letters*, 62:2128–2130, April 26, 1993.

[32] R.C. Black, F.C. Wellstood, E. Dantsker, A.H. Miklich, J.J. Kingston, D.T. Nemeth, and J. Clarke. Eddy current microscopy using a 77-k superconducting sensor. *Applied Physics Letters*, 64:100–102, January 3, 1994.

[33] R.C. Black, F.C. Wellstood, E. Dantsker, A.H. Miklich, D. Koelle, F. Ludwig, and J. Clarke. Imaging radio-frequency fields using a scanning squid microscope. *Applied Physics Letters*, 66:1267–1269, March 6, 1995.

[34] R.C. Black, F.C. Wellstood, E. Dantsker, A.H. Miklich, D.T. Nemeth, D. Koelle, F. Ludwig, and J. Clarke. Microwave microscopy using a superconducting quantum interference device. *Applied Physics Letters*, 66:99–101, January 2, 1995.

[35] H. Weinstock and M. Nisenoff. Nondestructive evaluation of metallic structures using a SQUID magnetometer. In H.D. Hahlbohm and H. Lübbig, editors, *SQUID '85–Superconducting Quantum Interference Devices and Their Applications*, pages 853–858, Berlin, 1985. de Gruyter.

[36] G. Donaldson, S. Evanson, M. Otaka, K. Hasegawa, T. Shimizu, and K. Takaku. Use of SQUID magnetic sensor to detect aging effects in duplex stainless steel. *British Journal of Non-destructive Evaluation*, 32:238–240, May 1990.

[37] D.S. Buchanan, D.B. Crum, D. Cox, and J.P. Wikswo. MicroSQUID: a close-spaced four channel magnetometer. In S.J. Williamson, M. Hoke, G. Stroink, and M. Kotani, editors, *Advances in Biomagnetism*, pages 677–679, New York, 1990. Plenum.

[38] A.D. Hibbs, R.E. Sager, D.W. Cox, T.H. Aukeman, T.A. Sage, and R.S. Landis. A high-resolution magnetic imaging system based on a SQUID magnetometer. *Review of Scientific Instruments*, 63:3652–3658, July 1992.

[39] L.N.C. Morgan, C. Carr, A. Cochran, D.McA. McKirdy, and G.B. Donaldson. Electromagnetic nondestructive evaluation with simple HTS SQUIDs: measurements and modelling. *IEEE Transactions on Applied Superconductivity*, 5:3127–3130, June 1995.

[40] B.J. Roth, N.G. Sepulveda, and J. Wikswo. Using a magnetometer to image a two-dimensional current distribution. *Journal of Applied Physics*, 65:361–372, January 1989.

[41] R.C. Black. *Magnetic Microscopy Using a Superconducting Quantum Interference Device.* PhD thesis, University of Maryland, 1995.

[42] R.A. Stewart, J. Kim, R.M. White, and R.S. Muller. Young's modulus and residual stress of LPCVD silicon-rich silicon nitride determined from membrane deflection. *Sensors and Materials*, 2:285–298, 1991.

[43] S. Timoshenko and S. Woinowsky-Krieger. *Theory of Plates and Shells*, page 401. McGraw-Hill, New York, 1959.

[44] A.H. Miklich, D. Koelle, E. Dantsker, D.T. Nemeth, J.J. Kingston, R.F. Kromann, and J. Clarke. Bicrystal YBCO DC SQUIDs with low noise. *IEEE Transactions on Applied Superconductivity*, 3:2434–2437, March 1993.

[45] J.T. Harding and J.E. Zimmerman. Quantum interference magnetometry and thermal noise from a conducting environment. *Physics Letters A*, 27:670–671, October 7, 1968.

[46] T. Varpula and T. Poutanen. Magnetic field fluctuations arising from thermal motion of electric charge in conductors. *Journal of Applied Physics*, 55:4015–4021, June 1, 1984.

[47] R.H. Koch, W.M. Goubau, J.M. Martinis, C.M. Pegrum, D.J. van Harlingen, and J. Clarke. Flicker (1/f) noise in tunnel junction dc SQUIDs. *Journal of Low Temperature Physics*, 51:207–224, April 1983.

[48] R.B. Blakemore. Magnetotactic bacteria. *Science*, 190:377–379, October 24, 1975.

[49] S. Spring and K. Schleifer. Diversity of magnetotactic bacteria. *System. Appl. Microbiol.*, 18:147–153, 1995.

[50] R.B. Blakemore. Magnetotactic bacteria. *Annual Review of Microbiology*, 36:217–238, 1982.

[51] R.B. Blakemore. Isolation and pure culture of a freshwater magnetic spirillum in chemically defined medium. *Journal of Bacteriology*, 140:720–729, November 1979.

[52] G. Lowe, M. Meister, and H.C. Berg. Rapid rotation of flagellar bundles in swimming bacteria. *Nature*, 325:637–640, February 12, 1987.

[53] H.C. Berg. *Random Walks in Biology*, pages 78–79. Princeton University Press, New Jersey, 1983.

[54] H.C. Berg and L. Turner. Torque generated by the flagellar motor of escherichia coli. *Biophysical Journal*, 65:2201–2216, November 1993.

[55] A.D.T. Samuel and H.C. Berg. Fluctuation analysis of rotational speeds of the bacterial flagellar motor. *Proceedings of the National Academy of Sciences*, 92:3502–3506, April 1995.

[56] M. Silverman and M. Simon. Flagellar rotation and the mechanism of bacterial motility. *Nature*, 249:73–74, May 3, 1974.

[57] M.M. Tirado and J.G. de la Torre. Rotational dynamics of macromolecules. *Journal of Chemical Physics*, 73:1986–1993, August 15, 1980.

[58] P.D. Frymier, R.M. Ford, H.C. Berg, and P.T. Cummings. Three-dimensional tracking of motile bacteria near a solid planar surface. *Proceedings of the National Academy of Sciences*, 92:6195–6199, June 1995.

[59] M. Ramia, D.L. Tullock, and N. Phan-Thien. The role of hydrodynamic interaction in the locomotion of microorganisms. *Biophysical Journal*, 65:755–778, August 1993.

[60] H.C. Berg. How bacteria swim. *Scientific American*, 223:36–44, August 1975.

[61] K.J. Duffy, P.T. Cummings, and R.M. Ford. Random walk calculations for bacterial migration in porous media. *Biophysical Journal*, 68:800–806, March 1995.

[62] J.W. Barton and R.M. Ford. Determination of effective transport coefficients for bacterial migration in sand columns. *Applied and Environmental Microbiology*, 61:3329–3335, September 1995.

[63] K. Potter, R.L. Kleinberg, F.J. Brockman, and E.W. McFarland. Assay for bacteria in porous media by diffusion-weighted NMR. *Journal of Magnetic Resonance B*, 113:9–15, 1996.

[64] D. Koelle, A.H. Miklich, L. Ludwig, E. Dantsker, D.T. Nemeth, and J. Clarke. dc SQUID magnetometers from single layers of YBCO. *Applied Physics Letters*, 63:2271–2273, October 18, 1993.